On the hydrodynamics of liquid-liquid Taylor flows within mini and micro capillaries

On the Hydrodynamics of Liquid-Liquid Taylor Flows within Mini and Micro Capillaries

Seyyed Saeed Shojaee Zadeh

MSc. Eng(Hons) Mech. Eng.

Stokes Laboratories

School of Engineering

Faculty of Science & Engineering

University of Limerick

Supervisor

Dr. Vanessa Egan

Submitted to the University of Limerick for the degree of

Doctor of Philosophy (PhD)

~ May 2023 ~

Declaration

The substance of this thesis is the original work of the author, and due reference and acknowledgement has been made, where necessary, to the work of others. No part of this thesis has been submitted in candidature for any other degree.

Signed: 

Seyyed Saeed Shojaee Zadeh (Candidate)

Signed: 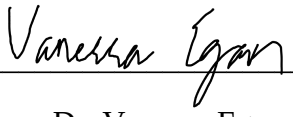

Dr. Vanessa Egan (Supervisor)

Limerick, 2023

Examination committee

Chairperson	Dr. Philip Griffin	University of Limerick
External examiner	Dr. David Kinahan	Dublin City University
Internal examiner	Prof. Jeff Punch	University of Limerick

Acknowledgement

An immense thank you to my supervisor, Dr. Vanessa Egan for her marvellous supervision, guidance, continuous support, and patience during my PhD study. *Thank you for being a wonderful teacher!* She has been a fantastic supervisor and I consider myself extremely lucky to work with such a patient and encouraging supervisor.

I am also indebted to Dr. Pat Walsh for his valuable feedback and insights that have shaped my research throughout my PhD program.

I also acknowledge the generous financial support from the Science Foundation Ireland CONNECT Centre (Grant Number: 13/RC/2007) throughout these past four years.

Thank you to all the staffs and my fellow postgrads in Stokes Laboratories and the Engineering Research Building for their kind support and creating a friendly environment, with especial mention goes to Fionnuala O'Connell.

I wish to acknowledge a friendship that began at UL and became ripe throughout my years in Ireland: thank you Dr. Joseph Mooney for making the past four-years much more enjoyable. *Thank you for introducing me to my favourite drink!*

I finish with Iran, where the source of my life energy resides: my family. I am grateful to my parents, Siroos & Nasrin, for their unwavering love and support, which keep me motivated and confident. They have cherished every wonderful moment with me and have always been there for me whenever I needed it. My heartfelt thanks go to my siblings, Sajjad & Saeedeh, for always being supportive of my adventures. And I need to thank them in Persian ...

تقدیم به وجود آسمانی آنهایی، که معنا میدهد به زندگی ام
به امن ترین پناهگاه زندگی‌ام، دستان استوار **پدرم**
به زیباترین نگاه زندگی‌ام، چشمان پرمهر **مادرم**
باشد که حاصل تلاش این حقیر، ذره‌ای بزداید غبار خستگی‌تان را
هرچند که سپاس نتوان گفت اقیانوس بی‌انتهای محبت‌تان را.

تقدیم با بوسه بر دستان پرمهرتان

This work is dedicated to my parents who taught me how to live my dreams

Abstract

This thesis presents an experimental investigation of the hydrodynamics of liquid-liquid Taylor flows in mini and micro channels, with the objectives of bridging gaps and extending previously conducted research on the subject. Taylor flows have emerged as a highly active research area due to the increasing demand for microscale devices and miniaturized components in order to reduce production costs and improve mobility. The utilization of two-phase flows in microdevices enables the dissipation of remarkably high heat fluxes within a confined space while maintaining minimal temperature variations. In addition, such flows also offer a promising platform for chemical and biomedical processes due to their well-defined high specific interfacial area and enhanced safety resulting from their extremely small dimensions. However, despite this research, the fluid mechanics of Taylor flows are still yet to be fully-determined and understanding the influence of all parameters is a big challenge, which calls for further investigation.

The context of this thesis is divided into three main aspects: the development of a precise measurement technique for slug flow characterization within microchannels; an experimental investigation on the mobility of droplets in liquid-liquid Taylor flows within circular capillaries; and experimentally investigating the pressure drop of liquid-liquid Taylor flows over varying viscosity ratios.

The first aspect introduces a novel technique to easily and reliably measure slug length and velocity. This automated, non-intrusive measurement technique allows for in-line high-frequency droplet/bubble detection and related physical properties based on changes in the light intensity caused by phase shifting in liquid-liquid or liquid-gas flows. This measurement methodology will aid in the determination and analysis of two-phase flow configurations in transparent microchannels, allowing for a better comprehension of the experimental data.

The velocity of individual droplets in liquid-liquid Taylor flow is then investigated experimentally over a wide range of Capillary number (2×10^{-4} to 3.7×10^{-2}), Bond number (0.05 to 3.2) and carrier to dispersed phase viscosity ratio (0.059 to 23.2) while also varying droplet length. This study provides a greater insight into droplet flows through an analysis of parameters affecting droplet mobility. The results indicate a complex dependency of droplet velocity on various parameters including droplet length, viscosity ratio, Reynolds and Bond number. In all cases, as droplet length exceeds a threshold value, droplet velocity becomes independent of length and is shown to scale with ~ $Ca^{0.5}$. Finally, a new expression has been developed to better estimate the velocity of elongated droplets, which has been found to correlate as a function of Capillary, Bond and Reynolds numbers.

Finally, pressure drop in liquid-liquid Taylor flow regimes is empirically explored by means of a reliable experimental set up that ensured high measurement accuracy and repeatability. The experiments were conducted using five different combinations of liquids in a capillary of 800 μm diameter. The strengths and weaknesses of existing models are identified and a more fundamental understanding of predicting pressure drop in Taylor flow regimes is developed. A new expression is presented that more accurately estimates the interfacial pressure drop in liquid-liquid Taylor flows. This correlation fits the experimental data within $\pm 20\%$ by assuming an annular velocity profile across the capillary in the presence of the second phase while accounting for inertial and viscosity ratio effects.

Overall, this study seeks to provide an improved understanding of liquid-liquid Taylor flow hydrodynamics as well as significant insights to facilitate microfluidic device optimisation.

Contents

Nomenclature

Roman	Description	Unit
A	Area	(m^2)
Bo	Bond Number ($^{\Delta\rho g D^2}/_{\gamma}$)	(-)
Ca	Capillary Number ($^{\mu U}/_{\gamma}$)	(-)
C_f	Skin-Friction Coefficient	(-)
D	Capillary Diameter	(m)
f	Friction Factor	(-)
g	Acceleration due to Gravity	(m/s^2)
h	Film Thickness	(m)
L	Capillary Length	(m)
L^*	Dimensionless Length (L/D)	(-)
P	Pressure	(Pa)
Q	Volumetric Flow Rate	(m^3/s)
R	Internal Radius of Capillary	(m)
r	Radial Position	(m)
Re	Reynolds Number $(\rho UD/\mu)$	(-)
U	Flow Velocity	(m/s)
We	Weber Number $(\rho U^2 D/\gamma)$	(-)
x	Axial Position	(m)
x^+	Dimensionless Developed Length (l/DRe)	(-)

Greek	Description	Unit
α	Volume Fraction of the Dispersed Phase (Q_D/Q_T)	(-)
γ	Interfacial Tension	(N/m)
Δ	Differential	(-)
δ	Film Thickness	(m)
ε	Void Fraction	(-)
μ	Dynamic Viscosity	(kg/ms)
ρ	Density	(kg/m^3)
σ	Surface Tension	(N/m)
τ	Shear Stress	(N/m^2)
ϕ	Pressure Gradient Ratio to the Reference Single Phase	(-)
X	Martinelli Parameter	(-)

Subscripts

A	Aqueous
app	Apparent
C, c	Carrier Phase
D, d	Dispersed Phase
Int	Interfacial
m	Mean Value
max	Maximum

O	Organic
T	Total
TP	Two Phase
u	Slug Unit Cell

Acronyms

4G	Fourth Generation
5G	Fifth Generation
AR20	Silico Oil (Polyphenyl-methylsiloxane)
CCD	Charged-Coupled Device
CFD	Computational Fluid Dynamics
CMOS	Complementary Metal Oxide Semiconductor
DAQ	Data Acquisition
DF	Droplet Flow
DI	De-ionized
DNA	Deoxyribonucleic Acid
FC40	Fluorinert^{TM} Electronic Liquid
FEP	Fluorinated Ethylene Propylene
HFE7500	Hydrofluoroether Engineered Fluid
IGBT	Insulate Gate Bipolar Transistor
LED	Light-Emitting Diode
LIF	Light-Induced Fluorescence

MCHS	Microchannel Heat Sink
MEMS	Micro-Electromechanical System
PDMS	Polydimethylsiloxane
PEG-DA	Polyethylene Glycol Diacrylate
PF	Parallel Flow
PIV	Particle Image Velocimetry
PVDF	Polyvinylidene Difluoride
SDF	Slug and Droplet Flow
SF	Slug Flow

Chapter 1

Introduction

This thesis presents a fundamental investigation of the hydrodynamic characteristics and transfer phenomena associated with liquid-liquid Taylor flows confined to mini and micro capillaries. Such flows significantly enhance heat and mass transfer compared to single phase flows and as a result, they have been employed in a variety of microfluidic areas including biological engineering, pharmaceutical industries, electronic cooling systems, and chemical engineering. In small scale tubes, liquid-liquid Taylor (slug) flow is a two-phase flow pattern consisting of a series of liquid segments separated by a second liquid which acts as the wetting carrier fluid. The fundamentals and applications of such flows have been explored in light of the growing interest in small-scale channels as an alluring technology for large-scale applications. As a result, there is now a greater requirement for knowledge of the flow hydrodynamics for the engineering and development of devices that employ such flows. Despite several attempts to develop all-encompassing models to predict the flow behaviors, existing models are still limited to narrow ranges of flow conditions. In most cases, researchers hope to generalize the results to other test conditions, however due to the complicated hydrodynamics of two-phase flows, extrapolations of correlations beyond the limits for which they were derived, can lead to poor predictions. To push the limits, the current study is concerned with the development of models for predicting liquid-liquid Taylor flow characteristics in mini / micro scale tubing. The characteristics of such flows have numerous facets, however, this work is primarily focused on:

1. An experimental investigation of droplet velocity in liquid-liquid flows with the objective of determining the effect of droplet size and viscosity ratio on droplet velocity within mini and micro capillaries.
2. Experimentally investigating pressure drop in liquid-liquid Taylor flow regimes by conducting experiments over a wide-range of flow conditions and analysing the existing models in the literature.

The influential parameters on droplet velocity and pressure drop are identified, and phenomenological models are developed as a result. A novel apparatus, capable of accurately defining the morphology and velocity of each carrier/dispersed phase unit, was developed at the beginning stage of this study to provide high confidence in the boundary conditions used for subsequent model development. The findings of this thesis have important theoretical and practical implications for the development and study of miniaturized devices that incorporate liquid-liquid Taylor flows.

This introduction chapter is divided into two main sections. Section 1.1 presents the motivation for conducting this research and gives an overview of the importance of Taylor flows. An introduction to slug flows and their characteristics are provided in Section 1.2 which also includes the theory pertinent to such flows inside small capillaries.

1.1. Motivation for Research

Modern engineers must deal with the challenges of sustainability in addition to the art of engineering in a world with constrained resources and indisputable climate change. Hence, rather than exploiting more natural resources, process intensification is a better alternative to fulfill modern life's demands while addressing sustainability concerns. At present, there is considerable interest in transferring existing technologies to small scale and the use of microfluidic devices as fundamental units has attracted special attention in the domains of mixing and separations, chemical, biomedical analysis, fuel cells and thermal management systems. Microscale devices offer more substantial advantages and more extensive application potentials than traditional channels when it comes to implementing technical procedures. In such devices, the heat and mass transfer capacity is greatly enhanced due to the reaction device's downsizing and huge surface-to-volume ratio. Specific interfacial areas as large as 9000–50,000 m^2/m^3 have been reached by reducing channel dimensions down to 50 μm, resulting in 100-times greater area than typically provided in macroscopic scales (Jähnisch *et al.* 2000). Furthermore, the microfluidic structure provides a portable and cost-effective platform that allows for precise control of hydrodynamic characteristics, resulting in a more consistent and safe process. On the other hand, strict laminar flow conditions are severely imposed on microfluidic flows by significant shear stresses associated with the narrow channel cross sections. The speed of mixing in these laminar flows is a serious challenge for applications where diffusion is paramount, and mixing must be improved through the "engineering of chaos" by employing hydrodynamic stretching-

and-folding or multi-lamination systems (Ducrée *et al.* 2006). However, the expense of manufacturing these complex features is considerably high. Under these premises, the use of multiphase flows has become a viable solution to obtain additional mixed fluids in mini and micro channels while also benefiting from a straightforward and affordable fabrication.

Generally, two phase flows form when two immiscible fluids flow together in a channel simultaneously while subjected to a pressure gradient. Such flows within mini and micro channels have unique features which are applied in a variety of applications including thermal management, biomedical and chemical processes. The application background of the such devices greatly depends on the flow configuration called "flow regime/pattern", with the most common flow pattern in the microchannels being liquid-liquid Taylor/slug flow. Slug flow occurs when one of the fluids, the carrier phase, wets the channel wall and completely engulfs the second fluid, the dispersed phase. This type of flow behaviour, in microfluidic elements, has attracted particular attention as it encompasses crucial characteristics required for the successful development and implementation of mixing, reactions, cooling and other processes that boost and elevate the performance over single-phase microfluidic systems. For the further development of microfluidics and to accelerate the transition from Lab (research) to Fab (manufacturing), designers need a comprehensive understanding of the flow hydrodynamics. During the 1970s and 1980s, several investigations and considerable research were devoted to understanding the formation and movement of the dispersed phase in two-phase flow systems. Studies progressed from investigations on the movement of a single bubble within a capillary (Bretherton 1961) to more complicated configurations including a chain of bubbles/droplets travelling through channels of various cross-section (Chisholm 1967). Interestingly, the majority of today's research still applies prior studies on a single bubble to determine the relationship between hydrodynamic and transportation phenomena for different types of two-phase flows. Given the limited accuracy of apparatus in the 70s and 80s, it is not surprising that the literature on the hydrodynamics of such flows, particularly liquid-liquid types, contains noticeable discrepancies. The accurate measurement of experimental variables (such as pressure drop, flow rate, flow velocity, etc.) is a crucial initial step in the development of a successful model. This requires an accurate and reliable measurement apparatus to characterize the flow behaviours and clearly define the boundary conditions. Nowadays, micro process engineering provides a well-developed toolkit to accurately measure flow characteristics such as pressure, temperature, and the transfer rates. Currently, in addition to invasive

methods such as anemometry or electric current measurements (Burlage *et al.* 2013), a number of non-invasive measurement techniques can be applied to capture the precise characteristics of slug flows. Examples of non-intrusive measurement methods include optics (Weber *et al.* 2013), capacitance (Isgor *et al.* 2015), and voltammetry (Gu and Fisher 2013).

To contribute to the ongoing development of microfluidic devices that rely on such flows, the overall objective of this thesis is a fundamental investigation on the hydrodynamics of liquid-liquid flows within mini and micro capillaries. It is focused on the development of models for predicting pressure drop and droplet velocity in liquid-liquid Taylor flows. The results of current research significantly add to the understanding of the hydrodynamics of Taylor flows and provide a versatile prediction tool for the design of systems that employ such flows. Moreover, this study develops an optical approach for performing high frequency real-time measurements of slug flow characteristics flowing in a transparent microfluidic channel. This measurement methodology will aid in the determination and analysis of two-phase flow configurations, allowing for a better comprehension of the experimental data.

1.2. Liquid-Liquid Slug Flows

1.2.1. Flow Characteristics

Due to the rapid growing numbers of applications that employ two phase flows in mini and microchannels as the principal means to enhance their performance, understanding the involved mechanisms and main structures of the flow field is crucial. In this regard, channel size classification helps us understand how fluid behaviour changes as the dimensions of the channel vary. Fluid dynamics in macroscopic channels can be described using classical equations, but as the channel size decreases, phenomena such as surface tension, capillary forces, and molecular interactions become increasingly significant. Transition criteria for channel size based on the critical diameter can vary depending on the specific context or field of study. However, a general transition criteria is described in a study by Kandlikar (2002) that subdivided the macro-to-microscale transition into three channel diameter size classes as: Micro-scale (below 600μm), Mini-scale (from 600 μm to 3 mm), Macroscale (greater than 3 mm). It is important to note that the specific values for the critical diameter and the corresponding transition criteria can vary depending on the

context. For example, in fluid dynamics, the concept of the critical diameter may be associated with the transition from laminar to turbulent flow. In microfluidics or nanofluidics, the critical diameter may be related to the onset of surface-driven flow effects. Therefore, the transition criteria should be considered within the specific domain or application being discussed.

Depending on the balance of viscous, gravitational, inertial and interfacial forces, two phase flows in mini/micro channels form different configurations called flow patterns/regimes. A flow pattern is a specific sort of geometrical distribution of phases with given standard names. While visual inspection is the most common method for categorizing or mapping flow regimes, other techniques are employed, such as spectral content analysis of unsteady pressures or changes in volume fraction. Recognizing the two-phase flow pattern assists in developing more accurate mass momentum, heat transfer, and pressure drop models, all of which are crucial in the design procedures (Kashid and Kiwi-Minsker 2011; Sur and Liu 2012). The most common and primary flow regimes observed in liquid-liquid horizontal mini/micro channels are slug flows (SF), slug and droplet flows (SDF), droplet flows (DF) and parallel flows (PF). Typical images of these flow regimes are presented in Figure 1.1(a).

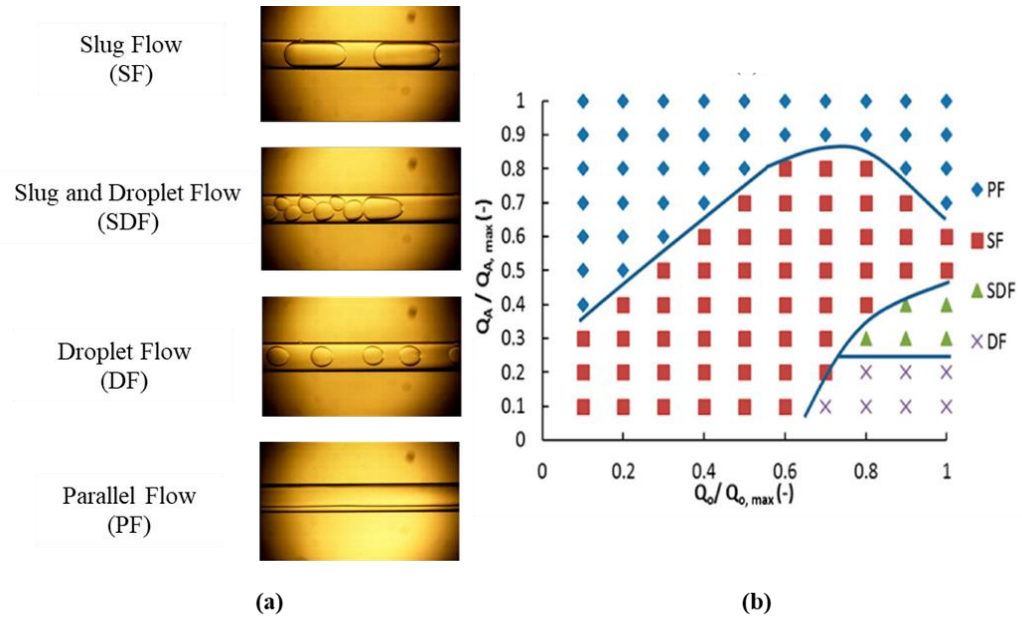

Figure 1.1. (a) Typical images of the most common liquid–liquid two-phase flow regimes within micro and mini channels and (b) an example of a flow pattern map from water-toluene experiments based on the aqueous flow rate ratio ($Q_A/Q_{A,\ max}$) and the organic flow rate ratio ($Q_O/Q_{O,\ max}$). In this example water forms the dispersed phase while toluene is the carrier liquid (Darekar *et al.* 2017).

As shown in Figure 1.1(a), in slug or Taylor flow, the diameter of the droplets approach the channel diameter and are separated by the continuous liquid. The slug and droplet flow pattern represents the transition from slug to droplet flow. This pattern of flow occurs at flow rates higher than those that display slug flow. At high carrier phase flow rates and low dispersed phase flow rates, the dispersed droplets become noticeably smaller than the capillary diameter and the flow pattern changes to droplet flow. Further increasing the continuous flow velocity at high dispersed flow rates causes the inertial force to overcome the interfacial tension force, allowing the two phases to pass one another and the parallel flow pattern to dominate. As the ratio of flow rates between the continuous and dispersed phases changes, the position of the interface changes inside the microchannel (see Figure 1.1(a)). Moreover, the Bond number directly impacts the position of the interface in parallel flows by determining the balance between gravity and surface tension forces.

Several flow regime maps for liquid-liquid flow patterns have been developed to predict the transition from one flow regime to another by means of a two-dimensional coordinate system (Dessimoz *et al.* 2008; Salim *et al.* 2008; Cherlo *et al.* 2010; Kashid and Kiwi-Minsker 2011; Tsaoulidis *et al.* 2013; Biswas *et al.* 2015; Darekar *et al.* 2017; Wu *et al.* 2017). Figure 1.1(b) gives an example of a flow pattern map for water-toluene from a study by Darekar *et al.* (2017). The x-axis displays the organic (continuous) flow rate ratio ($Q_O/Q_{O,\ max}$), and the y-axis represents the aqueous (dispersed) flow rate ratio ($Q_A/Q_{A,\ max}$). According to this map, the slug flow pattern becomes a prominent flow regime at low aqueous and organic phase flow rates. In this regime, the interfacial tension and pressure gradient govern the breakage of the dispersed phase (water) due to the expanding slug's interference with the continuous phase flow. Increasing the continuous phase flow rate while maintaining the dispersed phase flow rate causes the slug flow regime to change to slug and droplet flow, droplet flow, and parallel flow depending on the dispersed phase flow rate. Slug flow transitions to parallel flow as a result of an increase in the dispersed phase flow rate at constant continuous phase flow rate. While, droplet flow patterns often occur at low dispersed phase flow rates and relatively high continuous phase flow rates. In this condition, the dispersed phase is broken down into tiny droplets due to the inertial force imposed on by a relatively high flow rate of the continuous phase.

This thesis is focused on analysing slug flow also known as Taylor flow, or segmented flow or plug flow. It is a common flow pattern in mini and micro channels where

surface tension forces are dominant. Taylor (1961) was the researcher who carried out initial studies on two-phase slug flows to comprehend film thickness and liquid deposition at the capillary wall. A Taylor flow regime consists of two immiscible fluids flowing in a channel. As shown in Figure 1.2, one of the fluids, the carrier phase, wets the wall of the channel and engulfs a series of segmented slugs of the second fluid known as dispersed phase. The dispersed phase, with hemispherical caps at the front and rear, forms elongated droplets within the carrier phase and does not wet the wall as a thin film (film thickness) of the carrier phase is present.

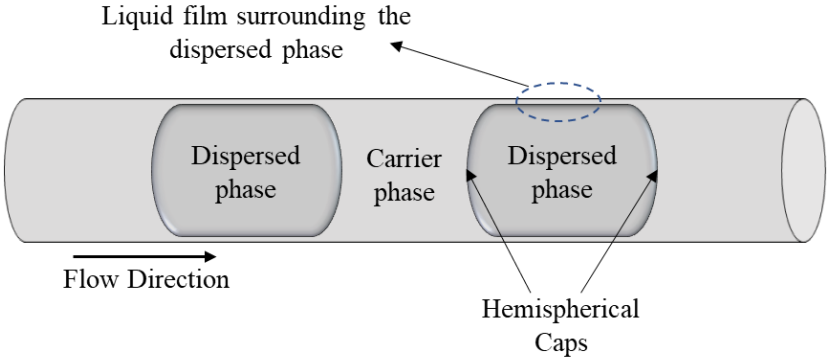

Figure 1.2. Configuration of a typical slug flow, highlighting carrier and dispersed phases, hemispherical caps, and liquid film separating the dispersed phase from the channel wall.

1.2.2. Slug Flow Generation

The various methods used to create Taylor flow can be classified into one of two categories: active or passive. Both approaches use two immiscible phases, in predetermined segments, that allow one stream to be split into separate slugs. A highly accurate flow control system is necessary to achieve precise control over slug properties, size and frequency, while utilizing these techniques. Active approaches depend on an outside stimulus to regulate the frequency and size of slugs. A piezoelectric transducer is typically used to deflect a flexible membrane or micro-valve as part of an actuation module (Chen and Lee 2006; Dong *et al.* 2006; Willaime *et al.* 2006). The instantaneous flow velocity of the dispersed phase liquid is altered by deflecting the membrane and changing the frequency at which droplet formation takes place. Different slug formations can be produced by varying the timing, amplitude, and length of a pressure pulse (Christopher and Anna 2007). The most well-known examples of this technique is the inkjet printing method that uses "drop on demand"

which deflects a membrane in contact with the reservoir to drive a droplet out of a microfabricated nozzle. The membrane must be deflected in order for droplets to form since the nozzle is too tiny (Beulen *et al.* 2007). Passive approaches are more prevalent for producing consistent liquid slugs. These techniques, which do not rely on external actuations, use the flow field to distort the interface and promote the emergence of interfacial instabilities. Commonly, a pressure source that is externally driven, such as a syringe pump, creates a pressure gradient causing the fluids to move to the segmentation device. Passive techniques can be categorized into several groups with slug formation in these categories determined by the characteristics of the flow close to the slug break-off point. Figure 1.3 shows three popular geometries for passive droplet generators: (a) co-flowing streams; (b) cross-flowing (T-junctions, X-junctions, or Y-junctions); and (c) flow-focusing (Christopher and Anna 2007). In these techniques, slugs of various sizes can be created by adjusting the ratio of liquid flow rates. The local flow field, which deforms the interface, is determined by the junction's geometry and the volumetric flow rate of both fluids. A droplet eventually separates from the dispersed liquid due to a free surface instability.

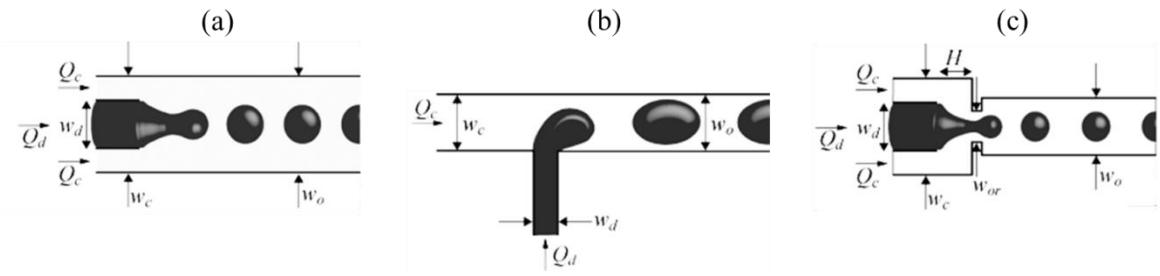

Figure 1.3. Schematic of different passive slug generators for liquid-liquid Taylor flow: (a) co-flowing streams, (b) cross-flowing streams and (c) flow-focusing geometry (Christopher and Anna 2007).

1.2.3. Scaling Groups

A number of dimensionless groups have been used by researchers for scaling of Taylor flows. These dimensionless numbers offer a way to evaluate the relative magnitudes of interacting forces and can be used to integrate two-phase flow data into more useful formats. They are collections of characterizing quantities pertinent to the flow domain without associating any physical dimensions. The dimensionless groups utilized in the hydrodynamics of Taylor flows are briefly described in this subsection.

Reynolds Number

The ratio of inertial and viscous forces is known as the Reynolds number, which is typically defined as:

$$Re = \frac{\rho U D}{\mu} \tag{1.1}$$

Where ρ, U, D and μ are density, flow velocity, characteristic length (i.e., inner diameter of the tubing) and dynamic viscosity. The Reynolds number for two-phase flow depends on the flow rates and physical characteristics of both phases. Most commonly, the Reynolds number is used to categorize flow regimes as laminar or turbulent with laminar flow defined as $Re \lesssim 2300$ for well-defined conditions within circular channels. The small characteristic length in mini and micro channels results in Reynolds numbers of typically $\lesssim 500$, implying that viscous forces dominate the inertial forces. The characteristics of the dispersed phase, carrier phase, or a combination of both phases (i.e., based on density and viscosity of the carrier phase and velocity of the dispersed phase) may be used to determine the Reynolds number in two-phase flows.

Capillary Number

An important dimensionless number in two-phase Taylor flows is the Capillary number, which is the ratio of viscous forces to interfacial tension. It is defined as:

$$Ca = \frac{\mu U}{\gamma} \tag{1.2}$$

where γ is the interfacial tension between the two immiscible liquids. In liquid-gas flows, this term is the surface tension, σ.

The Capillary number is primarily defined by the viscosity of the carrier phase (μ_C) and the bubble velocity in liquid-gas flows. However, in liquid-liquid flows, the dispersed phase's viscosity (μ_D) can also be employed to determine the Capillary number.

Given the significance of interfacial and viscous forces in slug flows, Ca is the main governing factor in describing the flow characteristics. The Capillary number also governs

the liquid film thickness around the dispersed phase, with the film becoming thicker as the Capillary number increases.

Weber Number

The ratio of the inertial and interfacial tension forces is known as the Weber number (We).

$$We = \frac{\rho U^2 D}{\gamma} \tag{1.3}$$

The Weber number is crucial in determining interfacial tension effects and slug generation in a mini and micro scale channel. By decreasing the interfacial tension between phases, slug break up can occur as a result of higher momentum transfer between the fluids.

Bond/Eotvos Number

The Bond/Eotvos number represents the ratio of capillary and gravitational (buoyancy) forces and is defined as:

$$Bo = \frac{(\Delta\rho) g D^2}{\gamma} \tag{1.4}$$

in which $\Delta\rho$ is density difference between the fluids and g is the acceleration of gravity, $9.8\, m/s^2$.

In liquid-liquid two-phase flow in micro-channels, the gravitational force can often be neglected due to very low Bond numbers (typically $Bo < 1$). Therefore, the flow behavior is found to be primarily dependent on other forces, such as surface tension, inertial, and viscous shear forces.

Void Fraction

The volumetric flow rates in the system are typically described by the void fraction of the flow, which is denoted as follows:

$$\varepsilon = \frac{Q_D}{Q_C + Q_D} \tag{1.5}$$

where Q stands for the volumetric flow rate, and C and D for the carrier and dispersed phases respectively.

In two-phase flows, the void fraction is a crucial variable since it is utilized to assess the overall performance of the flow or to minimize the number of required runs by providing a systematic way to generalize and scale the results. The word "void fraction" is frequently used in research without being properly defined, which causes confusion. The percentage of the channel's volume or length that the dispersed phase (typically gas phase) occupies is known as the void fraction. Typically, it is a volume ratio as defined in Eq. 1.5, but there are other formulations that can be found in literature.

Slug Length Ratio

In slug flows, both carrier and dispersed phase slug lengths are recognized as crucial criteria in defining flow features. The lengths of the carrier and the dispersed phases are often normalized by the inner channel diameters to become dimensionless.

$$L_C^* = \frac{L_C}{D} \quad , \qquad L_D^* = \frac{L_D}{D} \tag{1.6}$$

As depicted in Figure 1.4 , the dispersed phase slug length (L_D) is determined from nose to tail of the slug, including the hemispherical caps, and the carrier phase slug length (L_C) is measured from the nose of one dispersed slug to the tail of the following slug.

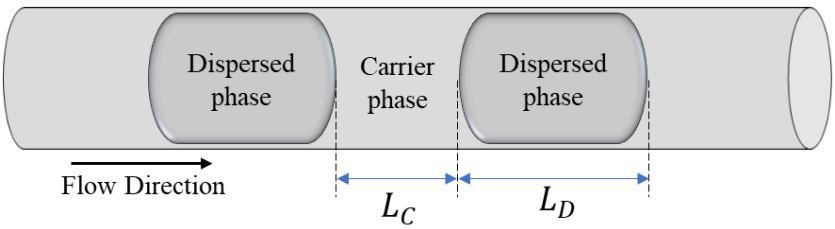

Figure 1.4. Schematic of Taylor flow, highlighting the definition of slug length.

1.2.4. Flow Dynamics

This section contains an overview of some of the key flow aspects of liquid-liquid Taylor flows. It is divided into three subsections; internal flow pattern, film thickness and pressure drop.

Internal Flow Pattern

One of the distinguishing characteristics of Taylor flows is the recirculation produced within slugs as a result of the shear stresses at the interface. These shear stresses are induced by the velocity gradient at the interface of the bubble/droplet due to the high mean velocity of the segmented phase and the surrounding film's slow movement. As depicted in Figure 1.5, the generated shear forces result in two dominant, mirrored and counter rotating vortices within the droplet (dispersed phase) that influence the flow field as the droplet advances. When the liquid in the droplet flows towards the front of the droplet, the front cap blocks the liquid, changing the flow direction towards the channel wall, which then causes the liquid to flow backwards due to friction on the channel wall. At the rear cap domain, the fluid flows from the interface near the channel wall toward the slug's center as the path is blocked by the rear interface. The circulation pattern outside the droplet is also created due to the pressure gradients across the channel length and wall friction. This is characterized by stagnation points at the droplet's nose and tail that reverse the flow and create a recirculation motion down the length of the carrier slug. Due to these internal circulations, fresh liquid continuously flows from the center of the slug towards the channel wall. This provides a renewal mechanism for the thermal and diffusion boundary layers which boosts heat and mass transfer. A variety of experimental and computational research have validated this pattern, which was first postulated by Taylor in 1961.

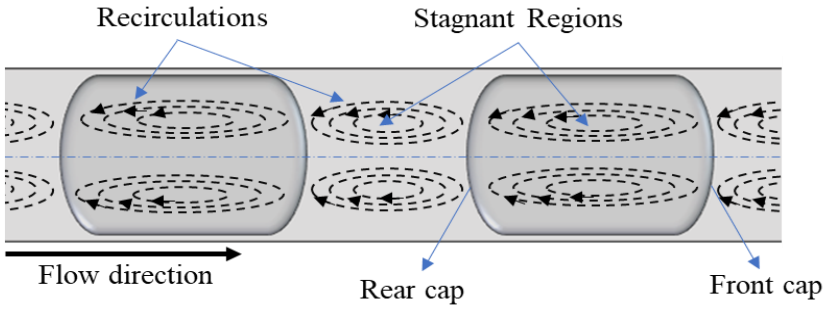

Figure 1.5. A simplified schematic representation of internal circulations within carrier and dispersed phases of a Taylor flow.

Many researchers including King *et al.* (2007), Ma *et al.* (2014), Xu *et al.* (2020) have studied these internal circulations using Particle Image Velocimetry (PIV) and Micro Image Velocimetry (μPIV). Recently developed experimental apparatuses for μPIV have

been demonstrated as promising techniques for characterizing the flow field in microchannels. This technique was first established by Thulasidas *et al.* (1997) to monitor velocity distributions inside liquid slugs while images were captured in a reference frame travelling with the bubbles. Alongside experimental studies, numerous numerical studies using CFD have also been published on the flow characteristics of Taylor flows. In most cases, 3D simulations have shown very good agreement with experimental data (Harries *et al.* 2003; Kashid *et al.* 2007). Figure 1.6 presents examples of recirculation patterns within liquid-liquid Taylor flows obtained from CFD simulations (Li and Angeli 2017) and μPIV measurements (Lindken *et al.* 2009). In Figure 1.6(a), the velocity distribution for Taylor flow is obtained from CFD simulations by modelling the flow within a capillary of 0.5 mm inner diameter. Using μPIV, Figure 1.6(b) illustrates the velocity distribution within both carrier and dispersed phases. A rectangular channel device (100 $\mu m \times 100\ \mu m$) made of PDMS (polydimethylsiloxane) was used in this study.

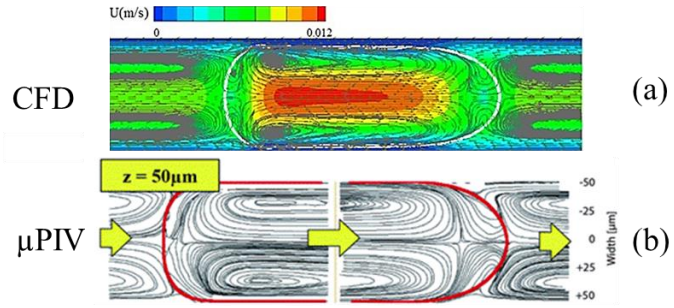

Figure 1.6. Schematic of (a) CFD and (b) μPIV measurements of flow circulation patterns within liquid-liquid Taylor flows adapted from studies by Li and Angeli (2017) and Lindken *et al.* (2009) respectively.

Film thickness

In a Taylor flow regime, a thin film of the carrier liquid, as shown in Figure 1.7, separates the dispersed phase from the channel wall. This thin barrier is a key feature of Taylor flows that influences the transfer of mass, heat, and momentum within liquid slugs.

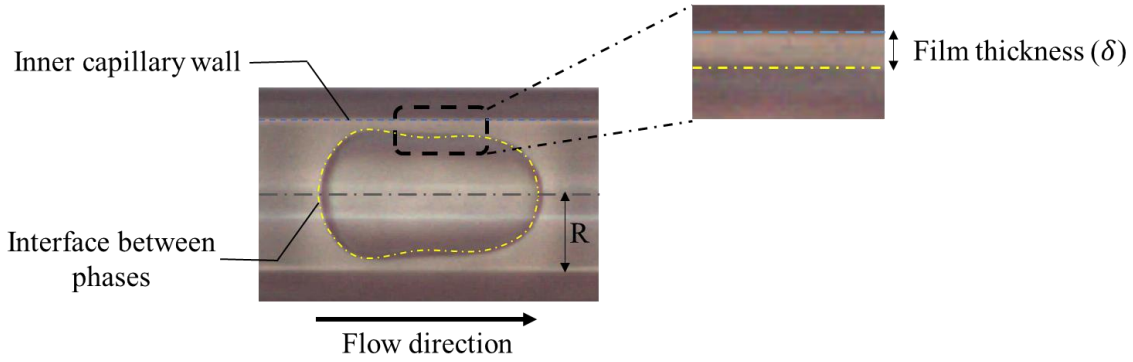

Figure 1.7. An image of an AR20 droplet dispersed in HFE7500. The interface of the droplet is outlined in yellow with top of channel wall outlined in blue. The liquid film separating the droplet from the capillary wall is highlighted on the right. The inner diameter of the capillary is measured to be 1.6 mm. Image is taken from experiments carried out in this study.

Knowledge of the film thickness is essential for real-world applications that include heat and mass transfer from the channel wall to the liquid or vice versa. It has been shown that the strength of the recirculation flow strongly depends on the magnitude of the thin film of carrier phase that separates the dispersed phase from the channel wall (Howard and Walsh 2013). Thickening the film around the droplet, reduces the recirculation intensity within the liquid slugs by allowing more fluid to bypass the slug. As a result, film thickness can significantly affect heat and mass transfer rates. In addition, in biological applications, the film thickness plays a very important role in preventing sample contamination and also cross contamination between samples within the capillary (Mac Giolla Eain *et al.* 2013a).

Several analytical and empirical studies have been conducted to characterize and develop models to predict film thickness magnitude. Analytical correlations were derived by Bretherton (1961), and Irandoust and Andersson (1989). Experimentally, direct and indirect methods have been employed to measure film thickness. In the direct method, the film thickness is typically measured by an optical microscopy technique, which employs a microscope and a high-speed CMOS camera to capture the liquid film (Han and Shikazono 2009; Howard and Walsh 2013; Mac Giolla Eain *et al.* 2013a). To measure film thickness using the indirect method, the dispersed phase velocity is measured experimentally and then used to calculate the film thickness (Suo and Griffith 1964).

In liquid-gas slug flows, Fairbrother and Stubbs (1935) made the initial attempt to find an expression for film thickness at $Ca < 0.014$. They remarked that the liquid deposition at the capillary wall caused the dispersed bubbles to move faster than the mean flow. According to their findings, the Capillary number, with the scale of $Ca^{1/2}$, was the

only factor affecting the relative drift velocity $(U_D - U_{mean})/U_D$. Subsequently, Taylor (1961) endorsed the applicability of the correlation for Ca up to 0.09 by using a single bubble moving through a liquid at low Reynolds numbers. Afterwards, a fundamental correlation for film thickness prediction was first derived by Bretherton (1961). According to this correlation, the film thickness is proportional to $Ca^{2/3}$. The expression was supported by experimental results for Capillary numbers less than 0.01. However, the model was not accurate for capillary numbers less than $\sim 10^{-4}$. Ratulowski and Chang (1990) carried out an analytical method to examine the effect of surfactants, known as the Marangoni effect, on the film thickness. According to this study, film thickness magnitude can be increased by a maximum factor of $4^{2/3}$ over the Bretherton's prediction. Later, Aussillous and Quéré (2000), by employing Taylor's experimental data, extended Bretherton's model for $Ca > 1.4$ by adding an empirical constant to the equation and suggested a new correlation called Taylor's law. They also indicated that for higher capillary numbers their model tends to underestimate the film thickness due to flow regime transformation from the inertial to the visco-inertial regime. Subsequently, a number of empirical and numerical studies have been carried out predicting and measuring film thickness. Many of the correlations resulting from these studies are based on Bretherton's model and propose the Capillary number as the only parameter affecting the film thickness magnitude (Irandoust and Andersson 1989; Kreutzer *et al.* 2001). Whereas, a number of studies have also accounted for Reynolds and Weber numbers effects (Heil 2001; de Ryck 2002; Han and Shikazono 2009). Han and Shikazono (2009) optically measured the film in liquid-gas slug flows and concluded that inertial effects need to be considered at high capillary numbers ($Ca > 0.02$). Their results also showed that film thickness becomes almost constant for Reynolds number greater than 2000. They proposed an empirical correlation based on their experiments in which the film thickness depends on Capillary, Weber and Reynolds numbers. This model showed good agreement, within 15%, with data for $Ca < 0.3$ and $Re < 2000$. The applicability of the model was extended up to $Ca < 1.9$ by Howard and Walsh (2013) who used white light optical microscopy to measure film thickness of various liquid-gas slug flow combinations. By using a similar apparatus, Mac Giolla Eain *et al.* (2013a) proposed a new model to predict film thickness in liquid-liquid Taylor flows in the visco-inertial regimes based on Capillary and Weber number. They also suggested a modified Taylor expression in the visco-capillary regime to estimate the thickness of the film. In their study capillary number ranges from 0.002 to 0.119 while the

Reynolds and the Weber number are less than 100 and 0.7 respectively. Table 1 summarises some of experimental studies on determining film thickness in both liquid-gas and liquid-liquid Taylor flows.

Table 1.1. Film thickness correlations for liquid-gas and liquid-liquid slug flows in milli/microchannels.

Author(s)	Correlation	Flow conditions
Fairbrother and Stubbs (1935)	$\delta/_R = 0.5Ca^{1/2}$	$5 \times 10^{-5} < Ca < 3 \times 10^{-3}$ Liquid-gas
Bretherton (1961)	$\delta/_R = 0.66Ca^{2/3}$	$10^{-3} < Ca < 10^{-2}$ Liquid-gas
Taylor (1961)	$\delta/_R = \frac{1.34Ca^{2/3}}{1 + 3.35Ca^{2/3}}$	$10^{-3} < Ca < 1.4$ Liquid-gas
Irandoust and Andersson (1989)	$\delta/_R = 0.335[1 - \exp(-3.08Ca^{0.79})]$	$9.5 \times 10^{-4} < Ca < 1.9$ Liquid-gas
Aussillous and Quéré (2000)	$\delta/_R = \frac{1.34Ca^{2/3}}{1 + 1.34(2.5Ca^{2/3})}$	$10^{-3} < Ca < 1.4$ Liquid-gas
Han and Shikazono (2009)	$\delta/_R = \frac{1.34Ca^{2/3}}{1 + 3.13Ca^{2/3} + 0.54Ca^{0.672}Re^{0.589} - 0.352Ca^{0.629}}$	$Ca < 4 \times 10^{-1}$ Liquid-gas
Dore *et al.* (2012)	$\delta/_R = 0.3[1 - \exp(-6.9Ca^{0.54})]$	$7 \times 10^{-3} < Ca < 1.59 \times 10^{-1}$ Liquid-liquid
Howard and Walsh (2013)	$\frac{U_b}{U_{TP}} = \frac{\left[\frac{(R-\delta)^2}{R^2}\left(\frac{\mu_f}{\mu_b} - 2\right) + 2\right]}{\left[\frac{(R-\delta)^4}{R^4}\left(\frac{\mu_f}{\mu_b} - 1\right) + 1\right]}$	$5.9 \times 10^{-3} < Ca < 1.82$ Liquid-gas
Mac Giolla Eain *et al.* (2013a)	$\delta/_R = 0.35Ca^{0.354}We^{0.097}$	$2 \times 10^{-3} < Ca < 1.19 \times 10^{-1}$ Liquid-liquid
Tsaoulidis and Angeli (2016)	$\delta/_R = 0.658Ca^{0.6409}Re^{0.1067}$	$3 \times 10^{-2} < Ca < 1.8$ Liquid-liquid

Pressure Drop

Pressure drop is regarded as a crucial metric in Taylor flow as it plays the main role in a system's overall cost as well as affecting stability, flow rate, and pump sizing. Pressure drop models are therefore necessary for the design of mechanical systems in order to accurately predict pressure drop in Taylor flows. The pressure drop for fully developed Hagen-Poiseuille flow of a single phase fluid in a capillary is determined using the friction factor. However, the frictional pressure gradient for a Taylor flow results from a combination of

shear stress at the channel wall and interfacial interactions between phases. As a result, compared to a single-phase flow, the addition of a second immiscible phase results in a noticeably higher pressure loss. There are limited analytical techniques for modeling pressure drop in Taylor flows with the most common approaches being homogeneous, separated and Taylor flow models.

The homogenous flow modeling estimates pressure drop by applying mixture properties of both phases into a conventional single phase theory. This modeling approach implies that the two-phase flow behaves as a pseudo single-phase fluid. Examples of models based on this technique are proposed by Awad and Muzychka (2008), Dukler *et al.* (1964), Cicchitti *et al.* (1959). Using single-phase flow theory, the pressure drop (ΔP_{TP}) in capillary tubes is determined by following equations:

$$\Delta P_{TP} = \left(\frac{32L}{D}\right)\left(\frac{\rho_m U_m^2}{Re_m}\right) \tag{1.7}$$

where based on the mixture properties, ρ_m, U_m and Re_m are density, flow velocity and Reynolds number respectively. In this model, choosing the appropriate thermophysical characteristics of the fluids, such as density and viscosity, is crucial for an experimental investigation of Taylor flow. In this regard, a variety of mixture models have been developed to define the mixture properties of the involved phases, with effective velocity and effective density being the most well-known models in the literature (Dukler *et al.* 1964).

Separated flow models, however model each phase independently based on its unique hydrodynamic characteristics and velocity. The correlations by Lockhart (1949) and Chisholm (1967) are the best examples of the several techniques with different degrees of sophistication that have been developed. In the separated approach, each phase is accounted separately and the resultant pressure drop is the total of each phase's individual contribution. However, this approach does not take the interfacial pressure into account. The most well-known example of correlations based on separated flow modeling is developed by Lockhart and Martinelli (1949). In 1949, Lockhart and Martinelli (1949) proposed a correlation scheme for analysing two-phase flows. Their approach was based on the assumption that the static pressure drop for both the liquid and gas phases flowing

concurrently is equal at any point along the duct. By applying this premise, they developed expressions to estimate the pressure drop in two-phase flow systems. These expressions considered four variables: D_C/D, D_D/D, α, and β. The first two variables represented the ratio of the hydraulic diameter to the pipe diameter for each phase, while the latter two represented the ratio of the true area occupied by each phase to the hydraulic area determined from the hydraulic diameters of each phase. By employing these simple pressure drop calculations,

$$\left.\frac{dp}{dx}\right|_{TP} = \frac{2f_C}{D_C}\rho {U_C}^2 = \frac{2f_D}{D_D}\rho {U_D}^2 \tag{1.8}$$

C and D in these equations stand for carrier and dispersed phases respectively.

By applying simple friction laws, i.e., $f_C \sim C_C/Re_C^n$ represents the friction factor for the liquid phase and $f_D \sim C_D/Re_D^m$ represents the friction factor for the gas phase, two-phase pressure drop could be estimated using,

$$\left.\frac{dp}{dx}\right|_{TP} = \left.\frac{dp}{dx}\right|_{C} \alpha^{n-2}\left(\frac{D}{D_C}\right)^{5-n} \tag{1.9}$$

$$\left.\frac{dp}{dx}\right|_{TP} = \left.\frac{dp}{dx}\right|_{D} \beta^{m-2}\left(\frac{D}{D_D}\right)^{5-m} \tag{1.10}$$

or

$${\phi_C}^2 = \frac{\left.\frac{dp}{dx}\right|_{TP}}{\left.\frac{dp}{dx}\right|_{C}} \sim \alpha^{n-2}\left(\frac{D}{D_C}\right)^{5-n} \tag{1.11}$$

$${\phi_D}^2 = \frac{\left.\frac{dp}{dx}\right|_{TP}}{\left.\frac{dp}{dx}\right|_{D}} \sim \beta^{m-2}\left(\frac{D}{D_D}\right)^{5-m} \tag{1.12}$$

Equations 1.11 and 1.12 involve parameters n and m, which denote the exponents on the Reynolds number in the simple friction models. As a result, for a specific combination of mass flow rates for the carrier and dispersed phases, unique values for D_C

and D_D emerge. Consequently, the values of α and β are also determined, resulting in constant values for ϕ_C^2 and ϕ_D^2 under the given flow conditions.

Another empirical parameter is also included in this model to account for the additional potential pressure drop between the two phases. This is known as the Martinelli parameter and is defined as:

$$X = \frac{\phi_C}{\phi_D} \tag{1.13}$$

Lockhart and Martinelli, based on their analysis, categorized four flow regimes by considering the values of m and n in the simple friction laws. These regimes are associated with different combinations of liquid and gas flows, namely laminar-laminar (LL), turbulent-turbulent (TT), laminar liquid-turbulent gas (LT), and turbulent liquid-laminar gas (TL). However, it is important to note that these flow regimes do not provide information about the specific flow patterns occurring within the system. While these categorizations are convenient and straightforward, they do not address the detailed characteristics of the flow patterns themselves.

The homogenous and separated modeling techniques are mainly applied to find solutions for any form of two-phase flow but are not capable of distinguishing between the various physics associated with different flow regimes. Due to their flow-regime independency, it is reported that these approaches are incompatible with Taylor flows, especially at low Reynolds numbers (Liu *et al.* 2005; Mac Giolla Eain *et al.* 2015). As a result, analytical modelling based on the unit cell concept was applied to determine the pressure drop in a Taylor flow to capture the particular hydrodynamic characteristics of such flows (Kreutzer *et al.* 2005b; Walsh *et al.* 2009). This modeling technique, which is known as Taylor flow modeling, considers three elements in estimating the total pressure drop (ΔP_T): (1) the frictional pressure drop along the carrier phase (ΔP_C), (2) the frictional pressure drop along the dispersed phase (ΔP_D), and (3) the interfacial pressure drop (ΔP_{Int}) that arises from the interfaces between phases, i.e. the differential Laplace pressures between the leading and trailing droplet caps.

$$\Delta P_T = \Delta P_C + \Delta P_D + \Delta P_{Int} \tag{1.14}$$

This model assumes fully developed laminar flow, with a parabolic velocity profile across the channel, to determine the pressure drop across the carrier phase (ΔP_C). This can be simply characterized by the Hagen-Poiseuille equation ($\Delta P = 32\mu UL/D^2$) by knowing the flow viscosity (μ), flow velocity (U), capillary length (L) and diameter (D). By taking this approach, a number of studies have investigated the pressure drop in Taylor flow regimes with the majority focusing on liquid-gas flows. In these flows, the contribution of frictional pressure drop along the dispersed phase (ΔP_D) has been neglected due to the negligible viscosity of the dispersed gas. As a result, the interfacial pressure drop (ΔP_{Int}) is determined by subtracting the carrier phase pressure loss from the overall pressure drop measured experimentally. The most well-known solution used in determining interfacial contribution was developed in a study by Bretherton (1961) using the Young-Laplace equation. Equation 1.15 represents the correlation proposed by Bretherton.

$$\Delta P_{Int} = 7.16(3Ca)^{3/2}\frac{\gamma}{D} \tag{1.15}$$

This expression was derived from a theoretical solution developed for the resultant interfacial pressure drop from a single bubble in a Taylor flow regime.

However, taking the same approach to calculate pressure drop across the droplet in liquid-liquid flows may not lead to a correct result due to the comparable viscosity of both phases (Ładosz and von Rohr 2018). In such flows, the dispersed phase viscosity cannot be neglected and varying viscosity ratios at the interface result in different velocity profiles across the droplets which have a substantial impact on pressure drop. In liquid-liquid flows, precise and reliable calculation of the frictional pressure drop along the dispersed phase is required in addition to the interfacial pressure drop's contribution. In this regard, various models have been proposed to correlate the pressure drop in the dispersed phase while primarily highlighting the need for determining the role of film thickness. Two different correlations assuming a stagnant or moving film were developed to determine the frictional pressure along the dispersed phase in liquid-liquid Taylor flows (Jovanović *et al.* 2011; Gupta *et al.* 2013). Figure 1.8 illustrates the arrangement of a droplet in Taylor flow with the velocity profile, film thickness δ, channel radius R and flow direction highlighted.

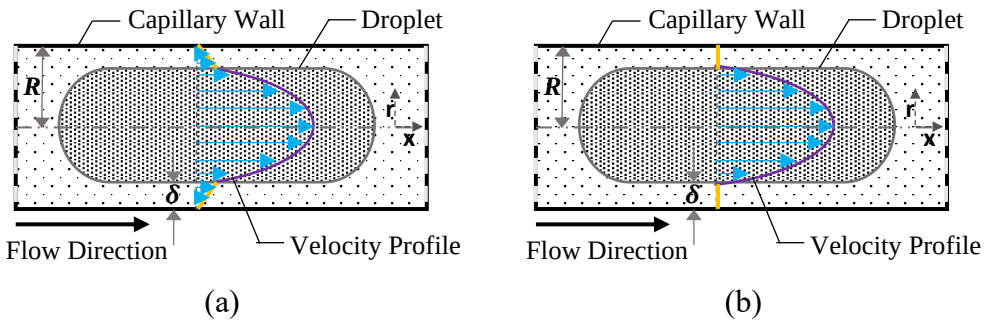

Figure 1.8. Schematic of the velocity profile across the capillary by assuming (a) a moving-film and (b) a stagnant-film.

The moving-film and stagnant-film models, given in equations 1.16 and 1.17 respectively, are the most well-known models in the literature for estimating pressure drop in liquid-liquid Taylor flows. Both models use the theoretical solution of Bretherton to determine the pressure drop caused by interfacial tension between phases.

$$\frac{\Delta P_T}{L} = \frac{8\mu_C U(1-\varepsilon)}{R^2} + \frac{4U_D\varepsilon}{\frac{(R^2-(R-h)^2)}{\mu_C} + \frac{(0.5(R-h)^2)}{\mu_D}} + \frac{1}{L_u} 7.16(3Ca_C)^{2/3}\frac{\gamma}{D} \qquad (1.16)$$

$$\frac{\Delta P_T}{L} = \frac{8\mu_c U(1-\varepsilon)}{R^2} + \frac{8\mu_D U_D\varepsilon}{(R-h)^2} + \frac{1}{L_u} 7.16(3Ca_C)^{2/3}\frac{\gamma}{D} \qquad (1.17)$$

The stagnant-film model assumes a considerable contribution of the dispersed phase in the total pressure drop and the moving-film model assumes a significant role of the thin liquid film, which separates the slugs (dispersed phase) from the capillary wall, in the total pressure drop. It was discovered that the film velocity had very little influence on the pressure drop. As a result, the mathematically straightforward stagnant-film model was determined to be sufficiently accurate for modelling the pressure drop caused by slug flows.

Following these previous studies, Mac Giolla Eain *et al.* (2013b, 2015) conducted an experimental study over a range of variables, including Capillary and Reynolds numbers, resulting in two different correlations predicting pressure drop in Taylor flows. First, they proposed a correlation to determine the skin-friction coefficient for liquid-liquid slug flows by focusing on the interfacial contribution in overall pressure drop (Mac Giolla Eain *et al.* 2013b). The proposed correlation showed good agreement with experimental results as the majority of the data points were positioned within the 15% error bandwidth

of the model. Subsequently, they developed a universal model to predict pressure drop in both liquid-liquid and liquid-gas slug flows in the form of frictional losses (Mac Giolla Eain *et al.* 2015). This model was attained by modifying a model proposed by Warnier *et al.* (2010) (for liquid-gas slug flows). Table 2 gives a summary of investigations on the pressure drop of liquid-liquid Taylor flows in mini/micro channels.

Table 1.2. Recently published studies on pressure drop in liquid-liquid Taylor flows in mini / micro channels.

Author(s)	Approach	Geometry	Remarks
Kashid and Agar (2007)	Experimental Taylor flow Lockhart-Martinelli	Capillary microreactor D= 0.25−1 mm	A theoretical prediction for pressure drop was developed across capillary and Y-junction.
Salim *et al.* (2008)	Experimental Homogeneous Lockhart-Martinelli	Quartz & glass microchannels Dh=793 and 667 μm	Pressure drop strongly depends on flow rates, channel material, and the primary fluid.
Aota *et al.* (2009)	Experimental Taylor flow	Microchips (glass microchannel) Dh=215 and 33 μm	Pressure drop model was proposed for liquid-liquid interfaces of the two-phase slug flow.
Jovanović *et al.* (2011)	Experimental Taylor flow	Microcapillary D=248 and 498 μm	Two pressure drop models was developed for liquid-liquid slug flow as the sum of frictional pressure drop and interface pressure drop.
Tsaoulidis *et al.* (2013)	Experimental Taylor flow	Teflon, glass microchannels Dh=200 and 270 μm	By considering the film thickness, a model was proposed to estimate pressure drop of liquid-liquid Taylor flows.
Gupta *et al.* (2013)	Experimental Numerical Taylor flow	Circular minichannel D=1.06 mm	A correlation was developed to determine the total pressure drop in a fully- developed unit cell.
Mac Giolla Eain *et al.* (2013b)	Experimental Taylor flow	Teflon circular tubes D=1.6mm	A correlation was developed to estimate the interfacial contribution to the total pressure drop in a liquid – liquid slug flow regime.
Marc Mac Giolla Eain *et al.* (2015)	Experimental Taylor flow	Teflon circular tubes D=1.6 mm	A universal model was developed to estimate pressure drop in both liquid-liquid and liquid-gas flow.
Li and Angeli (2017)	Numerical Taylor flow	Quartz microchannels Dh=0.2 and 0.5 mm	The pressure profile along the channel was predicted for liquid-liquid slug flows.

Unfortunately, despite several attempts to develop an all-encompassing model to estimate pressure drop in immiscible liquid-liquid Taylor flows, existing models are still limited to a narrow ranges of flow conditions. Research on liquid-liquid flows is still in its early stages compared to liquid-gas flows, which calls for greater efforts to fill the data gaps in the flow hydrodynamics.

1.2.5. Summary

Liquid-liquid flows offer significant advantages in heat and mass transfer, making them valuable in various microfluidic applications, such as biological engineering, pharmaceuticals, electronic cooling, and chemical engineering. As the demand for microfluidic devices utilizing these flows continues to grow, there is a pressing requirement for a deeper understanding of their behaviour to enhance engineering and device development. Despite their potential, research on liquid-liquid flows is still in its early stages compared to liquid-gas flows, underscoring the need for greater efforts to fill the existing data gaps in flow hydrodynamics. A concerted effort to expand the knowledge base and develop robust predictive models is essential to fully harness the potential of liquid-liquid flows in microfluidics and beyond. Addressing the existing challenges in modelling liquid-liquid flows will not only advance the fundamental understanding of these flows but also open up new possibilities for designing efficient and reliable microfluidic devices across a wide spectrum of applications.

Chapter 2

Slug Flow Applications

The subset of microfluidics known as droplet-based microfluidics has successfully provided a wide range of applications in the fields of biology, chemistry, and engineering. Illustrations of some of these applications and potential future applications are shown in Figure 2.1.

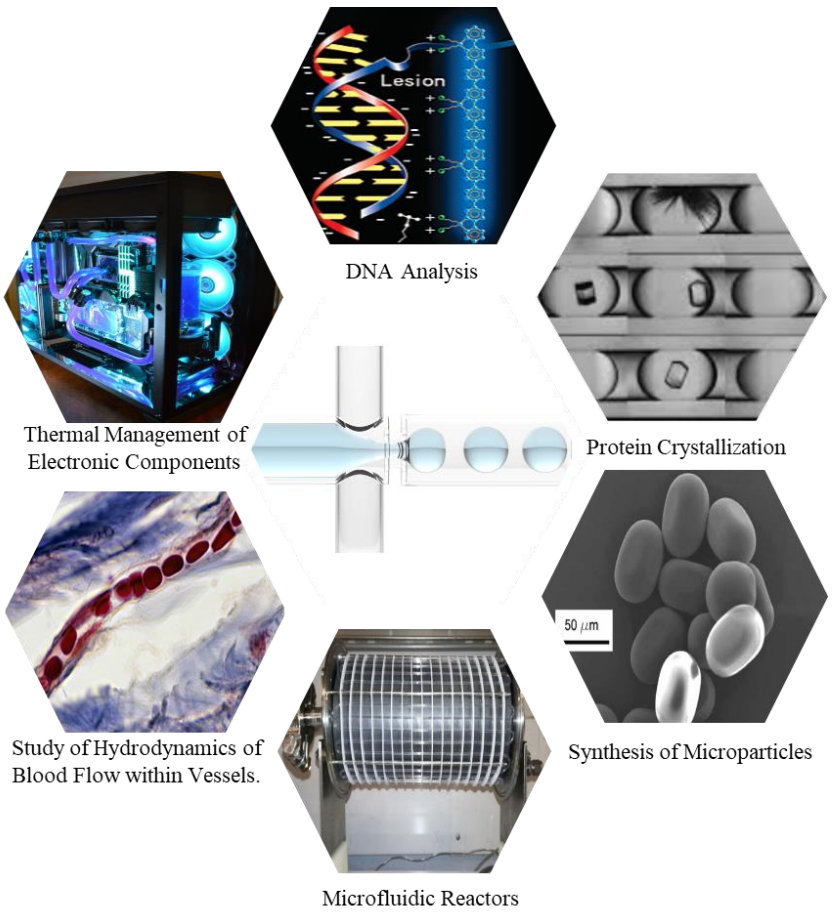

Figure 2.1. Examples of applications in various areas benefitting from two-phase flows to enhance performance (Dendukuri *et al.* 2005; Duan *et al.* 2010; Gerard *et al.* 2018; Gettyimages 2022).

Among different implemented flow configurations, the “slug format”, in which droplets are tightly packed inside a capillary, is the most appropriate for applications requiring multi-step assays. In such flows, each droplet takes an elongated shape and flows as an independent carriage, in a train, which may contain different chemicals. Due to this distinct characteristic, such flows have been used in a number of biological applications including DNA analysis and protein crystallization, enabling fast and cheap processes without the need for intricate instruments. In such flows, droplets never come into contact with the channel wall as a thin lubrication film from the continuous liquid engulfs them. This thin film plays an important role in reducing cross-contamination and minimizing material waste. Considering this, slug flows have also opened up a promising field in chemistry with a variety of practical applications, such as microparticle synthesis and chemical reactions. Slug flows in microchannels, with a high surface area to volume ratio and internal circulations within the slugs, not only offer a high mass transfer between phases but also result in enhanced heat transfer rates from the channel wall. Today’s electronic components with extremely high dissipation rates are the upcoming customers of slug flows calling for high performance heat sinks to maintain their integrity and endurance. This requires further research into the various facets of slug flows as they are yet to be integrated into real-world cooling systems outside of research labs.

The benefits of slug flows in microfluidic devices may also come with a pressure drop penalty. As a result, developing predictive correlations based on experimental and numerical research is essential for further advancement in this area. Such correlations, which can be employed as performance factors for the relevant microfluidic devices, must create a relationship between the pressure drop and the desired outcome, ie., heat transfer in applications where slug flow is used for cooling purposes. In this regard, it is necessary to correctly analyze the flow hydrodynamics by using high precision measurement tools to develop more reliable correlations for slug flows. To attain a higher performance, establishing methods and tools that have precise control over the flow parameters can be greatly advantageous. Chemists and biologists are undoubtedly interested in developing fresh tools and strategies to control and manage the droplet, since their investigations necessitate precise control on the volume of the substances and establishment of specific set of conditions.

This chapter's objective is to give an overview of the applications of two-phase flows in mini and microchannels in addition to how this study contributes to the further

development of these applications. The applications are divided into two categories; chemical and biomedical, and thermal management which are presented in sections 2.1 and 2.2 respectively. An overview of existing microfluidic droplet sensing techniques as well as the associated challenges are provided in section 2.3. Finally, the objectives of this study and the thesis outline are described in sections 2.4 and 2.5 respectively.

2.1. Chemical and Biomedical Applications

Liquid-liquid Taylor flows have a diverse spectrum in chemical engineering and biomedical applications. By adopting chip-based microchannel platforms, chemical and biomedical processes can be performed in smaller scales which brings numerous advantages such as a higher mixing rates, a reduction in the generation of by-products in sequential reactions and an exceptionally narrow residence time distribution. Microreactors, both single channel and multichannel, are examples of chemical applications that benefit from microdroplet systems. Monolithic reactors with a honeycomb structure catalyst are a type of multichannel microreactor that consist of a block of parallel channels with hydraulic diameters ranging from 0.3 to 3.1 mm and an active catalyst coated on their internal surfaces (Bauer *et al*. 2006). For catalytic reactions, slug flows are the optimal choice (Kreutzer *et al.* 2005a) since they open up new process windows with considerable process intensification, resulting in improved selectivity, lower risks, and higher efficiency through long-term operation modes near the optimal working point (Ern *et al*. 2012). Liquid-liquid Taylor flows also present a novel approach for the synthesis of monodispersed solid particles with diameters ranging from 20 to 1000 nm. Xu *et al.* (2005) used a microfluidic device to create monodispersed liquid droplets that were shaped in a microchannel and solidified in place by either polymerizing a liquid monomer or by cooling the liquid that sets thermally. The multiple droplet-creating mechanisms used in this technology allow for the use of a wide variety of materials, including metals, polymers, and gels, and may be scaled up to produce extensive quantities of particles.

Microfluidic droplets also have a key role in revolutionizing diagnostic DNA testing by introducing cutting-edge analytical tools. Since the 2010s, technological advancement in microfabrication gave birth to a new age in analytical chemistry, owing to the well-defined and reportedly easy-to-control flow structures which allow for the adjustment of droplet formation frequency and various droplet characteristics (Ward *et al.*

2005; Cao *et al.* 2018). Genetic analysis is one of the most successful examples of using droplet microfluidics which has the potential to meet the needs and challenges in genotyping for downsizing, reproducibility, and automation (Hosokawa *et al.* 2017). This technique dramatically reduces reagent usage, waste and cost by using an immiscible carrier fluid (for instance, oil) to discretize a single sample into thousands of individual reactions that are similar to independent and separated workbench reaction tubes but several times smaller in volume. Moreover, since droplets can be created and transferred at very high frequency rates, they are also capable of collecting a large number of data points in a short amount of time (Bardin *et al.* 2013). Figure 2.2 shows a schematic of a droplet-based microfluidic system for genotyping corn genomic DNA.

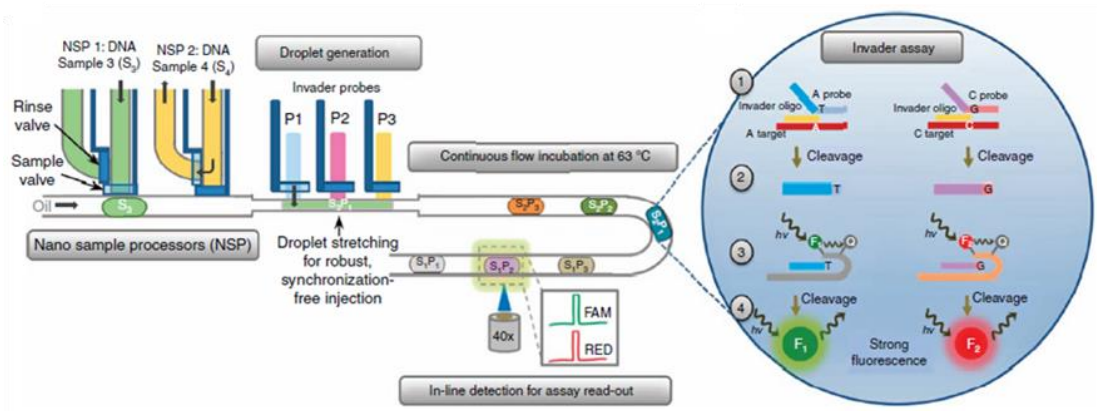

Figure 2.2. Two NSPs are used to successively load DNA samples into the microfluidic device, and programmable sample valves are activated when needed to digitalize the samples into 5 nL droplets. When the DNA droplets reach the droplet-generation zone, the narrow channel leads them to spread out and cover the whole area, enabling synchronization-free injection of 45 nL of Invader probes and reaction mix into the DNA droplets upon activating the relevant probe input valves. A two-color fluorescence spectroscopy detection system is used for in-line monitoring. The final allelic call out for particular DNA and probe is then obtained using fluorescence signals (Zec *et al*. 2018).

Additionally, liquid-liquid microfluidics provides a promising tool for the observation and manipulation of crystallization processes, such as in the production of crystals with a controlled size (Dombrowski *et al.* 2007). High throughput, less sample and reagent usage, quick mixing, and little cross-contamination are all benefits of using droplet-based microfluidic systems in crystallization procedures (Candoni *et al.* 2019). In chemical and biological sciences, crystallization is employed for molecular separation, purification procedures, product property control, and diagnostic objectives (Veesler and Puel 2015). Protein crystallization is a crucial step in determining the 3D structure of proteins by X-ray

diffraction (XRD) which helps in the assessment of their biological properties (Candoni *et al.* 2012). Figure 2.3 illustrates an example of microfluidic devices applied to protein crystallization. In crystallization from a solution, nucleation initiates the process and it is a crucial step in determining the physical characteristics of crystals (Kashchiev 2000). The majority of crystallization experiments are carried out in milli or microreactors (Galkin and Vekilov 2000; Svärd *et al.* 2010; Jiang and Horst 2011) with the need to know the exact location of the droplets, carrying crystals, for real-time analysis.

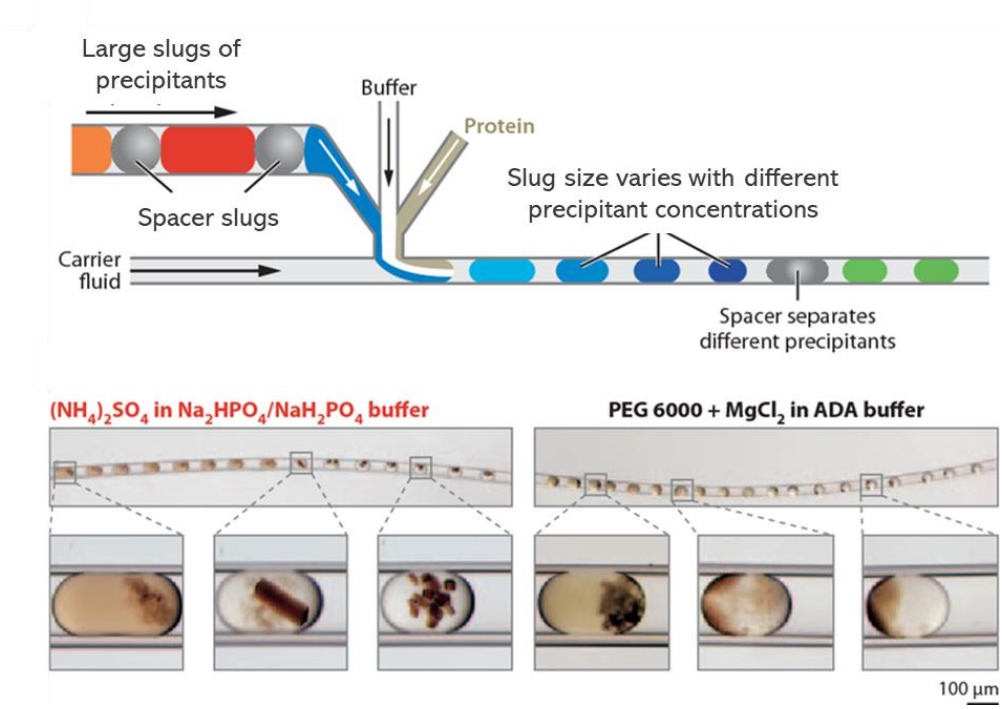

Figure 2.3. A microfluidic droplet technique to monitor crystallization conditions employing the micro-batch method (Li *et al.* 2006).

In all of the mentioned chemical and biomedical applications, the precision and predictability of the processes can be severely impacted by a phenomenon called droplet coalescence or droplet merging. In order to accurately regulate this phenomena, it is necessary to have a comprehensive grasp of the key factors that influence droplet velocity. It has been shown by various studies that several parameters affect droplet mobility in liquid-liquid flows. These include channel geometry, droplet size, presence or absence of surfactants, flow velocity, liquid viscosities and interfacial tension (Jakiela *et al.* 2011). As a result, developing a model to predict droplet velocity has become a serious challenge among researchers. In this regard, several attempts have been carried out over the last two decades to characterize the dispersed phase in two-phase flows within milli and microscale

channels. Most existing studies were aimed at liquid-gas flows (Bretherton 1961; Schwartz *et al.* 1986; Abiev 2017; Zhang *et al.* 2017) with only a few focusing on liquid-liquid flows (Hodges *et al.* 2004; Vanapalli *et al.* 2009; Jakiela *et al.* 2011). As such, the physical behaviour of liquid-liquid flows is still not fully understood. In addition, most research on liquid-liquid flows has focused on low viscosity fluids as the dispersed phase, with limited studies reporting on a high viscosity droplet being carried by fluid of a low viscosity. A low viscosity liquid, as the carrier phase, results in lower energy consumption and reduced overall cost of the operation due to a smaller pressure drop across the channel (Mukhaimer *et al.* 2015). Moreover, droplets that are larger than the channel size, are squeezed and their contact with the channel walls is avoided by the presence of a thin film of continuous phase. The viscosity of this lubricant film can significantly affect the droplet's internal mixing as well as droplet velocity and transfer (Baroud *et al.* 2010; Ferraro *et al.* 2019). Therefore, further investigation is necessary to understand the hydrodynamics of Taylor flows with a low viscosity liquid as the carrier fluid.

In this regard, part of the current study is focused on the experimental investigation of droplet mobility in liquid-liquid flows with the objective of determining the effect of droplet size and viscosity ratio on droplet velocity within mini and micro capillaries. A model is developed to predict droplet velocity with a high degree of accuracy. This model may pave the way for improved process modelling linked to Taylor-droplets in milli and micro channels by estimating droplet velocity and also revealing effective parameters. Transportation, analysis, detection, and monitoring are among the procedures applied in biological or chemical applications, each needing precise spatial and time control data for droplets.

2.2. Thermal Management Applications

In the close future, the generated heat flux in computer electronic components is projected to increase from $300\ W/cm^2$ to $500\ W/cm^2$, with hot spots approaching $1000\ W/cm^2$ or higher (Chai *et al.* 2013; Smakulski and Pietrowicz 2016; Ghani *et al.* 2017; Prajapati and Bhandari 2017). The current generation of microprocessors dissipate heat fluxes over $50\ W/cm^2$ and in some cases, small semiconductor devices such as power amplifiers (area ~1 cm^2), which are used for 5G network antennas, dissipate a huge amount of heat of order

$10^2\ W$. The fifth generation (5G) of wireless networks is anticipated to enable the ubiquity of interconnections for billions of gadgets as well as the opening of several new services through the transmission of data at multiple gigabits per second. Broad frequency bands, such as those at millimetre wave (mm-wave), have been earmarked for 5G in order to address the constantly growing demand for higher rates of data transmission (Rappaport *et al.* 2013). However, mm-wave transmissions lead to very low power amplifier efficiency (less than 20%) and a smaller receiving effective aperture (Hanafi 2014). To mitigate these challenges and offer more favourable RF link budgets, large scale antenna arrays with hundreds of components have been shrunk into considerably small base stations. A single 5G base station uses 2.5 to 3.5 times more power than a 4G station despite having a substantially smaller footprint, which results in excessive heat dissipation in a very small space (Li *et al.* 2021). Therefore, several of the hardware components included in 5G infrastructures face substantial thermal challenges, necessitating the development of innovative thermal management solutions as conventional heat spreaders such as forced convective air cooling systems or single phase flows are no longer effective. A second example of electronic components with high heat dissipation rates are IGBTs (Insulate Gate Bipolar Transistor). These devices are used in radar transmitters and power electronics and can generate heat fluxes up to $200\ W/cm^2$ (Thome and Cioncolini 2017). Such electronic devices are primarily made of silicon which cannot tolerate high thermal stresses. Hence, a cooling system providing low temperature gradients is required to maintain components at, as near an isothermal condition as possible to prevent system failure.

Forced convective cooling using air enables us to almost reach a heat flux of up to $150\ W/cm^2$ (Hamann *et al.* 2006) however in some cases such as laser diode arrays heat fluxes can skyrocket to 1000 W/cm^2 (Roy and Avanic 1996; Bandhauer and Bevis 2016). In these cases, applying direct liquid cooling, such as pool boiling, jet impingement (Jeffers *et al.* 2009; Hotta and Patil 2018), and spray cooling (Tilton *et al.* 1989; Fabbri *et al.* 2005) can provide high heat transfer rates by taking advantage of the latent heat of a liquid. Due to the high heat of vaporization, the heat transfer rate for boiling flow in microchannels is significantly larger than that of its single-phase counterpart. It has been shown that boiling flow is able to disperse heat at a rate of $10\ kW/cm^2$, which is ten times greater than for single phase flow (Mudawar and Bowers 1999). However, flow boiling has the drawback of being challenging to control due to back flow and flow instability. In addition, such techniques are more complex from a use and design point of view which require additional

maintenance procedures for hot swapping electronic parts (Ebadian and Lin 2011). Therefore, high performance heat sinks are urgently needed to maintain the integrity and endurance of today's electronic gadgets.

As traditional cooling systems are unable to fulfill such demands, the use of microchannel heat sinks (MCHS) has received considerable attention in research as an alternative method for heat removal from microelectronic systems. MCHS were first proposed by Tuckerman and Pease (Tuckerman and Pease 1981) and have since been widely employed in industrial applications owing to their intrinsic benefits of greater heat transfer performance, smaller size and volume, lower coolant consumption, and lower operating costs (Gao *et al.* 2022). It is widely recognized that using MCHS in collaboration with other technological innovations can address the extremely complicated thermal challenges that industries are currently facing, including those related to 5G devices, micro-electromechanical system (MEMS) systems, fuel cells, as well as the medical/biological and energy sectors (Gao *et al.* 2022). Moreover, introducing a periodic secondary flow within MCHS, can significantly improve the heat transfer coefficient by interrupting the thermal boundary layer, improving flow mixing, and increasing flow turbulence. Furthermore, because liquids have a much higher thermal capacity than gases, using a liquid instead of a gas bubble as the dispersed phase results in much higher heat transfer rates. Several experimental and numerical studies have shown enhanced heat dissipation rates up to 700% compared to traditional single phase flows (Mac Giolla Eain *et al.* 2015; Abdollahi *et al.* 2020a). Using high resolution infrared thermography, Mac Giolla Eain *et al.* (2015) carried out an experimental investigation of the heat transfer in liquid-liquid Taylor flows in a circular tube. According to this study, utilizing two immiscible liquid phases increases heat transfer performance by up to 600%. Following this work, a computational analysis by Abdollahi *et al.* (2020a) revealed that liquid-liquid Taylor flows could increase heat transfer over single phase flows by up to 700%. Table 2.1 provides an overview of the experimental and numerical studies on the heat transfer of liquid-liquid two phase flow in microchannels. These studies are carried out within circular and rectangular channels, ranging in size from $100\ \mu m$ to $2\ mm$, with water as the dispersed phase. Water with a high specific heat capacity ($C_p \approx 4\ kJ/kg.K$) is a common liquid coolant providing cheap and high heat transfer.

Table 2.1. A summary of recent research on the thermal behaviour of liquid-liquid Taylor flows within mini and micro scale channels.

Author(s)	Geometry	Working fluids	Findings
Urbant *et al.* (2008)	2D axisymmetric geometry with inner diameter of 100 μm	Mineral oil-Water	Heat transfer rate noticeably enhanced by introducing oil drops in water. Nusselt number augmented by elongating the oil droplets.
Fischer *et al.* (2010)	2D axisymmetric geometry with inner diameter of 0.1–1 mm	Water-5 cS Silicon oil or PAO	Nusselt number enhanced up to 400% in comparison with single liquid fluid.
Asthana *et al.* (2011)	Serpentine microchannel with cross section of 100 × 100 μm	Water-light mineral oil	Recirculation in continuous fluid interrupts the boundary layer. Water-oil Slug flow Nusselt number was about four times higher than pure water.
Mac Giolla Eain *et al.* (2015)	1.5 mm circular tube	Pd5, Dodecane and AR20 silicon oils-water	Heat transfer rate enhancement by decreasing carrier slug length and increasing dispersed slug length. Decreasing heat transfer by thickening liquid film. The addition of a second immiscible liquid phase resulted in heat transfer enhancements up to 600%.
Dai *et al.* (2015)	2 mm circular tube	Water-hexadecane	Experimental heat transfer rates well agreed with numerical predictions. A correlation developed based on heat transfer from wall to film region and from film to slug.
Che *et al.* (2015)	3D 200×(200–800)×800 μm microchannel	Water-mineral oil	Nusselt number decreases by increasing Pe number. Nusselt number enhancement by reducing aspect ratio.
Bandara *et al.* (2015)	2D axisymmetric geometry with inner diameter of 100 μm	Water-light mineral oil	Nusselt number increases up to 200% compared to single phase flow. Increasing slug length decreases the Nusselt number.
Abdollahi *et al.* (2020a)	Square channel with a hydraulic diameter of 1 and 2 mm.	Hexadecane, kerosene and water	Liquid-liquid Taylor flow can increase heat transfer rate up to 700 percent. Nusselt number is almost independent from two-phase velocity for $Ca < 0.005$.

In the design of all types of heat exchangers, pressure drop is the main governing factor in determining input power and system cost. Knowledge of the exact power consumption is necessary to secure a desirable flow rate. In this regard, unbiased and reliable experimental data is necessary for both the assessment of mathematical models and the development of physically based pressure drop correlations. Many efforts have been made in recent years to gain a better understanding of pressure drop in two-phase Taylor flows. Despite the fact that liquid-liquid slug flows show a better thermal performance and

have received more attention in chemical and biomedical applications, only a few studies have been conducted on modelling pressure drop in liquid-liquid slug flows, according to a review by Etminan *et al.* (2021). Most of the research to date has focused on liquid-gas rather than liquid-liquid flows with researchers hoping to generalize the results to other test conditions. However due to the complicated hydrodynamics of two-phase flows, extrapolations of correlations beyond the limits for which they were derived, may lead to poor predictions. Moreover, the existing correlations for liquid-liquid flows are based on experiments involving flows with carrier to dispersed phase viscosity ratios greater than unity. This is similar to liquid-gas flows where the viscosity of the carrier phase is always much greater than the dispersed phase and results in negligible frictional losses due to the dispersed phase. However, in liquid-liquid flows, a liquid with a comparably low viscosity can be used to segment the dispersed phase of a relatively higher viscosity. This results in an increased contribution of the dispersed phase to pressure drop, adding to the complexity of such flows. In addition, depending on the viscosity ratio of the involved fluids, the interfacial tension can significantly influence the overall pressure drop (Mac Giolla Eain *et al.* 2015). In microfluidic devices, the transport, synthesis, and diagnostics of high-viscosity materials is a big challenge due to the high flow resistance which requires a significantly high energy cost to pump material through a miniaturized system. In an effort to minimize pressure drop and overall energy cost, low-viscous carrier fluids have been employed to envelop highly viscous liquids in a variety of scientific and engineering applications, including lubricated pipelining (Joseph and Renardy 2013), multi-component polymeric flows (Everage Jr 1973; Khomami and Su 2000), and volcanic conduits (Carrigan and Eichelberger 1990). In such applications, the carrier phase functions as a lubricant to prevent the high-viscous fluid from being directly in contact with the channel wall and results in lower pressure drop.

In this regard, this thesis is focused on the development of a model for predicting the pressure drop in liquid-liquid Taylor flows over a range of effective parameters which includes the viscosity ratio of involved phases. This aids in the further development of microfluidic devices that rely on such flows and provides greater insights into the subject through an analysis of parameters affecting pressure drop in liquid-liquid flows.

2.3. Microfluidic Droplet Sensing Techniques

To attain the best performance in applications that benefit from slug flows, designers must have a thorough understanding of the flow configuration. Due to the small physical dimensions of such microfabricated devices, non-intrusive measurement techniques with high resolution are required to assess flow properties.

In recent decades, microchannel flows are studied using a range of imaging techniques. The most common method is optical microscopy, which involves illuminating the flow from underneath with a powerful light source and inspecting it from above using a camera with a short shutter length. This method typically needs complicated and expensive instrumentation, such as microscopes with integrated high-speed cameras and a powerful light source, restricting adaptability and providing only narrow-time assessments (Robert de Saint Vincent *et al*. 2012). Furthermore, the accuracy of the data obtained is heavily reliant on the camera's resolution and the operator's skill. Optical distortion caused by curved channel walls or varying refractive index may also cause significant measurement inaccuracy. Particularly, in circular microchannels with extremely small radii, optical distortion is a major issue for flow imaging. In addition, this technique does not allow in-line assessment and to obtain results, post processing of images is necessary. In an effort to overcome some of the difficulties associated with measurements made using the imaging techniques, Jakiela *et al.* (2011) employed linear camera imaging to capture only the channel's centreline. This method enables in-line measurements of droplet length and velocity by collecting necessary data and accelerating data processing by simply identifying the front and rear caps of the droplet. However, this method still requires a microscope with an integrated high-speed camera and brings uncertainty to the measurements due to the optical distortion.

In addition to the visual methods, there are alternatives based on changes in the fluid’s electrical characteristics caused by the presence of a second phase. Based on the different electrical resistances of the phases, resistive approaches are often utilized in cytometry to detect the presence of the droplets (Sun and Morgan 2010). However, this technique cannot provide an exact measurement of droplet length and velocity. A capacitive measurement was also developed by Niu *et al.* (2007), which detects the passing of a droplet and determines its velocity by means of suitable signal post-processing. But, this approach gives less confidence in length measurements as a result of signal convolution.

Capacitive sensors are generally used in microelectromechanical systems (MEMS), commonly to sense pressure and acceleration (Eaton and Smith 1997; Berggren *et al.* 2001). It is crucial to keep in mind that each of these electrical approaches requires intricate microfabrication and electrode implantation within the channel.

It is also possible to explore the instantaneous flow conditions by means of tracer-based measuring techniques. Unfortunately, adding tracers inevitably contaminates the fluidic system, which results in disrupted local hydrodynamics and triggered chemical reactions. This is why the use of measurement techniques such as particle image velocimetry (PIV) or light-induced fluorescence (LIF) is primarily reserved for early research and development objectives.

Thus, researchers have found it challenging to develop precise and suitable apparatus for in-line assessment and manipulation of flow characteristics in microscale two-phase flows. Especially, in microfluidic cell analysis systems which require new approaches for cell assays and high-speed cell manipulation.

In order to address the above mentioned challenges, the current study suggests a novel measurement technique for investigating flow properties in both liquid-liquid and liquid-gas slug flow regimes. Regardless of channel shape, this non-intrusive approach allows in-line measurements of both carrier and dispersed phase length and velocity with excellent precision. This measurement methodology will aid in determination and analysis of two-phase flow configurations in transparent microchannels, enabling optimization of the applications that profit from such flows.

2.4. Objectives

This thesis features the development of semi-empirical correlations to predict the pressure drop in microfluidic liquid-liquid Taylor flows and the drift velocity (velocity difference between the instantaneous droplet velocity and the mean flow velocity) of Taylor droplets in circular micro and mini channels. The strategy that has been chosen can be regarded as an analytical-experimental methodology that combines theoretical and experimental analyses. Subsequent to obtaining measurements, the effective parameters are employed to correlate the experimental data by means of a linear data regression while ensuring adherence to the subject's theoretical principles. The essential procedures of modelling have been divided into four sequential steps:

I: The strengths and weaknesses of existing models are identified and a more fundamental understanding of the Taylor flow regime is developed.

II: A novel, fully automated experimental setup was designed to accurately measure the desired parameters.

III: A model containing effective parameters is introduced through a thorough parametric analysis. This model is developed using a linear data regression and satisfies the theoretical foundations of the subject.

IV: The experimental data is compared with the new model to evaluate the accuracy of the model.

The objectives of the current thesis are:

- Establishing a non-invasive measurement method capable of conducting long-term measurements in micro-scale Taylor-flows and extracting desired parameters. By assisting in the identification and analysis of two-phase flow configurations in transparent microchannels, this measuring methodology will enable the optimization of applications that benefit from such flows.
- Measuring the pressure drop in liquid-liquid Taylor flows and determining the influence of flow characteristics upon its magnitude.
- Identifying the limitations with existing models and developing a new correlation, if necessary, to improve current predictions of pressure drop in liquid-liquid Taylor flow.

- Measuring droplet velocity in liquid-liquid flows with the objective of determining the effect of droplet size and viscosity ratio on droplet velocity within mini and micro capillaries.
- Developing a new expression, if necessary, to better estimate the velocity of droplets which accounts for all the effective parameters. This requires thorough analysis and evaluation to ensure high reliability in predicting the droplet velocity under varying conditions.

2.5. Thesis Structure

The remaining chapters of this thesis are organized as follows:

Chapter 3 contributes to the advancement of microfluidic droplet sensing techniques incorporating Taylor flows and gives a more comprehensive understanding of this flow regime by identifying the limitations with existing measurement techniques. A novel technique is developed to easily and reliably measure slug length and velocity. This technique is also used to ensure high accuracy and repeatability of all measurements carried out in the course of this thesis.

Chapter 4 details the findings of the droplet velocity measurements within mini and micro capillaries over five different fluid combinations. The chapter provides greater insights into the subject through an analysis of parameters affecting droplet mobility in liquid-liquid Taylor flows. The results highlight a complex relationship between droplet velocity and droplet length, viscosity ratio and Bond number. Finally, a new expression is developed to better estimate the velocity of droplets which involves all the effective parameters.

Chapter 5 includes experimental and theoretical studies on the pressure drop of liquid-liquid Taylor flows in micro capillaries. The strengths and weaknesses of existing models are identified and a new approach is developed to estimate the pressure drop over wide ranges of effective parameters. The new correlation offers a reliable prediction tool for estimating pressure drop in applications that deal with such flows.

Finally, **Chapter 6** summarizes the main findings of this research and includes further recommendations for future research on microfluidic liquid-liquid Taylor flows.

Chapter 3

Real-Time Measurement Technique for Slug Flow Characterization

Real-Time Measurement Technique for Slug Flow Characterisation

Chapter on Published Journal Article:

Journal of Fluid Flow, Heat and Mass Transfer[1]

Date: December 2022

Seyyed Saeed Shojaee Zadeh*[a], Vanessa Egan[b], Pat Walsh[c]

*****Corresponding Author

a CONNECT Centre, Stokes Laboratories, Bernal Institute, School of Engineering, University of Limerick, Ireland, V94T9PX. E-Mail: saeed.zadeh@ul.ie, Tel:+353873818619, ORCID: 0000-0003-1359-7232

b CONNECT Centre, Stokes Laboratories, Bernal Institute, School of Engineering, University of Limerick, Ireland, V94T9PX. E-Mail: vanessa.egan@ul.ie, ORCID: 0000-0001-8828-6303

c Stokes Laboratories, Bernal Institute, School of Engineering, University of Limerick, Ireland, V94T9PX. E-Mail: pat.walsh@ul.ie

DOI: 10.11159/jffhmt.2022.023

Abstract

To achieve accurate slug lengths and velocities in a slug flow regime, monitoring of the droplet/bubble train is an essential stage which necessitates the use of proper techniques. In most experiments, the traditional measurement apparatus consists of a high-speed camera coupled to a microscope which are employed to characterize such flows in microchannels. However, when using these techniques, optical distortion caused by the curved channel walls can result in large measurement uncertainty which undermines the measurement accuracy. In this regard, this study introduces a novel technique to easily and reliably measure slug length and velocity. This automated, non-intrusive measurement technique allows for in-line high-frequency droplet/bubble detection and related physical properties based on changes in the light intensity caused by a phase shifting in liquid-liquid or liquid-gas flows.

Keywords**:** slug flow, non-intrusive technique, in-line, high-frequency.

[1] See Appendix A for publication reference.

3.1. Introduction

Slug flow, also commonly known as Taylor flow, consists of two immiscible fluids moving within a channel. One of the fluids, the carrier phase, wets the channel wall and entirely engulfs the second fluid known as the dispersed/droplet phase. The second phase is present as discrete slugs/droplets within the carrier phase. In microchannels, slug flows have the advantage of high surface-to-volume ratios and internal circulations which not only promote thermal transfer from the channel wall but also mass transfer between phases (Kreutzer *et al.* 2005a; Kashid *et al.* 2010; Abdollahi *et al.* 2020a). Numerous experimental and numerical studies have demonstrated higher heat transfer rates of up to 700% when compared to standard single phase flows (Mac Giolla Eain *et al.* 2015). Slug flows are also used in microreactors, microfiltration, and catalytic processes to increase mixing rates and efficiency (Burns and Ramshaw 2001; Cybulski and Moulijn 2005; Qian *et al.* 2012).

Droplet-based microfluidic devices can now be employed in a variety of exploratory experiments, including those involving protein crystallization (Devos *et al.* 2021), DNA analysis (Adampourezare *et al.* 2021) and polymer particle formation (Seo *et al.* 2005). Such chemical reactions can be carried out in well-defined reaction volumes ranging from nanoliters to picoliters, thanks to the use of droplet-based microfluidic systems (Huebner *et al.* 2008). In this regard, numerous techniques for high – throughput analyses of droplet contents as well as techniques for generating and manipulating droplets in microfluidic devices have been developed (Thorsen *et al.* 2001; Anna *et al.* 2003; Song and Ismagilov 2003; Link *et al.* 2006). The characterization of key variables such as the droplet size, velocity, and frequency is one of the primary concerns in the development of these microfluidic applications. Due to the small physical dimensions of such microfabricated devices, non-intrusive measurement techniques with high resolution are required to assess the flow properties. Non-invasive measurement techniques that have been previously used include optical techniques, using a high speed camera and a microscope (Weber *et al.* 2013), capacitance, using coplanar electrodes (Isgor *et al.* 2015), and voltammetry, using two electrodes (Gu and Fisher 2013).

In recent decades, microchannel flows are commonly studied using imaging techniques. The most common method is optical microscopy, which involves illuminating the flow from underneath with a powerful light source and inspecting it from above with a short camera shutter length. This method typically requires complicated and expensive instrumentation, such as microscopes with integrated high-speed cameras and a powerful

light source, restricting adaptability and providing only narrow-time assessments (Robert de Saint Vincent *et al.* 2012). Furthermore, the accuracy of the data obtained is heavily reliant on the camera's resolution and the operator's skill. Optical distortion caused by curved channel walls or varying refractive index may also cause significant measurement inaccuracy. Particularly, in circular microchannels with extremely small radii, optical distortion is a major issue for flow imaging. In addition, this technique does not allow in-line assessment and to obtain results and hence, post processing of images is necessary.

In an effort to overcome some of the difficulties associated with measurements obtained using imaging techniques, Jakiela *et al.* (2011) employed a linear camera to only capture the channel's centreline. This method enables in-line measurements of droplet length and velocity by collecting necessary data and accelerating data processing by simply identifying the front and rear caps of the droplet. However, this method still requires a microscope with an integrated high-speed camera, which brings considerable uncertainty to the measurements.

In addition to optical methods, there are also other methods based on changes in a fluid's electrical characteristics caused by the presence of a second phase. Differences in the electrical resistances of the phases involved, means that resistive approaches are often utilized in cytometry to detect the presence of the droplets (Sun and Morgan 2010). However, this technique cannot provide an exact measurement of droplet length due to the low sensitivity of the technique. A capacitive measurement technique was also developed by Niu *et al.* (2007), which detects the passing of a droplet and determines its velocity by analysing the corresponding signal. The technique involves using two electrodes placed in close proximity to each other, such that the droplet passing between them changes the capacitance of the system. The signal produced by the capacitive measurement technique is a voltage signal that corresponds to the capacitance changes. The signal is then processed to determine the velocity of the droplet passing through the electrodes. This can be done using various signal processing techniques such as differentiation and integration, depending on the specific characteristics of the signal. However, this approach gives less accurate length measurements as a result of signal convolution. Capacitive sensors are generally used in microelectromechanical systems (MEMS), commonly to sense pressure and acceleration (Eaton and Smith 1997; Berggren *et al.* 2001). It is crucial to keep in mind that each of these electrical approaches requires intricate microfabrication and electrode implantation within the channel.

It is also possible to explore the instantaneous flow conditions by means of tracer-based measuring techniques such as Particle Image Velocimetry (PIV) or light-induced fluorescence (LIF). Unfortunately, adding tracers inevitably contaminates the fluidic system, which results in disrupted local hydrodynamics and triggered chemical reactions. Additionally, this technique requires bulky and expensive equipment to perform the measurements and laborious procedures to extract the data.

Thus, researchers have found it challenging to develop precise and suitable apparatuses for in-line assessment and manipulation of flow characteristics in microscale two-phase flows. Research in this area is motivated by the need to establish ultrasensitive detectors that can extract the most information about the flow characteristics and enable instant modifications to the flow.

In this regard, the current study proposes a novel measurement technique for investigating flow properties in both liquid-liquid and liquid-gas slug flow regimes. Regardless of channel shape, this non-intrusive approach allows in-line measurements of both carrier and dispersed phase length and velocity with excellent precision. This measurement methodology will aid in the determination and analysis of two-phase flow configurations in transparent microchannels, allowing for a better comprehension of the experimental data.

3.2. Experimentation

The main goals of the experiments are to measure the droplet length and velocity in a two-phase flow regime. This requires an experimental test bed to create and move a slug train within a tubing of precisely defined dimensions, and the ability of the setup to automatically detect a phase shift. The phase detection system should be capable of detecting a phase shift between the slugs in a slug train. This has been done using an optical sensor to detect changes in the optical density or refractive index of the fluid. As the slug train moves through the tubing, the phase detection system monitors for any phase shifts between the slugs. If a phase shift is detected, the system automatically records the time and location of the shift. The following outlines the detailed procedures of the experimentation.

3.2.1. Droplet Generation and Transport

Figure 3.1 illustrates a schematic of the automated experimental setup employed in the current study. In microfluidic applications, syringe pumps are the preferred option as they

offer sufficiently stable and reliable volumetric flow rates. In the current experiment, a Harvard Pico Plus Elite syringe pump, with an accuracy of $\pm 0.35\%$, was used to pump the fluid through the tubing. This programmable pump provides improved flow performance with extreme precision and a smooth flow range of 0.54 pl/min to 11.70 ml/min. Glass syringes with a high accuracy in nominal diameter were used to minimize any uncertainty due to deformation of the barrel and piston during the experiments. Therefore, the pump setup can provide a precise flow rate.

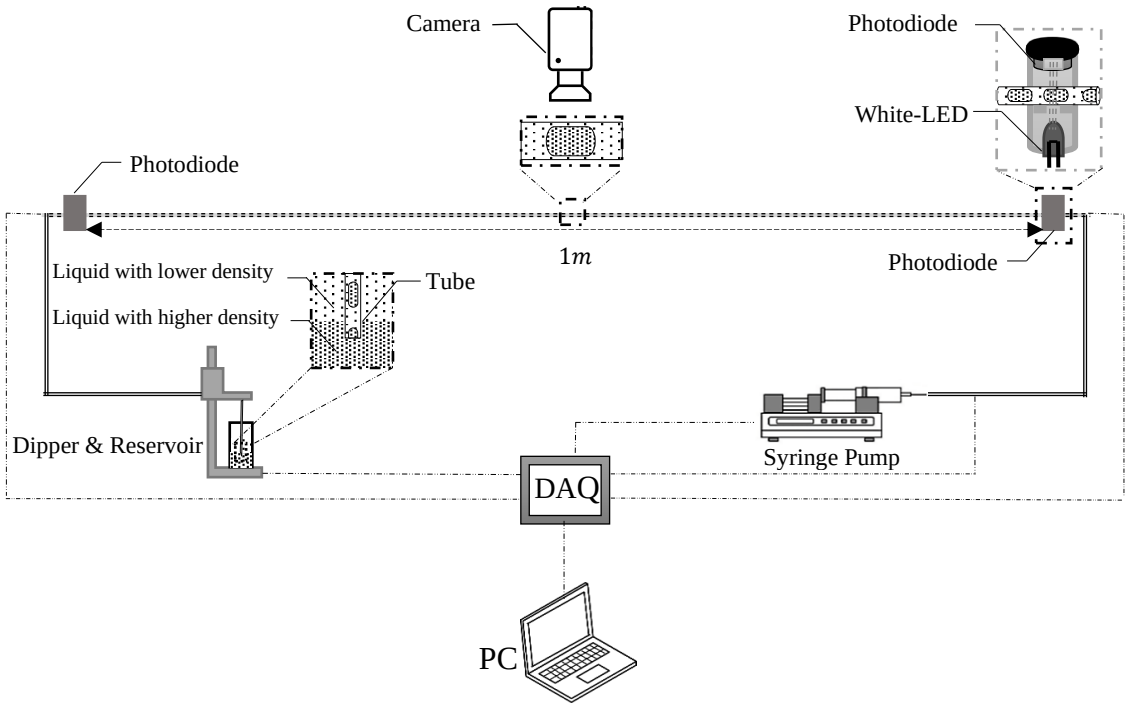

Figure 3.1. Experimental configuration used for slug length and velocity measurements.

Before generating droplets, the FEP (Fluorinated Ethylene Propylene) tubing was first primed with the carrier liquid. Then, with the syringe pump at one end of the tube in withdraw mode, both liquids were drawn into the tube while simultaneously vertically sliding a custom designed traverse/dipping stage into a reservoir containing both immiscible fluids (see Appendix F for more details). As the tubing's tip enters the target liquid, the pump draws in a desired amount of that liquid. This requires knowledge of which phase is denser and the precise location of the interface between the fluids to be input to the traverse programme. The tip of the tubing has been cut at a 45-degree angle to improve accuracy and prevent the introduction of air bubbles into the system. To prevent drawing the incorrect fluid, the dipping height must be adjusted according to interface position within the reservoir. By means of G-Code (NC-Code) programming, the traverse system

and syringe pump can generate droplets with different lengths. A reservoir with a relatively large volume of 200 millilitres is used to minimize the effects of interface height changes during experiments. With a larger volume of liquid in the reservoir, the fluctuations in the interface height between phases are reduced and more consistent slug flow patterns are achieved. This technique enables a high precision and a significant high degree of freedom in terms of the droplet and the carrier phase lengths.

3.2.2. Tubing Diameter Measurement

Droplets were generated in FEP Teflon tubes (Cole Parmer^{TM}) with the nominal inner diameter of $0.8\ mm$ and the total length of $5.70\ m$. Knowing the exact cross-sectional area of the channel with the least amount of uncertainty is essential when working with microfluidics systems. In experimental trials, the nominal sizes of the channels, as given by the manufacturers, are typically considered in calculations. However, there is often a mismatch between the nominal and actual dimensions.

PIV is a commonly used measurement technique in the literature to determine the actual channel's cross-sectional area. In this measurement technique, the analytical solution for the velocity profile across the tube, given by the Navier-Stokes equations for a laminar flow regime, can be employed to determine the tube diameter at specific locations. To precisely determine the bi-dimensional velocity profile in different planes in the microchannel, the actual shape of the section must first be determined. Therefore, microscopic techniques such as SEM are usually needed to accurately define the cross-section's shape. Typically, the cross-section's shape does not match the manufacturer's data sheet exactly. For example, according to the data sheet provided by a manufacturer, the channel's cross-section is a perfect square, when it actually may be somewhat trapezoidal and the angles may not be exactly right-angles. This can significantly affect the accuracy of the velocity measurements determined by means of PIV. Therefore, it is relatively challenging to precisely determine the cross-sectional area of a microchannel using PIV/µPIV. Moreover, variations in dimensions along the channel length are not included in this measurement technique as it is a local velocity measurement at a specific distance along the tubing length. A method that provides an averaged value of the diameter is more desirable.

Measuring the pressure drop along a specific length of the channel is another method for determining the cross-sectional area of a microchannel. In the case of circular cross-

sections, the capillary diameter can be determined by measuring the pressure drop of a laminar flow along the tubing and applying Hagen-Poiseuille's equation ($D^4 = 128\mu LQ/\pi\Delta P$) (Walsh *et al.* 2009). This method delivers the averaged value of a tubing diameter and is noticeably simpler than using PIV. However, its accuracy can be considerably impacted by uncertainties imposed by the pressure sensor and the fluid viscosity. Based on this technique, an uncertainty of ∽1.5% is determined for tubing diameter by considering uncertainty of 2% for viscosity, 1 mm for length, 0.35% for flow rate (based on the pump specifications) and 5% for pressure drop. Moreover, there are only a few precise solutions available to calculate pressure loss for non-circular cross-sectional areas, and approximations or empirical models are often used to estimate the pressure loss in non-circular conduits.

To avoid the aforementioned challenges, this study offers a new technique to accurately measure the averaged diameter of the tubing. The inner diameter of the tubing is obtained by filling a certain length of the tube at a certain flow rate (Q) and measuring the time (Δt) it takes for the phase to shift from air to liquid. Two photodiode sensors, one meter apart, were used to determine the exact phase changing time. The following subsection outlines the detailed procedures to precisely detect the phase change. Knowing the tube length (l), phase shifting time (Δt) and the filling flow rate (Q), the tube diameter (D) can be calculated by the following equation:

$$D = 2\sqrt{\frac{Q\Delta t}{\pi l}} \tag{3.1}$$

In the current study, the actual diameter was measured to be 6% less than nominal diameter given by the manufacturer. Considering length, flow rate, and time as the independent variables, an uncertainty value of 0.2% is determined for the tubing diameter. Maximum inaccuracy of 1 mm for tube length, 0.35% for flow rate, and $2.5 \times 10^{-4} s$ for time were considered to determine the uncertainty values. It is important in this procedure to use a tube that has not been used before as any trace of liquid within the tube results in a smaller diameter than the actual value. With any cross-sectional geometry, this method can be used to precisely measure the average channel area.

3.2.3. Droplet Detection

In this study, the automation of droplet recognition and related physical features such as droplet length and velocity are based on the difference in light transmission through a tube

caused by phase shifting in liquid-liquid flows. In this regard, a reliable light source that delivers a steady amount of light orthogonal to the length-axis of the tubing, as well as a sensor sensitive to light intensity, are required to identify the fluctuation in transmitted light caused by phase shifting. In the current investigation, standard white LEDs with a maximum voltage of 3.4 V and a maximum current of 50 mA were employed as a light source, and Burr-Brown photodiodes with an integrated amplifier, model OPT301M, were utilized to detect the transmitted light with the frequency of 4 kHz (detailed manufacturer's specifications of the equipment are provided in Appendix B). To keep system noise to a minimal level, the electrical cabling was grounded by a differential ground and shielded cables were used.

Figure 3.2 shows the assembly configuration of the light sensor. A holder was designed, and 3D printed from PLA to accurately locate the LED and photodiode at a specific axial location along the tube and orthogonal to the tube axis. The holder also shielded the photodiode from outside light.

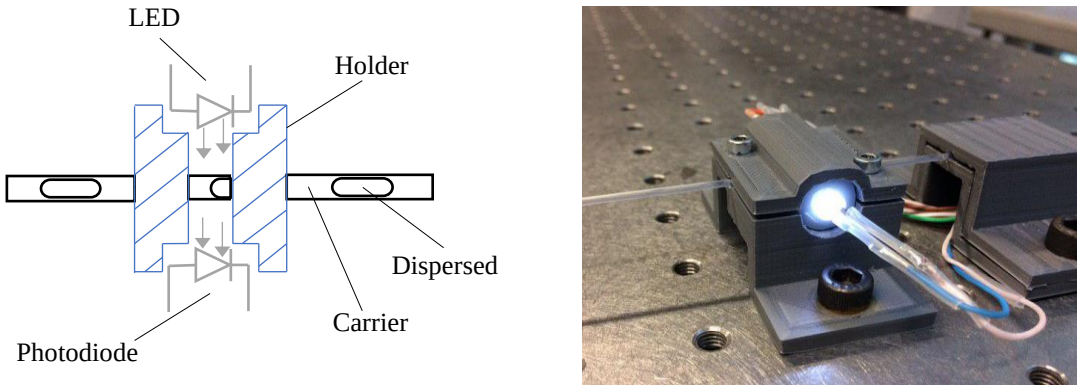

Figure 3.2. Configuration of the light sensor assembly.

Figure 3.3 illustrates the general wiring setup of the photodiodes. A symmetric power source that provides a $\pm 5\ V$ voltage range feeds the amplifier. Two different power supply units (PSU) were used to deliver a symmetric power supply. The positive output of PSU_1 is linked to the input_1 of the photodiode/amplifier, the negative exit of PSU_2 is connected to the input_3, and the short-circuit voltage level between both power supplies is connected to the input_8 of the photodiode which serves as a differential ground. Two 0.1 μF capacitors are placed between the positive/negative power supply and the grounding (see Figure 3.3) as recommended in the data sheet. According to this layout, the sensor's

outputs are pins 2, 4, and 5 with a resistor being placed between pins 4 and 5 to change the sensors' sensitivity. Also, in order to minimize the noise level, it's critical to ground the reader's housing with a differential ground.

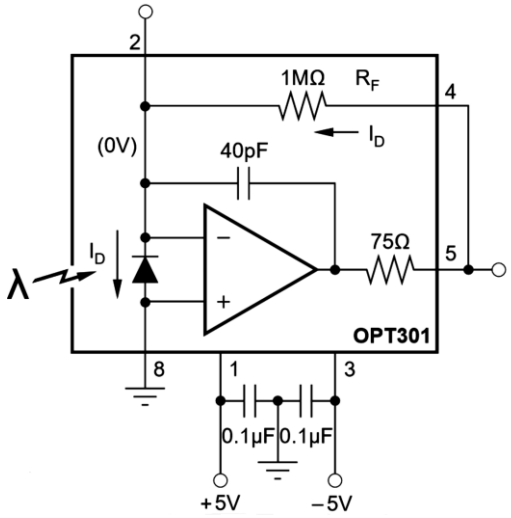

Figure 3.3. Schematic layout of the photodiode with an integrated amplifier.

The photodiode only determines the amount of light being received and delivers a specific voltage in accordance with the light intensity. Therefore, a procedure is required to extract the physical characteristics of the flow from the light sensor's output voltage. An example of an output signal from the photodiode is shown in Figure 3.4. In this case, water and AR20 are the dispersed and continuous phases respectively with results shown for two droplets.

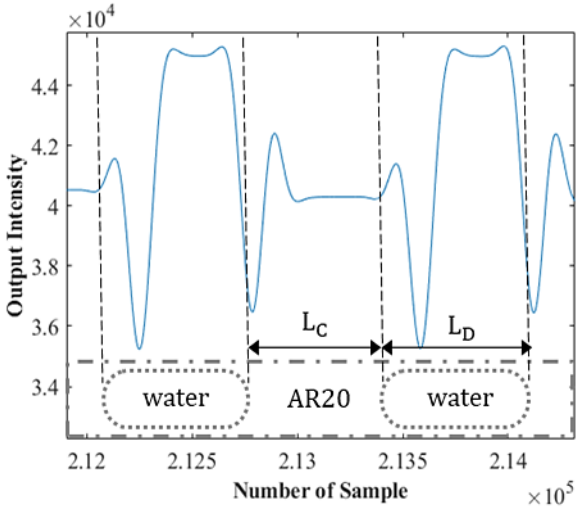

Figure 3.4. An example of recorded data for droplet velocity and length measurements from AR20-water.

The variation in light intensity recorded by the photodiode can be attributed to two factors. The first is due to a difference in the light transmission coefficient between the fluids. In liquid-liquid flows, due to the comparable refractive indices of the liquids, the change in light transmission is expected to be minimal. The second and more important effect is the dispersion caused by light refraction and reflection at the interface between the dispersed and carrier liquids. Although this technique can be used in both liquid-liquid and liquid-gas flows, the current study focuses on liquid-liquid flows to analyse the worst-case scenario in which there is a small difference in refractive index between the liquids. In this study, two different fluid combinations, AR20-water and HFE7500-AR20, were analysed within a circular capillary with an inner diameter of 0.75 mm. In AR20-water, AR20 with refractive index of 1.44 carries water droplets with refractive index of 1.33 while, in the second fluid combination, AR20 is dispersed within HFE7500 with refractive index of 1.29.

To better comprehend the signal post-processing and how droplet length was determined, Figure 3.5 displays a sample of the output signal from an individual water droplet as well as a schematic graph demonstrating the reflection effects.

(I) The droplet front cap has yet to be introduced, the light is perfectly aligned, and the signal intensity remains constant.

(II) Light reflection towards the photodiode, caused by the front cap, can explain the partial rise in light intensity. This light cannot travel through the light channel towards the photodiode in an undisturbed situation.

(III) As the droplet advances, the front cap reflects a significant quantity of light that would otherwise be transmitted to the photodiode. Additionally, due to the lower refractive index of water and cap curvature, a portion of the aligned-light is deflected towards the outside of the sensor window.

(IV) Beyond the caps, when the center of the droplet is aligned with the LED and sensor, there is a difference in the voltage output compared to the carrier fluid. The difference is due to the fluid's transparency, with water being more transparent than AR20.

(V) Light scattering caused by the rear cap results in a lesser amount of incoming light to the photodiode.

(VI) Similar to II, reflection effect of the rear cap on non-aligned light can explain the rise in light intensity.

(VII) Similar to (I), the droplet has passed the light window.

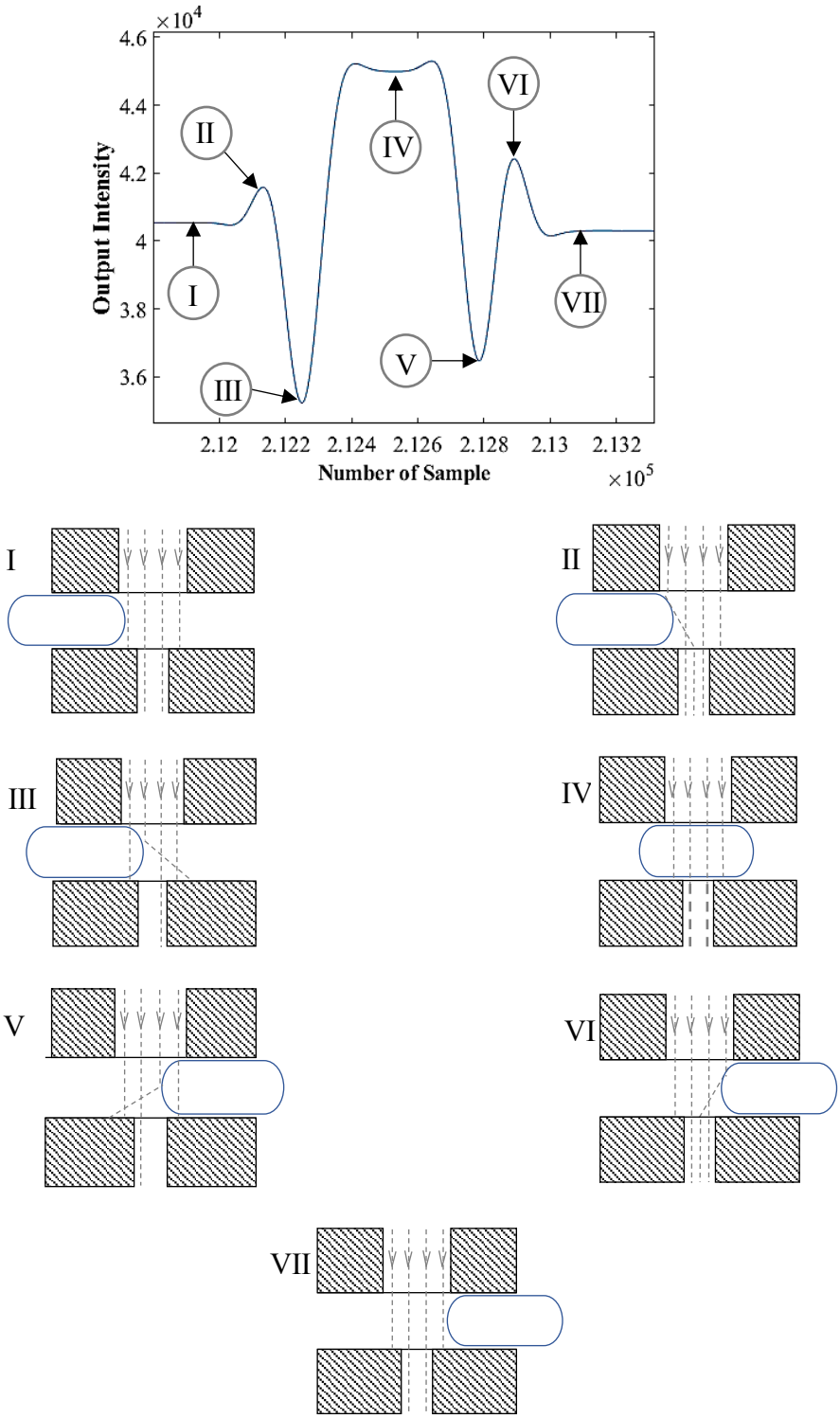

Figure 3.5. Signal intensity variations due to the light reflection and deflection effects caused by droplet caps. In this case, water droplet is dispersed in AR20.

The analogy to a sideward exposed hemispherical lens, which bundles or scatters light depending on the position of the light beam, explains why the cap surfaces have such a strong influence. Several images were taken using a high-speed camera of droplets with various lengths to confirm the accuracy of the signal processing (see Appendix G).

It is also worth noting that different fluid combinations, as well as changes in the holder, tubing diameter, and light intensity, result in slightly different recorded signals. Figure 3.6 presents a sample output signal from HFE7500-AR20. Unlike the signal from AR20-water (see Figure 3.3), when the center of the droplet is aligned with the LED and sensor, the voltage output is lower than the carrier fluid. This is due to the fluid's translucency, with HFE7500 being more translucent than AR20.

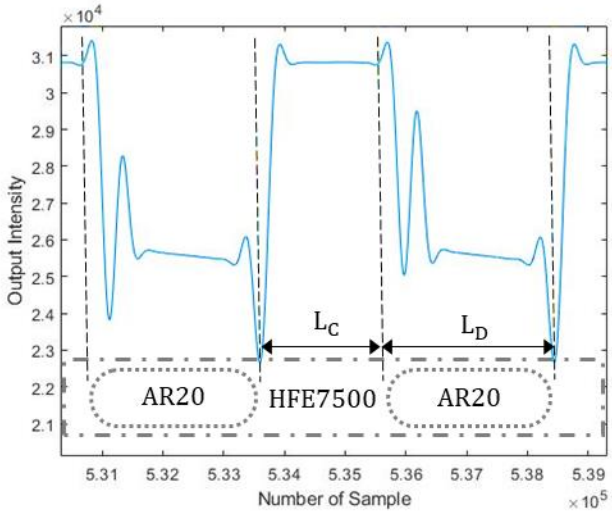

Figure 3.6. An example of recorded data for droplet velocity and length measurements from HFE7500-AR20.

Once the front and rear caps of the droplets have been detected, the velocity of each droplet can be simply determined by measuring the time it takes for the droplet to travel from one sensor to the next when placed at a specific distance (l) apart. The elapsed time (t) is determined based on the sample frequency (f) and number of recorded samples (n). In this study, two photodiodes were set at one meter apart and data was recorded at a frequency of 4 kHz. The length of a droplet (L_D) can be calculated using the droplet velocity (U_D) and the time it takes for the droplet to pass a single sensor. As a result, the length of the continuous phase (L_C) can be determined by knowing the times assigned to the back cap of one droplet and the front cap of the following droplet.

$$t = \frac{n}{f} \tag{3.2}$$

$$U_D = \frac{l}{t} \tag{3.3}$$

$$L_{D_i} = U_{D_i} \times (t_{r_i} - t_{f_i}) \tag{3.4}$$

$$L_{C_i} = U_{D_{i+1}} \times t_{f_{i+1}} - U_{D_i} \times t_{r_i} \tag{3.5}$$

t_r and t_f are the times assigned to rear and front caps respectively.

A data acquisition unit was set up to collect the data from two photodiodes and a custom MATLAB code was written for post-processing of the output signal (see Appendix E). This system setup allows for an in-line evaluation over the flow characteristics, as well as the storage of data on an SD memory card for subsequent analysis.

3.3. Validation of the Technique

Figure 3.7 presents results from length measurements for the dispersed (droplet) and carrier phases for a trial with 120 water droplets in AR20. In these graphs, the solid-lines present the mean value while the dashed-lines are deviations from the mean.

With the largest deviation from the average being 2% for the droplet (Figure 3.7(a)) and 4% for the carrier phase (Figure 3.7(b)), the results of the length measurements demonstrate an excellent consistency in both droplet and carrier lengths. Such low standard deviations show that the majority of the data is tightly packed around the mean value and the carrier and dispersed phases have consistent lengths. In comparison to the carrier phase, the droplet length data displays less deviations in the length measurements. During the droplet generation, the oil phase (AR20) with an almost equal and finite volume, separates the droplets from one another. As a droplet moves within a channel, depending on the flow hydrodynamics, the oil phase can travel from one side to the other side of the droplet through a thin film that separates the droplet from the capillary wall. The carrier phase length fluctuates throughout the experiment as a result of this phenomenon.

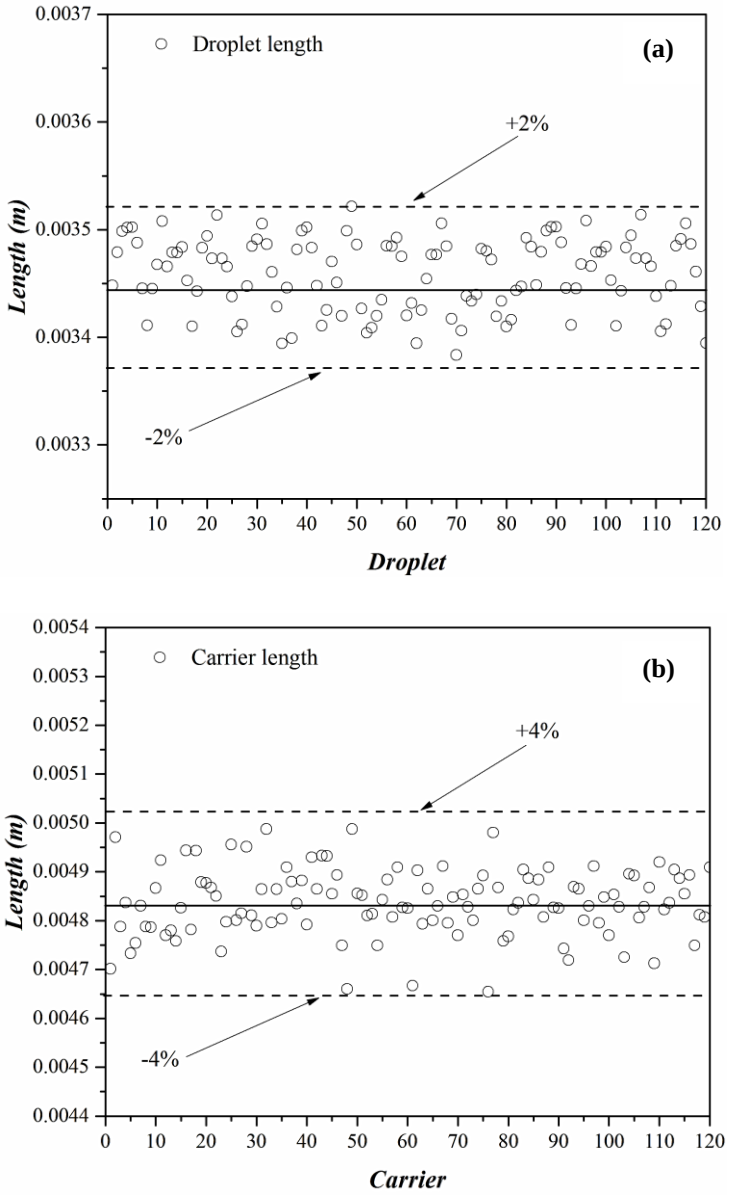

Figure 3.7. Data from measurements of (a) droplet length and (b) carrier phase length for 120 droplets of water dispersed within AR20.

Figure 3.8 presents results for the droplet and carrier phases of an 85-droplet train. In this example, AR20 droplets are dispersed in HFE7500. According to the data, the carrier and dispersed phases are consistent in length, and the majority of the data is tightly clustered around the mean value. Also, the carrier phase illustrates a lower maximum deviation (2.5%) in comparison to the experiment with AR20-water (4%).

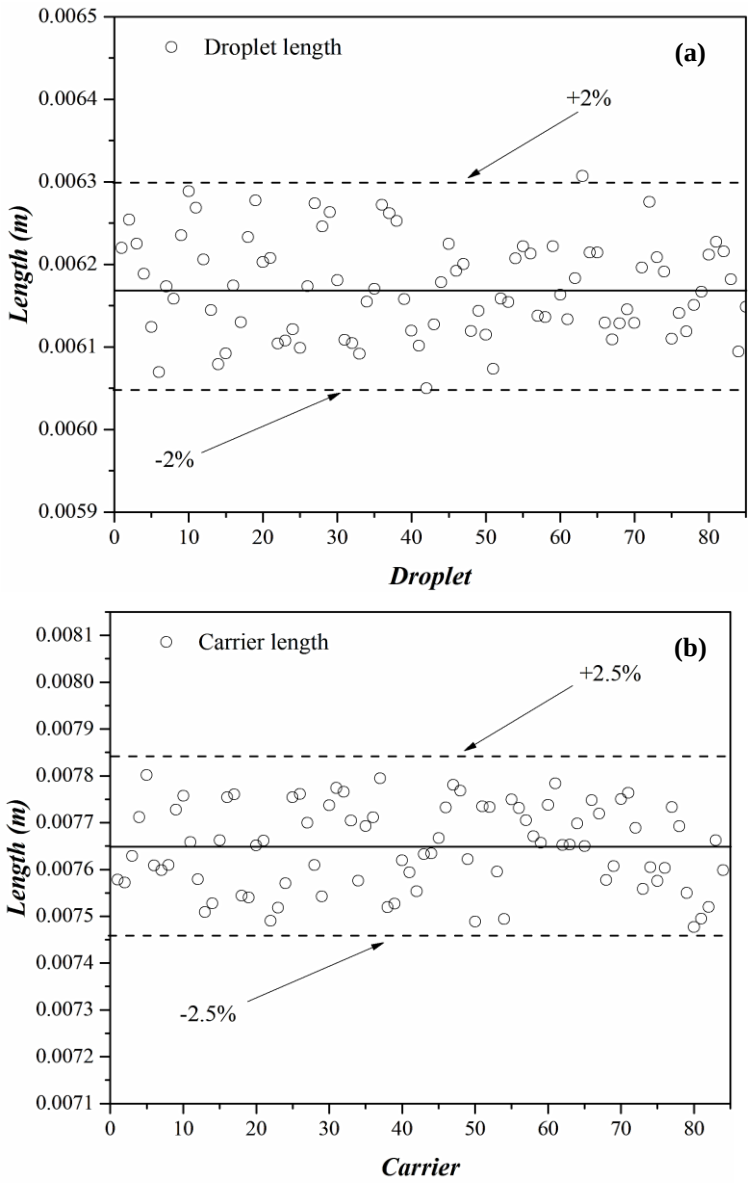

Figure 3.8. Data from measurements of (a) droplet length and (b) carrier phase length for 85 droplets of AR20 dispersed within HFE7500.

3.4. Conclusion

This study presents a novel measurement technique to determine droplet and carrier length and velocity for slug flows within macro and micro transparent channels. This non-intrusive method provides an in-line high-frequency platform for measuring flow characteristics of two-phase flows in channels of any cross-sectional geometric shape. The measurement technique can be used for rapid in-situ experimental modifications due to its real-time nature. The contrast in index of refraction that enables the phase detection, suggests that this detector might also serve as a preliminary step for probing the chemical

composition of droplets. Additionally, this methodology enables a cheap and reliable framework to determine the inner diameter of microchannels with a high precision.

Chapter 4

An Experimental Study on the Mobility of Droplets in Liquid-Liquid Taylor Flows within Circular Capillaries

An Experimental Study on the Mobility of Droplets in Liquid-Liquid Taylor Flows within Circular Capillaries

Chapter on Published Journal Article:

International Journal of Multiphase Flow[1]

Date: September 2022

Seyyed Saeed Shojaee Zadeh*[a], Vanessa Egan[b], Pat Walsh[c]

*****Corresponding Author

a CONNECT Centre, Stokes Laboratories, Bernal Institute, School of Engineering, University of Limerick, Ireland, V94T9PX. E-Mail: saeed.zadeh@ul.ie, Tel:+353873818619, ORCID: 0000-0003-1359-7232

b CONNECT Centre, Stokes Laboratories, Bernal Institute, School of Engineering, University of Limerick, Ireland, V94T9PX. E-Mail: vanessa.egan@ul.ie, ORCID: 0000-0001-8828-6303

c Stokes Laboratories, Bernal Institute, School of Engineering, University of Limerick, Ireland, V94T9PX. E-Mail: pat.walsh@ul.ie

URL: https://doi.org/10.1016/j.ijmultiphaseflow.2022.104259

Abstract

Further development of microfluidics devices that rely on liquid-liquid droplet flows, requires a thorough understanding of the parameters influencing droplet velocity. This study provides greater insights into this subject through an analysis of parameters effecting droplet mobility in such flows. A novel, fully automated experimental setup was designed to accurately measure droplet velocity and length. Measurements were performed over a wide range of Capillary number (2×10^{-4} *to* 3.7×10^{-2}*), Bond number (*0.05 *to* 3.2*) and carrier to dispersed viscosity ratio (*0.059 *to* 23.2*) while also varying droplet length. Five different fluid combinations were examined within circular capillaries with inlet diameters ranging from* 555 *μm to* 1.70 *mm. Results reveal a complex relationship between droplet velocity and droplet length, viscosity ratio and Bond number. In all cases, as droplet length exceeds a threshold value, droplet velocity becomes independent of length and is shown to scale with ~* $Ca^{0.5}$*. As the droplet length falls below the threshold, the droplet velocity faces a changeover zone in which the velocity initially declines and then rises with further decrease in the length. For shorter droplets, higher Bond numbers cause the droplet phase to travel asymmetrically with respect to the channel centre line which substantially impacts the mobility of these droplets. Finally, a new expression has been developed to estimate the velocity of elongated droplets.*

Keywords: *microfluidics, droplet mobility, droplet length, viscosity ratio, Bond number*

[1] See Appendix A for publication reference.

4.1. Introduction

Droplet microfluidics is a cutting-edge small-volume liquid manipulation for lab-on-a-chip that has seen rapid growth in recent decades. This technology has been applied in several chemical, mechanical and biomedical applications in order to achieve higher mixing and mass flow rates and to regulate and manipulate fluids on micro-scale devices. As immiscible fluids move within the channel, internal circulations within the droplet and carrier phases result in enhanced mixing and heat and mass transfer compared to single phase flows (Elamvaluthi and Srinivas 1984; Wegmann and Rudolf von Rohr 2006; Malsch *et al.* 2008; Talimi *et al.* 2012). In chemical processing, micro-fluidic devices have benefitted process intensifications by replacing the conventional large channel with micro-scale sizes. A high surface to volume ratio in such devices brings numerous advantages such as high efficiency, less wastage of materials, clear and cheaper processes etc. (Khan *et al.* 2017). When compared to standard single-phase flows in thermal management, liquid-liquid flows have shown increased heat transfer rates of up to 700% (Mac Giolla Eain *et al.* 2015). Synthesis of nano materials, DNA analysis, nitration reactions are all examples of chemical and biological applications that take advantage of microreactor technologies (Burns *et al.* 1998; Taly *et al.* 2007; Fidalgo *et al.* 2008). Microreactors are shown to have an exceptionally narrow residence time distribution, which causes great reduction in the generation of by-products in sequential reactions (Kreutzer *et al.* 2005a; Waelchli and von Rohr 2006).

In most applications benefitting from segmented flows, the coalescence of droplets is an undesirable phenomenon which reduces system efficiency (Méhault *et al.* 2021). This phenomenon happens due to the dissimilarity in the droplet velocities (U_D). As droplets in a chain move at different velocities than their neighbours, droplet-to-droplet distances become inconsistent, resulting in the coalescence of adjoining droplets. In applications such as protein crystallization (Zheng *et al.* 2003), synthesis of microparticle (Xu *et al.* 2005) and reaction screening (Hatakeyama *et al.* 2006), the coalescence of adjoining droplets might induce reagent contamination, change in droplet size, and make it difficult to spot an individual droplet among a chain of droplets (Chen *et al.* 2007). On the other hand, managed droplet coalescence has emerged as a fundamental microfluidic technique in some applications. For example, in order to have a satisfactory mixing effect, two distinct droplets must be fused together in the process of micro and nano particle manufacturing

(Zhang *et al.* 2008; Baroud *et al.* 2010; Xiao and Zhang 2011; Jiu-Sheng and Jiang 2012; Deng *et al.* 2015). Also, droplet-merging techniques offer a lot of potential in biological applications such as cell transplantation for the treatment of disorders including diabetes and hemophilia (Shintaku *et al.* 2007).

Thus, preventing or regulating droplet coalescence in a microfluidic system requires a comprehensive understanding of the parameters that determine droplet velocity. It has been shown by various studies that several parameters affect droplet mobility in liquid-liquid flows including channel geometry, droplet size, presence or absence of surfactants, flow velocity, liquid viscosities and interfacial tension (Jakiela *et al.* 2011). As a result, developing a model to predict droplet velocity has become a serious challenge among researchers. In this regard, several attempts have been carried out over the last few decades to characterize the dispersed phase in two-phase flows within milli and microscale channels. Most existing studies were aimed at liquid-gas flows (Bretherton 1961; Schwartz *et al.* 1986; Abiev 2017; Zhang *et al.* 2017) with only a few focusing on liquid-liquid flows (Hodges *et al.* 2004; Vanapalli *et al.* 2009; Jakiela *et al.* 2011). As such, the physical behaviour of liquid-liquid flows is still unclear and not fully understood. In addition, most research on liquid-liquid flows only use low-viscous fluids as the dispersed phase, with limited studies reporting on a high-viscous droplet being carried by a fluid with a low viscosity. A low-viscous liquid, as the carrier phase, results in a lower energy consumption and reduced overall cost of the operation due to the smaller pressure drop throughout the channel (Mac Giolla Eain *et al.* 2015; Mukhaimer *et al.* 2015). Therefore, further investigation is necessary to pave the path for using low-viscous liquids as carrier fluids rather than high-viscous ones.

In liquid-gas flows, Fairbrother and Stubbs (1935) made the first attempt to characterize such flows and observed that the dispersed bubble moves faster than the mean flow due to the existence of a liquid film at the capillary wall. Their findings revealed that the relative drift velocity (bubble velocity/mean velocity) is proportional to $Ca^{0.5}$ with the Capillary number being the only effective parameter. Approaching the subject theoretically, Bretherton (1961) was the first to develop a fundamental correlation predicting the dispersed phase velocity. Based on his findings, the bubble velocity exceeds the mean flow velocity by an amount of $W \simeq 1.29(3Ca^{2/3})$ in absence of any gravitational effects. Experiments with liquid-gas flows for Capillary numbers of less than 10^{-3} supported these findings with less than 10% error. Afterwards, Schwartz *et al.*(1986)

endorsed Bretherton's model for high flow velocities and long bubbles, but at low velocities the model underpredicted the bubble velocity.

In liquid-liquid flows, Hodges *et al.*(2004) made the first theoretical effort to investigate a viscous droplet within a circular capillary. Based on their findings, the droplet motion can be determined by means of three independent parameters; droplet size, viscosity ratio between phases and the Capillary number. In their study, gravity effects were considered to be negligible. Due to the importance of the subject, more attempts to empirically explore droplet mobility have been reported in recent years. Despite the increased attention and effort, there is yet no reliable and widely acknowledged model in the literature to estimate droplet mobility within micro-scale channels. Complexity of the problem and precision of the instruments have brought a significant level of discrepancies into the literature. For instance, in studies by Vanapalli *et al.*(2009) and Labrot *et al.*(2009), droplet mobility (u_d/u_m) is determined to be 1.28 and 1.6 respectively, and the droplet length and viscosity of liquids are found to have no effect on the droplet mobility. Vanapalli *et al.*(2009) performed their experiments in a micro-scale rectangular channel ($120\ \mu m \times 200\ \mu m$) while Capillary number, droplet to carrier viscosity ratio and droplet length to channel width ranges were $10^{-3}-10^{-2}$, $0.03-0.88$ and $1.5-7.2$ respectively. Labrot *et al.*(2009) examined chains of droplets within a rectangular channel ($300\ \mu m \times 500\ \mu m$) for $10^{-3} \leq Ca \leq 4 \times 10^{-3}$ and $0.014 \lesssim \mu_C/\mu_D \lesssim 20$. In a recent study by Abdollahi *et al.* (2020b), droplet velocity was found to be 10% higher than the mean velocity for the range of $0.0005 \leq Ca \leq 0.02$ regardless of the droplet volume. This study focused on flows in square channels with hydraulic diameters of 1 mm and 2 mm. In contrast, viscosity ratio and droplet size are demonstrated to have significant influences on droplet velocity in research by Jin *et al.*(2010) and Jakiela *et al.*(2011). Jakiela *et al.*(2011) studied the effect of droplet size and viscosity on droplet velocity by generating individual droplets within a square micro-channel (with the width of $360\ \mu m$). In their experiments, droplet to carrier viscosity ratio ranges from 0.3 to 33 and Capillary number spans three order of magnitude ($10^{-4}-10^{-1}$). Dependency of droplet velocity on Capillary number is shown to be very strong for $\mu_C/\mu_D < 1$ however, for $\mu_C/\mu_D \geq 1$ and $\mu_C/\mu_D \ll 1$ is less important. Jin *et al.*(2010) proposed a spontaneously synchronized droplet-merging technique, which enables two droplets with different sizes or viscosities to merge in a straight rectangular microchannel. In their experiments, PEG-DA (polyethylene glycol diacrylate Mn 258) was used as the carrier phase within rectangular

microchannels, with and without expansion of the cross-section, while water and mixture of water-glycerol were the dispersed phases. According to this research, the low viscosity droplet flows faster than the high viscosity droplet.

After evaluating relevant studies in the literature, four issues have been identified: (1) Most research aimed at droplet velocity has been performed within channels with a rectangular cross-sectional area with only a few studies carried out with circular capillaries. The hydrodynamics of a droplet in a rectangular channel differ from those in a cylindrical channel with an axial symmetry. In a cylindrical channel, drops are spherical or plug-like, depending on droplet volume. However, in a rectangular channel, the droplet forms a spherical shape until its diameter is smaller than the channel height. As the droplet becomes larger, the channel walls reshape the droplet to a pancake-like shape and further increasing droplet size results in a plug-like shape (Ahn *et al.* 2006). It has been shown by several studies that droplet size and shape can greatly affect the flow topology inside and outside of the droplet (Roberts *et al.* 2014; Zhao *et al.* 2015). The presence or lack of well-formed internal circulations has been found to have a significant impact on droplet velocity (Jakiela *et al.* 2012). In a study by Helmers *et al*.(2022), the droplet's relative velocity was reported to negatively correlate with the evoked topological change in a rectangular channel. Furthermore, due to fluid leakage at the corners of rectangular channels, droplet velocity in such channels is expected to differ from circular capillaries. (2) In previous experimental studies, droplet velocity is measured by analysing high quality images captured by means of high-speed cameras. These techniques usually necessitate complicated and cumbersome apparatuses, such as microscopes with integrated high-speed cameras followed by image post-processing, limiting manoeuvrability and offering only short-term assessments (Robert de Saint Vincent *et al.* 2012). In addition, the accuracy of measurements using such techniques is greatly restricted to the camera’s resolution and the operator' skill. In these cases, optical distortion induced by curved channel walls or a different refractive index can lead to a significant level of measurement uncertainty. (3) The nominal sizes of the channels, as given by the manufacturers, are assumed in most experiments, but taking this approach may lead to incorrect results. In such experiments, the drift velocity of the dispersed phase is determined by knowing the flow rate of the continuous liquid and the respective cross-section area. As a result, it is critical to determine the precise area of the channel cross-section with the least level of uncertainty. For example, 2% inaccuracy in capillary diameter measurement results in $\simeq$ 4% error in flow velocity measurements. This

may account for some of the discrepancies in empirical results observed in the literature. (4) Most investigations have neglected the impact of buoyancy forces on droplet motion without referencing the Bond number values (ratio of the buoyancy force to the surface tension force). Although gravity effects are less important in liquid-liquid two-phase flows due to the comparable density of both phases, they can still have a considerable impact depending on channel dimensions and interfacial tension between phases. This is especially important when working with dense fluids such as fluorocarbons (e.g. FC40) which are commonly used in biotechnology applications. The symmetrical shape of the droplet is shown to be significantly distorted by gravitational forces at high levels of Bond number and causes non-uniform film thickness along the cross-section (Bretherton 1961; Suresh and Grotberg 2005). The majority of previous studies ignore gravitational effects for $Bo < 1$, however in a study by Jovanović *et al.*(2011) the buoyancy force was demonstrated to affect the flow hydrodynamics even at $Bo \simeq 0.06$.

In this regard, a new experimental technique is proposed and employed in the current study to determine droplet velocity in microchannels with high precision and reliability. This measurement procedure is completely automated, hence minimizing errors. The focus of the current study is an experimental investigation of droplet velocity in liquid-liquid flows with the objective of determining the effect of droplet size and viscosity ratio on droplet velocity within mini and micro capillaries. Measurements were obtained over a wide range of carrier to dispersed viscosity ratios (0.059 to 23.2), droplet length to capillary diameter ratios (0.7 to 16), Bond numbers (0.05 to 3.2) and flow velocities (7.3 to 53.6 mm/s). To achieve these ranges, five different flow combinations were utilized within circular capillaries with the inlet diameters ranges from $555\ \mu m$ to $1.70\ mm$. In three flow combinations, water formed the dispersed phase with HFE7500, FC40 and AR20 forming the carrier phases, and in other two combinations AR20 was the dispersed while HFE7500 and FC40 were the continues phases.

4.2. Experimentation

The experimental configuration used to measure slug length and velocity is shown in Figure 4.1. Droplets were generated in FEP Teflon tubes (Cole Parmer^{TM}) with the inner diameter varying from $555\ \mu m$ to $1.70\ mm$ and with a total tube length of $5.70\ m$. Prior to generating droplets, the tube was primed with the carrier liquid. Following this, both liquids

were then drawn into the tube using a Harvard Pico Plus Elite syringe pump, which was situated at one end of the tube, in withdraw mode and simultaneously vertically moving a custom-made traverse/dipping stage into a reservoir containing both immiscible fluids. The traverse system and syringe pump were controlled and synchronised by G-Code programming to generate individual droplets of various lengths (L_D). As the tip of the tubing enters the dispersed liquid, the pump draws in a desired volume of the liquid for any required droplet length. This requires knowledge of the carrier and dispersed liquid densities to identify which phase occupied the upper and lower portions of the reservoir, and the vertical location of the immiscible interface between phases was accounted for in the dipping program. Using this method, the droplet length can be controlled with a great degree of accuracy and freedom. 10 ml Hamilton glass syringes were used to minimize any uncertainty due to deformation of the barrel and piston during the experiments. In each experiment, only a single droplet was formed and then examined in the test section. The droplet velocity was measured as the average velocity between two optical sensors. These were placed midway along the tubing, 2.35 m away from the syringe and the inlet reservoir, as depicted in Figure 4.1. This ensured that measurements were performed under fully developed flow conditions and that the process of droplet creation did not affect the measurements. These sensors were used for measurement of droplet length (L_D) and velocity (U_D).

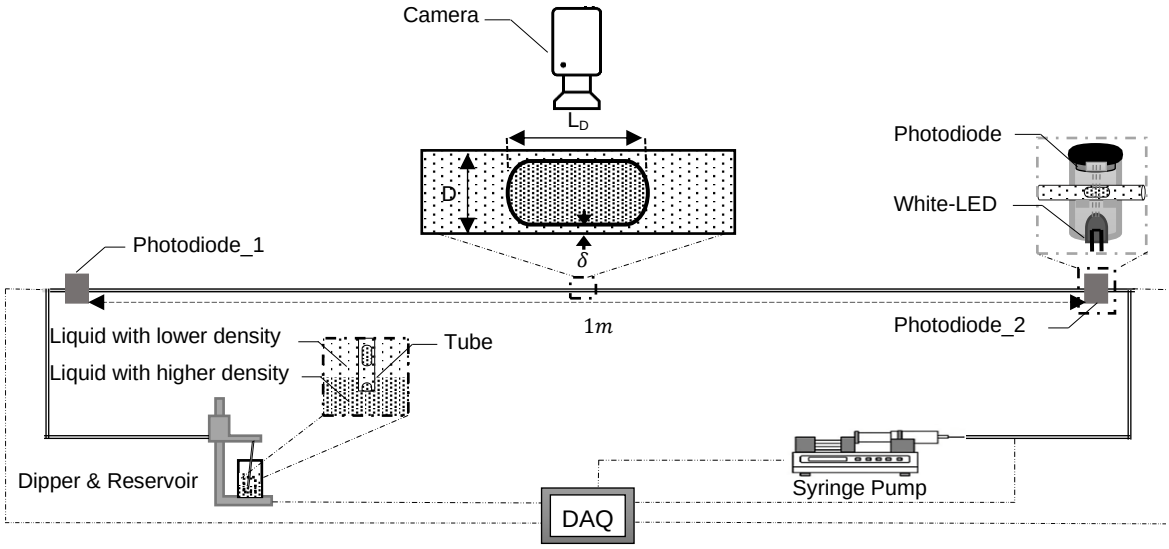

Figure 4.1. Experimental configuration for droplet length and velocity measurements and illustration of two-phase flow structure highlighting capillary length (D), droplet length (L_D) and film thickness (δ).

Figure 4.2(a) provides a detailed schematic of the optical sensor build-up. Each light sensor configuration consists of an LED, a photodiode, and a holder. In this experiment, white LEDs with a maximum voltage of 3.4 V and current of 50 mA were used as a light source to have constant and reliable level of light emission. To detect light transmission variations, Burr-Brown photodiodes with integrated amplifiers (OPT301M) were employed. Their output voltage, which is proportional to input light intensity, was recorded at a frequency of 4 kHz using a data acquisition system. A plastic holder was manufactured to keep both the LED and photodiode in a desired location and orthogonal to the tube axis. Also, the holder places the LED and photodiode 2 cm apart to ensure a parallel light beam and alignment of the light path towards the photodiode. The light path consisted of a cylindrical hole, perpendicular to the tube axis, with a measured diameter (ϕ_L) of 500 μm ± 50 μm.

As droplets pass each photodiode, the light intensity to the diode changes. Generally, changes in transmission from the light source to the photodiode are caused by two factors: the first is changing the light transmission index by switching from the carrier liquid to the droplet liquid. Because all the liquids utilized in this study were transparent, the effect of changing the transmission index due to the fluid properties was small. The second and more influential factor is light refraction and scattering at curved droplet interfaces between phases. This change in light intensity causes a change in the photodiode's voltage output, which is analyzed and used to measure droplet length, L_D, and velocity, U_D. Figure 4.2(b) shows a sample of recorded data from both sensors as a single droplet passed over them. Clearly, both sensors have a similar signal profile but differ in their intensity and noise level. The difference in output intensities may result from slight differences in their LED's current, which can be caused by differences in the current limiting resistor tolerances, and from slight differences in fabrication of the holders, which were 3D resin printed. Also, a longer cable to the data acquisition system or a greater electromagnetic field around the sensor was seen to contribute to the higher noise level observed in the signal from Sensor 2. To keep system noise to a minimum, the electrical hosing was grounded by a differential ground and shielded cables were used.

The output signal can be explained using the analogy of a sideward exposed hemispherical lens, which bundles or scatters light depending on the position of the light beam. A greater change in output signal correlates with a larger difference in refractive index between the carrier and dispersed phases. Figure 4.2(b) presents a signal from the

worst-case scenario of HFE7500 and water in which both liquids have similar refractive indices of 1.28 and 1.33 respectively.

As a droplet enters the light window (from left side in Figure 4.2(a)), the front cap reflects a significant quantity of light that would otherwise be transmitted to the photodiode. The time of this sharp reduction in sensor output intensity is assigned to the droplet's front cap entering the light path, t_1 in Figure 2(b). Following this, the signal stabilizes towards a relatively constant value while the droplet's center, which is approximately cylindrical in shape, traverses the light path. As the droplets rear cap approaches the sensor's light path, it exhibits similar behavior to the front cap by reducing the amount of incoming light to the photodiode and is deemed to have fully entered the light path when the output intensity is at a minimum. This time, t_2, is assigned to the rear cap having reached the left side of the sensor light path. Finally, the output signal returns to its initial value as the rear cap leaves the right side of the light path and the droplet has fully traversed the sensor, t_3.

Now that the front and rear cap characteristics are identified on the data signals, the droplet's velocity and length can be determined by utilizing the data recording frequency ($4\ kHz$) as a timescale. Droplet velocity (U_D) was determined from elapsed time for the leading cap of a droplet to travel from the entrance of Sensor 1 to the entrance of Sensor 2, which was placed $1\ m \pm 1\ mm$ downstream. Droplet length (L_D) was then determined by the product of droplet velocity and the elapsed time between the leading and trailing caps of a droplet passing the left side of either sensor, i.e. $t_2 - t_1$ in Figure 4.2(b). Alternatively, droplet length (L_D) plus the light path diameter (ϕ_L) can be determined by the product of droplet velocity and time elapsed between the leading and trailing caps entering and leaving either sensor's light path, i.e. $t_3 - t_1$ in Figure 4.2(b). In this case, the diameter of the light path needed to be subtracted to obtain an accurate value for droplet length. The latter of these methods was used to determine droplet length throughout this study since the central section of the data trace is not present when droplet length to tube diameter ratio is of order unity. However, both methods were evaluated for longer droplets and provided equivalent results.

It is further observable from Figure 4.2(b) that the droplet lengths obtainable from both optical sensors fall within a few recorded data points of each other so there is little discernible difference in droplet morphology along the 1 m test section. Additionally, since the signal-to-noise ratio of sensor 1 was greater than that of sensor 2, data from sensor 1 was used for droplet length measurement throughout. A custom MATLAB code was used

to post-process the output signal for calculation of droplet velocity and length using the described methodology (see Appendix E). Finally, several images of passing droplets were also recorded using a high-speed camera at the position shown in Figure 4.1 for droplets of various lengths. These images were also used to confirm the accuracy of the signal processing procedure outline here.

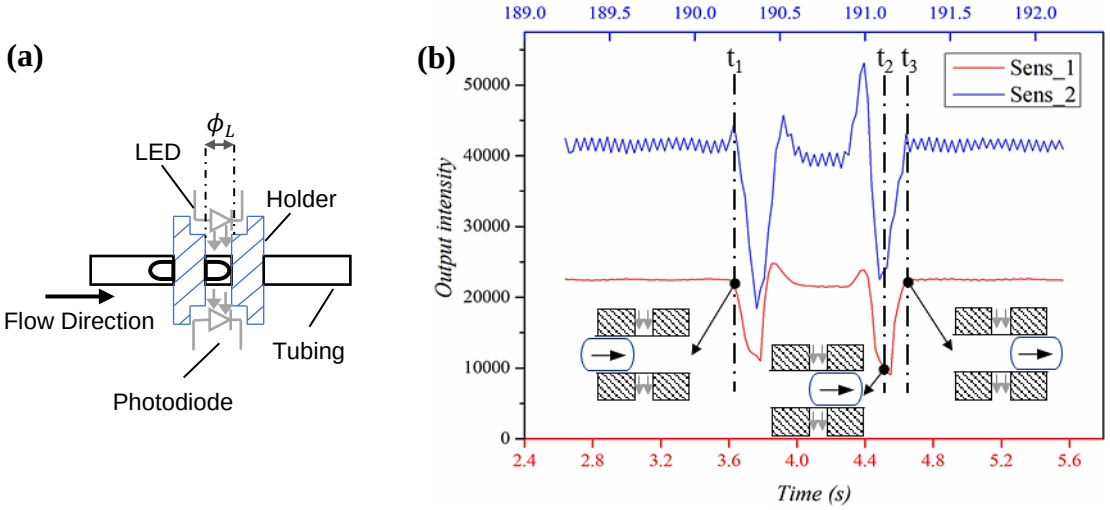

Figure 4.2. Light sensor configuration, (a) example of recorded data used for droplet velocity and length measurements (b) and images of a water droplet dispersed in HFE7500 within 1.6 mm inner diameter capillary.

In order to determine the exact inner diameter of the tubes two procedures were followed:

(1) By measuring weight of the liquid that fills a specified length of the tube and using the following equation:

$$D = 2\sqrt{\frac{m}{\pi L \rho}} \tag{4.1}$$

In this equation D, m, L and ρ are tube diameter, weight, length and the liquid density respectively.

(2) By filling the tube with a specific flow rate (Q) and measuring the time (t) takes for the phase to shift from air to liquid at two distinct positions along the tube. Two photodiode sensors located one meter apart were utilized to determine the exact phase changing time. The diameter can be calculated by following equation:

$$D = 2\sqrt{\frac{Qt}{\pi L}} \tag{4.2}$$

A CCD camera with maximum frame rate of 30 fps was employed for visualization purposes. Five different flow combinations were used in this study; in three flow combinations FC40, HFE7500 and AR20 were chosen as carrier fluids while water was the dispersed phase, and in two other flows AR20 was dispersed in FC40, HFE7500. The viscosity ratio (μ_C/μ_D) changes from 0.059 (HFE7500_AR20) to 23.2 (AR20_Water) to allow for an analysis of the effect of this parameter on the hydrodynamics of the flows. Measurements were obtained over a wide range of Reynolds (0.7 to 104), Capillary (2×10^{-4} to 3.7×10^{-2}), Bond (4×10^{-2} to 3.26) and Weber (3×10^{-3} to 1.56) numbers. Further details on the various liquids (fluid properties) and range in dimensionless groups are presented in Table 4.1.

The surface tension and interfacial tension between each fluid combination was measured using a KSV CAM 200, an optical contact angle measuring and contour analysis system. Prior to experimentation, all needles and syringes were rinsed and allowed to air dry using ethanol to remove any contaminations. In addition, all liquids were filtered twice to remove any trace impurities. Millex® sterile syringe filter was used which is ideal for sterilizing organic solvents, aqueous solutions or air/gas with a 0.45 μm pore size hydrophilic PVDF membrane. The detailed manufacturer specifications of the apparatus used throughout this study is provided in Appendix B.

Table 4.1. Thermophysical properties of the fluids and range of dimensionless groups investigated at **20** ℃.

Liquid	Density ($\boldsymbol{kg/m^3}$)	Viscosity ($\boldsymbol{kg/m.s}$)	Carrier/Dispersed	Interfacial Tension ($\boldsymbol{N/m}$)	Re	Ca	Viscosity Ratio (μ_C/μ_D)	We	Bo
Water	998	0.0009	**FC40/Water**	0.051	3.6 35.4	5.6×10^{-4} 4.2×10^{-3}	4.33	3×10^{-3} 1.2×10^{-1}	0.05 0.47
FC40	1854	0.0039	**HFE7500/Water**	0.049	9.4 104	2×10^{-4} 1.2×10^{-3}	1.37	3×10^{-3} 1.3×10^{-1}	0.04 0.31
HFE7500	1620	0.00124	**AR20/Water**	0.03	0.7 4.5	6.2×10^{-3} 3.7×10^{-2}	23.2	4.6×10^{-3} 1.7×10^{-1}	0.11
AR20	1142	0.0209	**FC40/AR20**	0.006	3.6 35.4	4.6×10^{-3} 3.5×10^{-2}	0.18	2.6×10^{-1} 1	0.34 3.26
			HFE7500/AR20	0.0019	9.4 50.7	6×10^{-3} 3.2×10^{-2}	0.06	6×10^{-2} 1.56	0.84 1.65

4.3. Results

To provide a better assessment of the data obtained, results are presented in terms of viscosity ratio of the tested fluids. Results from AR20_Water with a high carrier to droplet viscosity ratio ($\mu_C/\mu_D \gg 1$) are discussed first, followed by FC40_Water and HFE7500_Water experiments with comparatively moderate viscosity ratios ($\mu_C/\mu_D \approx 1$) and, finally, FC40_AR20 and HFE7500_AR20 with very low viscosity ratios ($\mu_C/\mu_D \ll 1$). Each set of experiments with a specific fluid combination was performed over four different flow velocities while droplet length ranged from a very small value ($L_D/D \approx 0.7$) up to the maximum possible values (up to $L_D/D \approx 18$) in each flow combination. During measurements, it was observed that from a certain length, droplets began to split and separate. The likelihood of this occurrence increases at higher droplet velocities. A first indication of the likelihood of droplet separation might be given by the Weber number, which links the inertia forces with the surfaces tension. In this study, Weber number spans from 3×10^{-3} to 1.56 and the minimal range of droplet length ratio ($0.8 \leq L_D/D \leq 7$) is represented by HFE7500_AR20 with the largest Weber number ranges ($0.06 \leq We \leq 1.56$).

In each run, only a single individual droplet was generated and was inspected at all four flow velocities. To ensure repeatability, each test was performed several times (at least three times) and the mean values of the data were used in analysis. The measurements indicate a high level of consistency in droplet length and velocity, with the largest deviation from the average value in each set of experiments being less than 1%.

4.3.1. High Viscosity Ratios ($\mu_C/\mu_D \gg 1$)

Results from AR20_Water with carrier (AR20) to dispersed (water) viscosity ratios (μ_C/μ_D) of 23.2 are presented in Figure 4.3. In this graph, the X-axis represents the droplet length (L_D) normalized by the capillary diameter (D) and the Y-axis is the ratio of droplet velocity (U_D) to mean flow velocity (U_{mean}). In these set of experiments, mean flow velocities and Capillary number ranges are $8.9 - 53.6\, mm/s$ and $6.2 \times 10^{-3} - 3.7 \times 10^{-2}$ respectively while droplet length ratio (L_D/D) spans from ~ 0.8 to ~ 13. The

experiments have been performed in a capillary with the inner diameter of $1.54\,mm$ and the Bond number is determined to be 0.11.

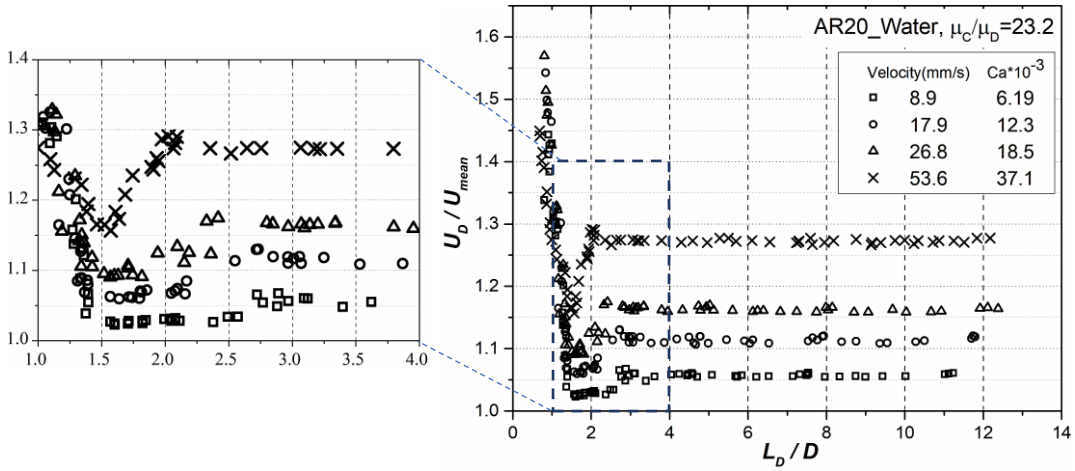

Figure 4.3. Variation in droplet velocity ratio with dimensionless droplet length for experiments with AR20_Water while $\mathrm{Bo} = 0.11$.

Figure 4.3 indicates that for longer droplets with $L_D/D \gtrsim 3$, droplet velocity becomes almost constant and no longer varies with droplet length. The commencement of this plateau zone shifts slightly from longer ($L_D/D \approx 3$) to shorter ($L_D/D \approx 2$) droplet length by increasing the flow velocity from 8.9 to $53.6\,mm/s$. Focusing on the plateau zones, the droplet velocity ratio increases from $\sim$1.05 to $\sim$1.27 by increasing the flow velocity and thus the Capillary number. The parabolic velocity profile for fully-developed laminar flow, implies the maximum flow velocity is twice that of the mean flow velocity at the capillary centre line. Thus, a neutrally buoyant droplet moves faster as its cross-sectional area shrinks and moves away from the capillary wall.

Figure 4.4 presents the images captured by a high-speed camera for AR20_Water experiments. These images show a water droplet dispersed in AR20 at four different velocities for a $1.54mm$ inner diameter capillary while maintaining a constant droplet volume. Clearly, the droplet becomes slimmer and a thicker film engulfs it as the flow velocity (U_m)/Capillary number (Ca) increases. According to several studies (Bretherton 1961; Aussillous and Quéré 2000; Howard and Walsh 2013; Mac Giolla Eain *et al.* 2013a), the magnitude of the film strongly depends on the Capillary number (Ca), with the film thickness increasing with Capillary number.

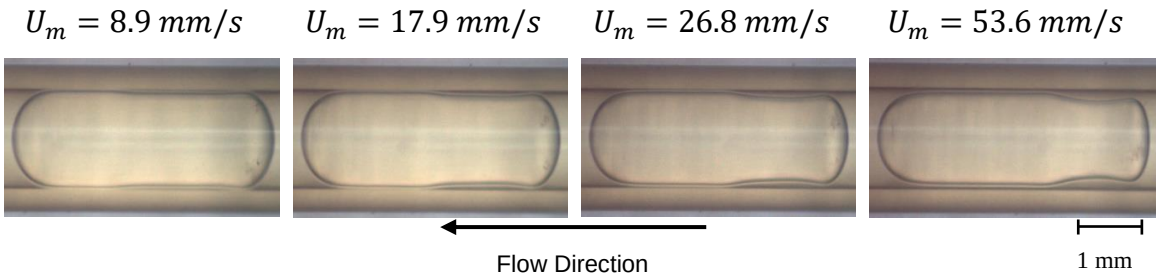

Figure 4.4. Images of water droplet dispersed in AR20 with a constant droplet volume at four different mean flow velocities. The capillary's inner diameter is 1.54 mm and the droplet length ratio (L_D/D) is measured to be 3.3 at the lowest flow velocity.

As the droplet length ratio reduces below the plateau zone threshold, the droplet velocity faces a crossover area in which the velocity initially decreases to a minimum before further increasing as droplet length reduces. This transition area narrows and deepens as the flow velocity increases. The magnified section, depicted in Figure 4.3, is provided in Appendix H, aiming to offer a better grasp of the underlying trends in this area. At the lowest flow velocity ($U_{mean} = 8.9\ mm/s$), the variations in L_D/D and U_D/U_{mean} in the crossover zone are $\sim$1.6 and $\sim$0.03 respectively, whereas these values are $\sim$1 and $\sim$0.13 at the highest flow velocity ($U_{mean} = 53.6\ mm/s$). Flow topology inside the droplet is believed to be responsible for the velocity reduction in this area where the absence of well-formed internal circulations has resulted in increased hydrodynamic resistance of the droplet (Jakiela *et al.* 2011; Li *et al.* 2020). The amplitude of this internal circulatory flow, as well as how strongly it is coupled with the outer flow, has been found to have a considerable impact on the droplet's hydrodynamic resistance (Vanapalli *et al.* 2009). Figure 4.5, taken from a numerical study by Kumari *et al*.(2013), illustrates the variations in the internal flow topology as the bubble length is changed.

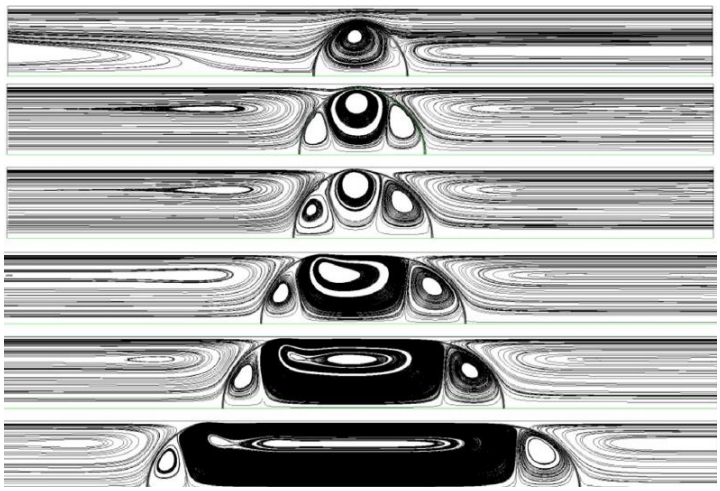

Figure 4.5. Effects of bubble length variation on internal flow topology adapted from a study by Kumari *et al*.(2018).

By further reduction in droplet length ($L_D/D \lesssim 1.2$), the plot shows a sharp increase in the velocity ratio. Figure 4.6 shows images from a small droplet of water with $L_D/D \sim 0.85$ dispersed in AR20 at different flow velocities. In this case, the droplet diameter is noticeably smaller than the capillary diameter and Taylor flow is said to no longer exist within the channel. Thus, the droplet travels significantly faster than a fully-confined elongated droplet (separated from the capillary wall by a thin film) by moving away from the capillary wall (where the flow velocity is almost zero) towards the capillary's centre where the flow velocity is maximum.

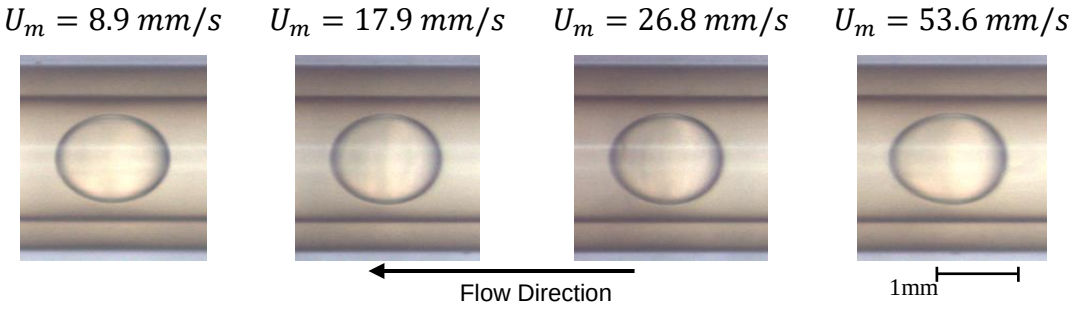

Figure 4.6. Images of water droplet dispersed in AR20 with a constant droplet volume at four different mean flow velocities. The capillary's inner diameter is 1.54 mm and the droplet length ratio (L_D/D) is measured to be 0.85 at the lowest flow velocity.

4.3.2. Medium Viscosity Ratios ($\mu_C/\mu_D \sim 1$)

Figure 4.7(a) and (b) present droplet velocity measurements for FC40_Water and HFE7500_Water respectively with moderate carrier to dispersed viscosity ratios. It can be clearly seen that results in both figures follow a very similar trend with a slight difference in the crossover zone's depth. In both figures, the plateau regions and the crossover zones begin at $L_D/D \sim 6$ and $L_D/D \sim 2$ respectively. In comparison to AR20_Water, FC40_Water and HFE7500_Water present longer but shallower crossover regions (see Appendix H). As previously noted, this transition region is thought to depend on the droplet's internal flow topology. It has been shown previously (Ma *et al.* 2014) that decreasing the viscosity ratio (μ_C/μ_D) suppresses the internal circulations within the dispersed phase. Also, a recent numerical study by Xu Chao *et al.*,(2021), showed that the mixing intensity at the front of the droplet reduces as the droplet viscosity increases. At the interface between the droplet and carrier fluid, the shear stresses are equal and given by the following equation.

$$\tau = \mu \frac{\partial u}{\partial n}\Big|_{n=Int} \Rightarrow \mu_D \frac{\partial u_D}{\partial n}\Big|_{n=Int} = \mu_C \frac{\partial u_C}{\partial n}\Big|_{n=Int} \Rightarrow \frac{\mu_C}{\mu_D} = \frac{(\frac{\partial u}{\partial n})_D}{(\frac{\partial u}{\partial n})_C}\Big|_{n=Int} \quad (4.3)$$

This implies that the dispersed phase is subjected to a lower shearing stress when the carrier phase has a lower viscosity. As a result, a droplet travelling in a low-viscous fluid is expected to have a more uniform internal flow pattern (weaker circulatory flows) due to a reduced shear stress on its surface. In cases with FC40_Water and HFE7500_Water with relatively lower viscosity ratios of 4.33 and 1.33 respectively, the velocity ratio variations associated with the flow topology are less than 2.5%; while in AR20_Water with a high viscosity ratio ($\mu_C/\mu_D = 23.2$), the stronger internal flow circulations of the droplet have a significant impact on the droplet velocity over a certain range of the drop length ($1 \lesssim L_D/D \lesssim 2$) and resulted in the velocity ratio changes up to $\sim 15\%$.

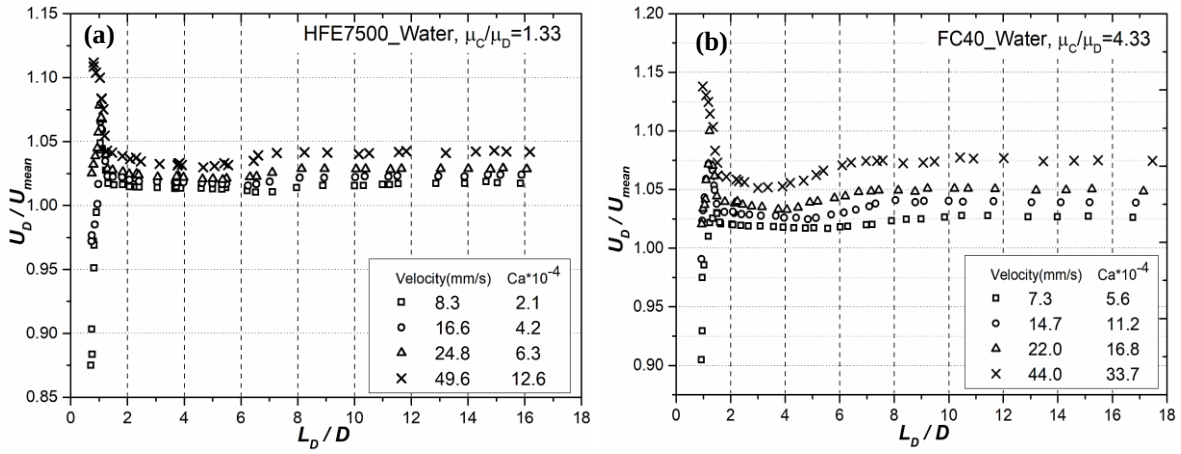

Figure 4.7. Variation in droplet velocity ratio with dimensionless droplet length for experiments with (a) HFE7500_Water, Bo = 0.47 and (b) FC40_Water, Bo = 0.3.

As the droplet length further reduces, the droplet velocity ratio exhibits two different behaviours depending on the flow velocity; at the highest flow velocity, a further reduction in droplet length causes the droplet velocity to increase considerably, similar to AR20_Water. As previously discussed, this is due to the small cross-sectional area of the droplet and the parabolic velocity profile giving the maximum velocity at the centre. However, at low flow velocities, further decreasing the droplet length resulted in a significant reduction in droplet velocity. This reduction in droplet mobility is believed to be due to buoyancy effects on the droplet position within the channel. A side view of a

water droplet flowing at two different velocities while being engulfed by FC40 (as the carrier phase) is shown in Figure 4.8. The buoyancy effect is noticeable at the lower flow velocity ($7.3\ mm/s$), with the droplet traveling closer to the top surface rather than the channel's centre. (see Figure 4.8(a)). While this vertical displacement of the droplet is almost diminished at the highest flow velocity ($44\ mm/s$), where a thicker film separates the droplet from the upper-side of the capillary wall (Figure 4.8(b)). As the flow velocity increases, a thicker film separates the droplet from the top surface, driving the droplet to the tube's centre and symmetrical with the capillary centre line. This enables the droplet to move faster as its body shifts away from the capillary wall, where the flow velocity is lower due to the parabolic velocity profile for the laminar flow across the channel.

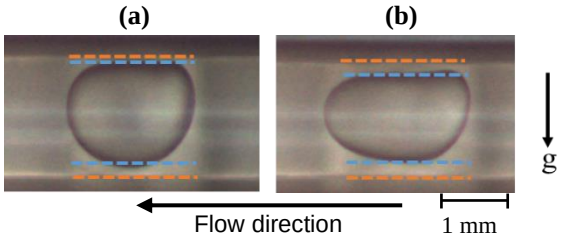

Figure 4.8. Images of water dispersed in FC40 with a constant droplet volume over velocities of (a) 7.3 mm/s and (b) 44 mm/s while the Bond number is 0.3. The capillary's inner diameter is 1.70 mm and the droplet length ratio (L_D/D) is measured to be 1.1 at the lower flow velocity.

The Bond number (ratio of buoyancy to interfacial tension forces, $\Delta\rho g D^2/\gamma$) for AR20_Water is 0.11, whereas in cases with FC40_Water and HFE7500_Water, Bond numbers are determined to be 0.3 and 0.47 respectively. Hence, in comparison to AR20_Water, the buoyancy force is expected to have a greater impact on flow characteristics for FC40_Water and HFE7500-Water. In a numerical study by Zheng *et al.*(2007), the effect of Bond number on the film thickness over liquid-gas flows was investigated. Their findings revealed that as the Bond number increases, the ratio of the upper to lower film thickness ($\frac{\delta^+}{\delta^-}$) decreases but increases with the Capillary number. For a small Bond number (Bo=0.1), the ratio ($\frac{\delta^+}{\delta^-}$) increases linearly with Ca, while for a higher Bond number ($Bo = 0.6$) and low Ca, it grows with a steeper non-linear trend.

Figure 4.9(a) and (b) present the results of FC40_Water and HFE7500_Water experiments performed with lower Bond numbers of 0.05 and 0.04 respectively. In order to achieve lower Bond numbers, these set of experiments with FC40_Water and

HFE7500_Water were carried out using capillaries with diameters of $550\ \mu m$ and $580\ \mu m$ respectively. In these cases, the lower Bond numbers allow eliminating the influence of buoyancy forces but compare the results to the previous experiments with relatively higher Bond number values.

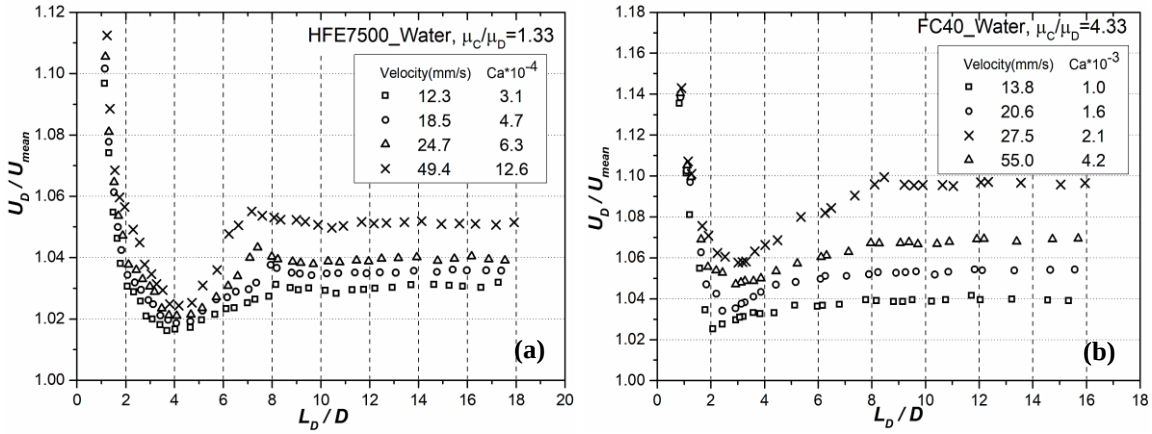

Figure 4.9. Variation in droplet velocity ratio with dimensionless droplet length for experiments with (a) HFE700_Water, Bo $= 0.04$ and (b) FC40_Water, Bo $= 0.05$.

In these cases, the influence of buoyancy force on the droplet velocity of very small drops has been clearly negated over all flow velocities and graphs exhibit a similar trend to AR20_Water (with $\mu_C/\mu_D \gg 1$ and $Bo = 0.11$). Also, FC40_Water and HFE7500_Water experiments with lower Bond numbers (as shown in Figure 4.9), present more defined crossover zones with an increased depth (see Appendix H). Hence, the internal flow topology of the droplet appears to be affected by the buoyancy force as well. A higher Bond number causes the droplet to move closer to the capillary's top-side, resulting in a significant flow leakage (significant film velocity) on the lower-side and almost a stagnant film on the upper-side. Consequently, the droplet is subjected to uneven shear stresses which affects its internal flow patterns. In a numerical study by Zheng *et al.*(2007), Bond number is shown to affect the flow around the dispersed phase. They highlighted that the flow topology of the continuous phase becomes asymmetric in respect to the centre line when $Bo \neq 0$, and there are flow interactions between upper and lower domains. While, in the case with $Bo = 0$, both upper and lower flow domains are found to be independent with no flow interaction between them.

4.3.3. Low Viscosity Ratios ($\mu_C/\mu_D \ll 1$)

In order to evaluate the mobility of high-viscous droplets, AR20 with a high viscosity ($\mu_D = 21.3$) was dispersed in HFE7500 ($\mu_C = 1.3$) and FC40 ($\mu_C = 4.3$) which resulted in

very small carrier to droplet viscosity ratios of $\mu_C/\mu_D = 0.059$ and $\mu_C/\mu_D = 0.186$ respectively. The results from these experiments are presented in Figure 4.10. Capillaries with inner diameters of $800\,\mu m$ and $1.70\,mm$ were used in HFE7500_AR20 and FC40_AR20 resulted in Bond numbers of 1.66 and 3.26 respectively.

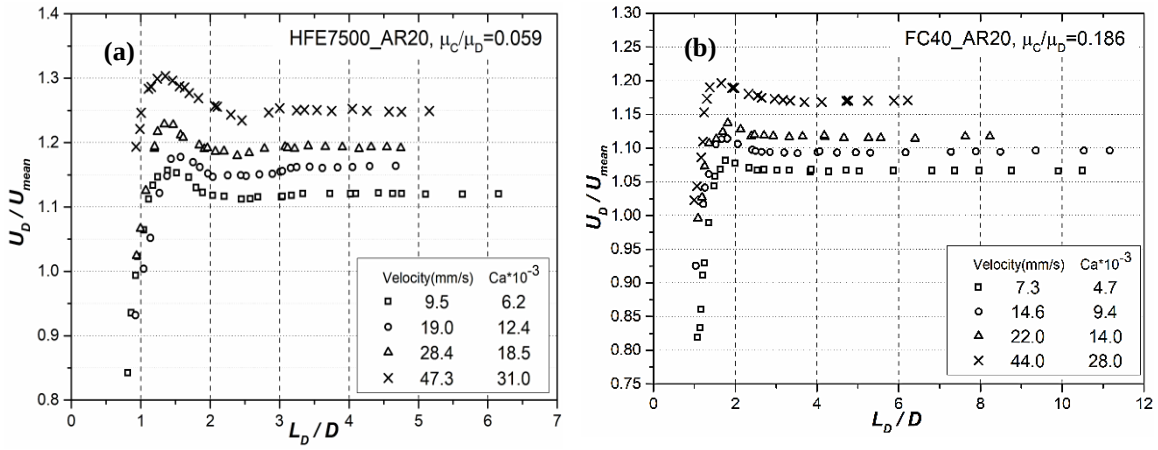

Figure 4.10. Variation in droplet velocity ratio with dimensionless droplet length for experiments with (a) HFE7500_AR20, Bo = 1.66 and (b) FC40_AR20, Bo = 3.26.

Figure 4.10(a) and (b) present a similar trend in droplet velocity ratio with a slight difference at the crossover region (see Appendix H). The velocity ratio (U_D/U_{mean}) in both graphs becomes almost constant as L_D/D exceeds ~3. The velocity ratio in HFE7500_AR20 shows a modest decline as the droplet length ratio falls below ~3, however this reduction is not observed in FC40_AR20. As the droplet length is reduced further, the velocity ratio rises until its length shrinks to a value of L_D/D ~ 1.5. Further reduction in the droplet length resulted in a significant decrease in droplet mobility. In FC40_AR20 and HFE7500_AR20, the high Bond numbers of 3.26 and 1.66 respectively, mean that the droplet is subjected to a greater buoyancy force. As previously stated, a significant buoyancy force causes the droplets to move towards the upper wall, resulting in a notable reduction in the velocity of short drops.

Figure 4.11 displays side-view photos captured from experiments with HFE7500_AR20 in which a droplet of AR20 is dispersed in HFE7500 while flowing at two different mean flow velocities of (a)9.5 mm/s and (b)47.3 mm/s. The inner capillary diameter is $800\,\mu m$ and the droplet length ratio (L_D/D) at the lower flow velocity is measured to be 1.2. At the flow velocity of $9.5 mm/s$ (Figure 4.11(a)), the buoyancy effect is clearly visible with the droplet being lifted towards the upper capillary wall. In this case, the lower wall's film thickness is several times that of the upper side. At the higher flow

velocity (Figure 4.11(b)), a thicker film on the upper wall pushes the droplet down toward the centreline, but the buoyancy effect is not completely eliminated and the droplet still moves asymmetrically in respect to the capillary centre line. Unlike, in the case of FC40_Water with a lower Bond number of 0.3 (see Figure 4.8), where the droplet's vertical displacement is diminished at the maximum flow velocity. This explains why the buoyancy effect on droplet mobility is minimal at the highest flow velocity in FC40_Water and HFE7500_Water (see Figure 4.7) with relatively lower Bond numbers (0.3 and 0.47) but not for HFE7500_AR20 and FC40_AR20 with higher Bond numbers (1.66 and 3.26).

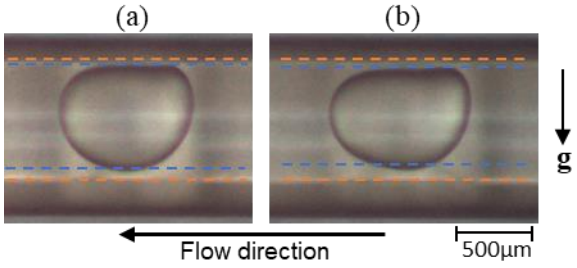

Figure 4.11. Images of AR20 dispersed in HFE7500 with a constant droplet volume over mean flow velocities of (a) 9.5 mm/s and (b) 47.3 mm/s at a Bond number of 1.66. The capillary's inner diameter is 800 µm and the droplet length ratio (L_D/D) is measured to be 1.2 at the lower flow velocity.

HFE7500_AR20 and FC40_AR20 experiments were also investigated in capillaries with smaller diameters of 580 μm and 550 μm, yielding lower Bond numbers of 0.85 and 0.34, respectively. The results from this set of experiments are graphed in Figure 4.12.

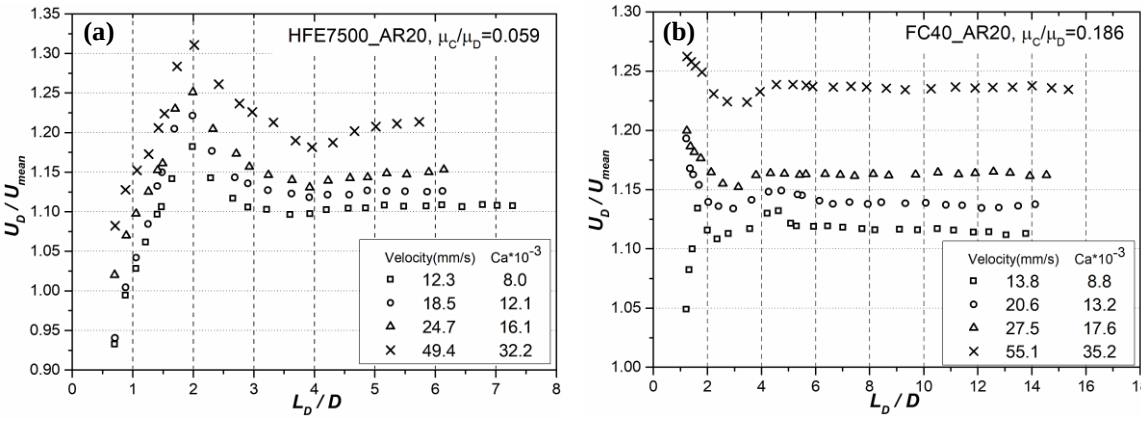

Figure 4.12. Variation in droplet velocity ratio with dimensionless droplet length for experiments with (a) HFE7500_AR20, Bo = 0.85 and (b) FC40_AR20, Bo = 0.34.

Figure 4.12(a) indicates that, despite the fact that the Bond number for HFE7500_AR20 was reduced from 1.66 to 0.85, the buoyancy force still has a significant impact on the mobility of short droplets, resulting in a rapid reduction in droplet velocity as the droplet length ratio falls below $L_D/D \sim 2$. While, in FC40_AR20 with a lower Bond number of 0.34, the buoyancy impact on short droplets is only observable at the lowest flow velocity ($13.8\ mm/s$) and disappears at higher flow velocities, as shown in Figure 4.12(b). At the higher flow velocities, the buoyancy effect on droplet placement is neutralized, as a thicker film on the upper wall drives the droplet down towards the centreline.

4.4. Discussion

In the previous section, the influence of droplet length ratio on droplet mobility was investigated and three distinct domains were identified: The results are schematically summarized in Figure 4.13, highlighting the impact of viscosity ratio, Bond number and Reynolds number on velocity ratio of a droplet at a specific Capillary number while varying the droplet length ratio.

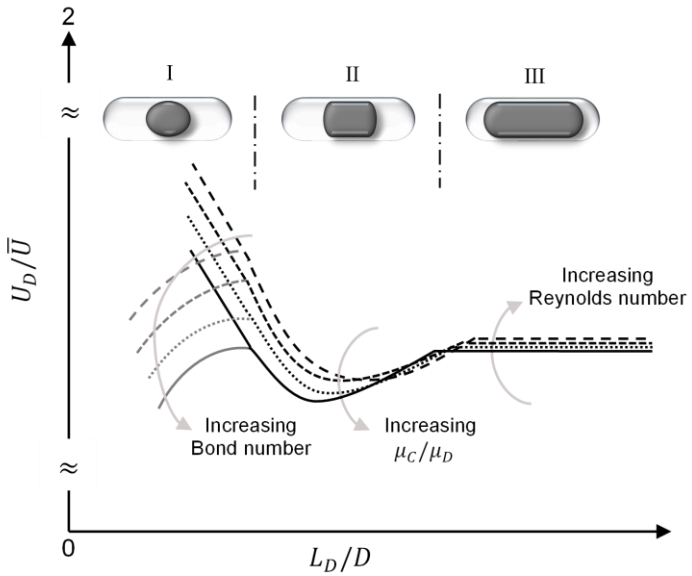

Figure 4.13. Schematic highlighting the impact of viscosity ratio, Bond number and Reynolds number on droplet velocity ratio at a specific Capillary number while varying droplet length ratio.

(I) For very short droplets, $L_D/D \lesssim 2$, the diameter of the droplet is noticeably smaller than that of the capillary and the ratio of capillary to buoyancy forces greatly impacts the droplet velocity. When capillary forces dominate, decreasing the droplet length boosts droplet mobility, whereas short droplets travel substantially slower than the mean flow velocity when buoyancy forces are dominant.

(II) For $L_D/D \gtrsim 2$, the plots showed a changeover zone in which the droplet velocity first decreases and then increases. This crossover area deepens as the carrier to droplet viscosity ratio (μ_C/μ_D) increases. The lack of well-formed internal circulations is believed to be the reason for velocity reduction in this region. The amplitude of this internal circulatory flow, as well as how well it is coupled with the outside flow, has a substantial impact on the droplet's hydrodynamic resistance (King *et al.* 2007). Droplet length, flow velocity and viscosity ratio are found to have a role in droplet's transition from a low to a high level of internal circulation. In addition to the internal flow topology, the buoyancy force is shown to influence the droplet velocity in this zone.

(III) As the droplet length exceeds the cross over zone, the droplet relative velocity (U_D/U_{mean}) becomes almost constant and droplet length no longer affects drop velocity. According to the data analysis, the commencement of this plateau zone greatly depends on the Capillary number and weakly on Reynolds and Bond numbers. Equation 4.4 gives an estimation of the minimum droplet length ratio ($\left(\frac{L_D}{D}\right)_{Threshold}$) required to enter the plateau zone for each flow combination. This correlation is obtained by data regression with the aim of determining the least RMS error using iterative numeric procedures by Solver function in Excel file. The Solver function is employed in data regression to find the best-fitting mathematical model by minimizing the sum of the squares of the differences between the observed data points and the predicted values. Through an iterative process, Solver adjusts the model's coefficients until the sum of squared differences is minimized, resulting in an optimized fit for the data. In this correlation, the droplet velocity and continuous phase properties are employed to determine the Capillary ($Ca = \mu_C U_D/\gamma$) and the Reynolds ($Re = \rho_C U_D D/\mu_C$) numbers.

$$\left(\frac{L_D}{D}\right)_{Threshold} = 1.25(Re \times Bo)^{0.05} Ca^{-0.25} \qquad (4.4)$$

In Figure 4.14, experimental measurements are compared with the correlation presented in Eq. 4.4, with the vertical and the horizontal axes representing experimental

and the model's estimation respectively. The model's accuracy is highlighted by dashed-lines giving $\pm 20\%$ deviations from the correlation.

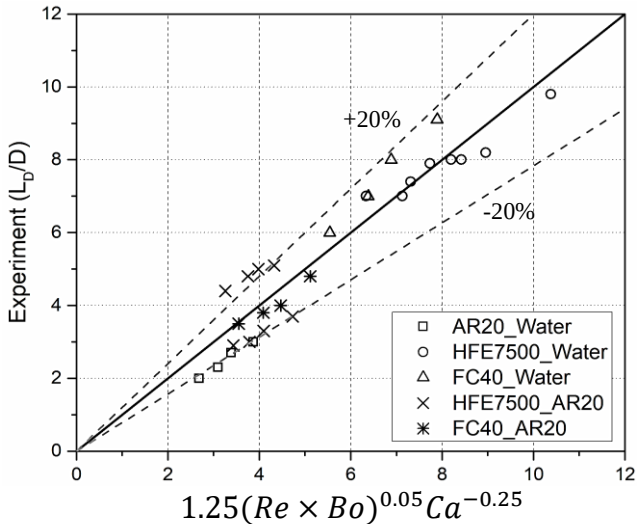

Figure 4.14. Experimental minimum droplet length ratio (L_D/D) required to enter the plateau zone compared to prediction calculated using Eq. 4.4.

In the plateau zone, the droplet velocity ratio (U_D/U_{mean}) increases as the Capillary number increases. Figure 4.15 shows how droplet velocity ratio changes with Capillary number. Each data point in this graph represents the mean values of the data recorded for each flow velocity located in the plateau zone. In this plot, the solid line presents the best-fit curve for the scattered data and dashed-lines are 10% deviations from the curve. A linear data regression is applied to determine the trend line's power.

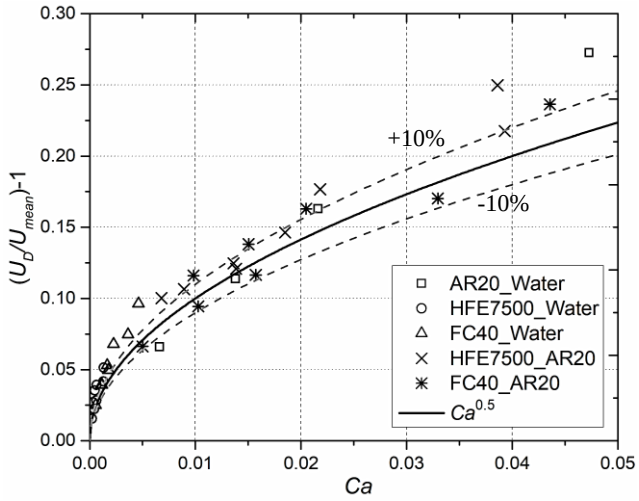

Figure 4.15. Variation in droplet velocity ratio as a function of the Capillary number. Each data point in this graph is the averaged value of the data located at the plateau zone at each flow velocity.

The result implies that the droplet velocity ratio increases as a function of $\sim Ca^{0.5}$ which is the exact value first suggested by Fairbrother and Stubbs (1935). They conducted the first attempt to assess the flow of second phases in circular capillaries by blowing air into a capillary filled with a viscous fluid and measuring the amount of liquid left behind on the capillary wall. Their empirical model was indorsed by Taylor (1961) for very small Capillary numbers ($Ca \leq 0.09$). Also, Schwartz *et al.*(1986) replicated Bretherton's tests for long and short bubbles, and their measurements for long bubbles demonstrated that the correlation by Fairbrother and Stubbs (1935) better models the data than the Bretherton's theory.

In Equation 4.5 a new correlation is suggested by the current authors to better predict droplet velocity in liquid-liquid Taylor flow regimes. This model is achieved by means of a linear data regression and includes the effects of Bond and Reynolds numbers. In this equation, Reynolds number is determined based on the continuous phase properties.

$$\frac{U_D}{U_{mean}} - 1 = 0.8\left(\frac{Re}{Bo}\right)^{0.1} Ca^{0.5} \tag{4.5}$$

Figure 4.16 illustrates an evaluation of this model, where the vertical axis represent results from the experiments and the horizontal axis is the model's estimation of the drift velocity.

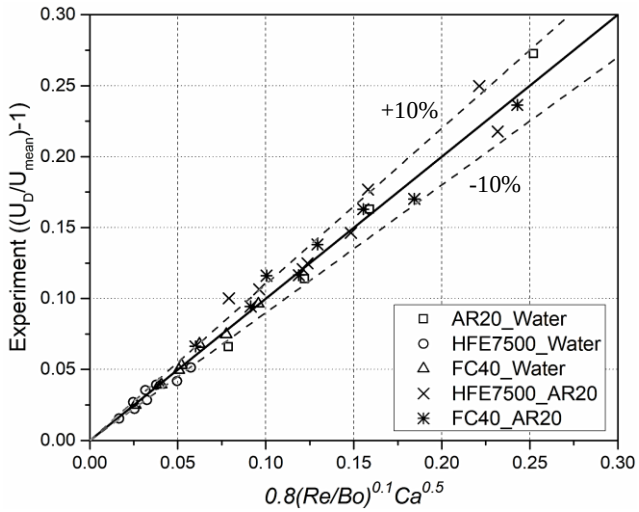

Figure 4.16. Experimental droplet drift velocity plotted against theoretical prediction calculated using the correlation described by Eq. 4.5.

From this figure, the majority of the data points are located within the $\pm 10\%$ bandwidth of the predicted values. Therefore, this model shows an excellent capability of estimating droplet velocity in liquid-liquid slug flow regimes where droplet length no longer affects drop velocity.

Various computational and experimental investigations have proven the effect of Reynolds number on droplet/bubble shape and film thickness (Edvinsson and Irandoust 1993; Giavedoni and Saita 1999; Lac and Sherwood 2009). A numerical study by Kreutzer *et al*.(2005b) shows that when Reynolds number increases, the bubble nose elongates and the rear of the bubble flattens. It has been pointed out that the inertia of the circulating liquid creates a significant dynamic pressure increase at high Reynolds numbers, which causes the bubble shape to vary in accordance with the Laplace pressure term. Therefore, the inclusion of Reynolds number in the correlation seems reasonable, given that droplet shape is one of the most important factors in determining droplet velocity.

Overall, the results reveal that droplet velocity is influenced by a complicated interrelationship of numerous factors. Previous investigations performed over two-phase flows (liquid-liquid / liquid-gas) within micro/milli capillaries assumed a negligible effect of buoyancy forces due to a very narrow cross-sectional area of the capillary. While this research shows that buoyancy can considerably impact droplet hydrodynamics even in liquid-liquid flows (with the comparable densities of phases) within capillaries of very small diameters ($\sim 500\ \mu m$). In addition, in previous studies predicting droplet velocity, droplet length was shown to have no effect on velocity by assuming the droplet was large enough to occupy the whole channel cross section ($L_D/D \gtrsim 1$). Whereas, according to findings of the current study, droplet velocity only becomes independent of its length as the droplet length exceeds a certain threshold (in some cases eight times greater than the capillary diameter, $L_D/D > 8$). The beginning of this threshold is estimated in Eq. 4.4 and found to be influenced by Capillary, Bond and Reynolds numbers. According to the findings of the current investigation, small variations in droplet length below the threshold lead to noticeable changes in droplet velocity. Thus, this study recommends using droplets longer than the minimal threshold, estimated by the correlation in Eq. 4.4, to avoid coalescence of adjoining drops in applications where droplet coalescence is an undesired phenomenon (e.g. DNA analysis and protein crystallisation). Above this threshold, where the droplet velocity is independent of its length, Eq. 4.5 can be used to predict the velocity with a high degree of accuracy. This model assists in the attainment of an optimal

configuration in the related applications by estimating droplet velocity and also revealing effective parameters. Transportation, analysis, detection, and monitoring are among the procedures applied in biological or chemical applications, each needing precise spatial and time control data for droplets.

4.5. Conclusions

Velocity of individual droplets in liquid-liquid Taylor flow was investigated experimentally by means of a novel fully-automated apparatus. The experiments were performed over five different fluid combinations resulting in extensive ranges of Reynolds number ($0.7 < Re < 104$), Bond number ($0.05 \ll Bo \ll 3.26$), viscosity ratio ($0.186 \ll \mu_C/\mu_D \ll 23.2$) and droplet length ratio ($0.7 \leq L_D/D \leq 18$) ratios. This wide range allowed for a better insight into how these elements influence droplet mobility. The results indicate a complex dependency of droplet velocity on various parameters including droplet length, viscosity ratio, Reynolds and the Bond number.

In trials with short droplets ($L_D/D \lesssim 2$) and low Bond numbers, droplets are able to move considerably faster than the mean flow velocity by flowing away from the stagnant region near the capillary wall and towards the capillary's centre with the maximum flow velocity. As the Bond number increases, buoyancy forces exert influence over interfacial forces, causing the droplet to move asymmetrically with respect to the channel centre line. This phenomenon along with the parabolic velocity profile in the carrier phase, results in a significant reduction in the velocity ratio of short drops. As the droplet length becomes longer, the droplet velocity faces a transition area in which the velocity initially declines and then rises by further increase in the droplet length. The velocity reduction in this area is believed to be caused by the flow topology inside the droplet. The effect becomes stronger as the carrier to droplet viscosity ratio increases. As the droplet length surpasses a certain value, the droplet velocity ratio (U_D/U_{mean}) becomes independent from its length and increases as the Capillary number increases. This increase is believed to be caused by the film thickening around the droplet, and has been found to be correlated as a function of Capillary, Bond and Reynolds numbers.

Overall, this article hopes to provide an incremental comprehension on the liquid-liquid slug flow hydrodynamics as well as profound insights to facilitate microfluidic device optimization

Chapter 5

Experimentally Investigating the Pressure Drop of Liquid-Liquid Taylor Flows Over Varying Viscosity Ratios

Experimentally Investigating the Pressure Drop of Liquid-Liquid Taylor Flows Over Varying Viscosity Ratios

Chapter on Published Journal Article (Under Review)

International Journal of Multiphase Flow[1]

Seyyed Saeed Shojaee Zadeh*[a], Vanessa Egan[b], Pat Walsh[c]

*****Corresponding Author

[a] CONNECT Centre, Stokes Laboratories, Bernal Institute, School of Engineering, University of Limerick, Ireland, V94T9PX. E-Mail: saeed.zadeh@ul.ie, Tel:+353873818619, ORCID: 0000-0003-1359-7232

[b] CONNECT Centre, Stokes Laboratories, Bernal Institute, School of Engineering, University of Limerick, Ireland, V94T9PX. E-Mail: vanessa.egan@ul.ie, ORCID: 0000-0001-8828-6303

[c] Stokes Laboratories, Bernal Institute, School of Engineering, University of Limerick, Ireland, V94T9PX. E-Mail: pat.walsh@ul.ie

Abstract

Micro-capillary liquid-liquid Taylor flows have emerged as a promising new platform for achieving higher heat and mass transfer compared to single-phase flows. In any application benefiting from such flows, pressure drop is a fundamental characteristic in evaluating the required input power in order to achieve an optimum configuration. Despite several attempts to develop an all-encompassing model to estimate pressure drop in immiscible liquid-liquid flows, existing models are still limited to narrow ranges of Reynolds, Capillary and Weber numbers and are insufficiently accurate over a wide range of viscosity ratios. To push the limits, the present study proposes a new expression for interfacial pressure drop based on experimental investigations over a wide range of Capillary ($3 \times 10^{-4} \leq Ca_C \leq 7.6 \times 10^{-2}$)*, Reynolds* ($0.1 \leq Re_C \leq 49$) *and Weber* ($7 \times 10^{-4} \leq We \leq 1.5$) *numbers while carrier to dispersed viscosity ratio* (μ_C/μ_D) *spanned from* 0.058 *to* 24.2*. To obtain these ranges, five distinct liquid-liquid fluid combinations were examined within a capillary of diameter 800 µm. A novel experimental setup is employed in this study to ensure high accuracy and repeatability of the measurements. The strengths and weaknesses of existing models are identified and a more fundamental understanding of predicting pressure drop in Taylor flow regimes is developed. The new model uses standard Hagen-Poiseuille flow theory in combination with an empirical optimized term for predicting the effect of differential Laplace pressure between leading/trailing caps of dispersed phase droplets. This correlation fits the experimental data within* $\pm 20\%$ *and can provide a prediction certainty for estimating pressure drop in applications that deal with such flows.*

Keywords: *viscosity ratio, liquid-liquid, Taylor flow, pressure drop.*

[1] See Appendix A for publication reference.

5.1. Introduction

Over the past few decades, the limitations of traditional thermal management methods have become more evident as heat fluxes in electronic components have increased in tandem with significant miniaturization. Forced convective air cooling and microchannel heat sinks with single-phase liquid flows can provide heat dissipation of up to 150 and 790 W/cm^2 respectively (Tuckerman and Pease 1981; Hamann *et al.* 2006). However, in applications using laser diode arrays, heat fluxes can skyrocket to 1000 W/cm^2 (Roy and Avanic 1996). Applying direct liquid cooling such as pool boiling, jet impingement and spray cooling, these systems can provide high heat transfer coefficients by taking advantage of the latent heat of the liquids (Fabbri *et al.* 2005; Jeffers *et al.* 2009; Hotta and Patil 2018). However, despite the attractive thermal behaviour of direct liquid cooling systems with or without phase change, these methods are still insufficient and more complex from a use and design point of view, as they require additional maintenance procedures for hot swapping electronic parts (Ebadian and Lin 2011).

Liquid-liquid slug flows in microchannels provide a high surface area to volume ratio and internal circulations within the slugs not only offer a high heat transfer rate from the channel wall (Mac Giolla Eain *et al.* 2015) but also result in enhanced mass transfer between immiscible phases (Kreutzer *et al.* 2005a; Kashid *et al.* 2010). Several experimental and numerical studies have shown enhanced heat transfer rates of up to 700% compared to traditional single-phase flows (Mac Giolla Eain *et al.* 2015; Abdollahi *et al.* 2020a). Microreactors, microfiltration and oil recovery are examples of practically observed efficiency enhancements using liquid-liquid slug flows to promote the mixing rate (Schwartz *et al.* 1986; Burns and Ramshaw 2001). Also, in biomedical research, liquid-liquid Taylor flows in microchannels have been employed for synthesis of nano materials, DNA analysis and to achieve more realistic settings by mimicking the blood flow within the vessels (Burns *et al.* 1998; Kandlikar *et al.* 2005; Taly *et al.* 2007).

Heat and mass transfer enhancements are always entwined with pressure drop evaluation and, in most applications, the pressure drop value defines the margin of the progression. In all applications employing Taylor slug flows, designers need a comprehensive understanding of how such flows behave in order to secure desired flow rates and achieve an optimal design. In this regard, pressure drop is the main governing factor in determining pump size, input power requirements and overall system cost.

In general, Taylor flows are classified into two different types; liquid-liquid and liquid-gas slug flows. A fundamental understanding of the hydrodynamics of these flow regimes was achieved through a pioneering publication by Bretherton (1961). Until recently, relevant research in this area has tended to focus on liquid-gas flows with the majority of published pressure drop models focusing on these flows. Comparatively, there are substantially fewer studies on pressure drop models for liquid-liquid flows. In terms of heat transfer enhancement, liquid-liquid flows demonstrate much better performance compared to gas-liquid flows (Howard *et al.* 2011; Mac Giolla Eain *et al.* 2015) and, as such, a number of studies have recently been conducted resulting in semi-empirical correlations and models for pressure drop (Kashid and Agar 2007; Jovanović *et al.* 2011; Mac Giolla Eain *et al.* 2015). Despite this research however, these models tend to be based on limited test conditions of Reynolds, Capillary, and Weber number and viscosity ratio. In most cases, researchers hope to generalize the results to other test conditions, however due to the complicated hydrodynamics of two-phase flows, extrapolations of correlations beyond the limits for which they were derived, may lead to poor predictions.

Generally, two different approaches are used for modelling pressure drop in liquid-liquid slug flows. The first assumes a considerable contribution of the dispersed phase in the total pressure drop and the second approach assumes a significant role of the thin liquid film, which separates the slugs (dispersed phase) from the capillary wall, in the total pressure drop. Kashid and Agar (2007) developed correlations, based on both approaches, by conducting experiments with varying slug sizes and capillary diameter for carrier to dispersed viscosity ratios greater than unity. Their model, using the first approach was found to over-predict pressure drop while the second approach presented good agreement with their experimental results. Subsequently, Jovanović *et al.* (2011) developed a further two models for liquid-liquid pressure drop prediction; a stagnant-film and moving-film model. Their results showed a negligible effect of film velocity on pressure drop. Therefore, both models were found to be very similar in prediction and the stagnant-film model was assumed sufficiently accurate. In their study, carrier to dispersed phase viscosity ratios were also greater than unity.

Following these studies, Mac Giolla Eain *et al.* (2013, 2015a) conducted an experimental study over a range of variables, including Capillary and Reynolds numbers, resulting in two different correlations predicting pressure drop in Taylor flows. First, they proposed a correlation to determine the skin-friction coefficient for liquid-liquid slug flows

by focusing on the interfacial contribution in overall pressure drop (Mac Giolla Eain *et al.* 2013b). In their experiments, carrier to dispersed viscosity ratios ranged between $\sim 1.3\ to\ \sim 21$. The proposed correlation showed good agreement with experimental results as the majority of the data points were positioned within the 15% error bandwidth of the model. Subsequently, they developed a universal model to predict pressure drop in both liquid-liquid and liquid-gas slug flows in the form of frictional losses (Mac Giolla Eain *et al.* 2015). This model was attained by modifying a model proposed by Warnier *et al.* (2010) (for liquid-gas slug flows) and showed a maximum error of 20% from the experimental data. Recently Adrugi *et al.* (2016) from experiments in small-scale tubing, proposed a theoretical model, based on a force balance, in which slug length and capillary number were found to be the only effective parameters on pressure drop of liquid-liquid slug flows. In this study, low viscosity oils were used as the carrier phases and water as the dispersed phase which resulted in a carrier to dispersed viscosity ratio of ~ 0.5 to ~ 5. The proposed model does show good agreement with experimental data with a maximum deviation of 15% for Reynolds number ranges from $\sim 50\ to\ \sim 250$, however the effects of viscosity ratio are not fully evident as an averaged viscosity for the two-phase mixture was used in the model.

Aside from the aforementioned cases, there are other correlations for estimating pressure drop of liquid-liquid flows in the literature. These models are primarily employed to determine solutions for any type of two-phase flow, regardless of flow regime, in a completely different technique than Taylor flow modelling (Cicchitti *et al.* 1959; Chisholm 1967; Lin *et al.* 1991; Salim *et al.* 2008). It has been observed that the majority of those models are restricted to specific flow conditions and generally exhibit unsatisfactory concurrence with experimental data (Jovanović *et al.* 2011;Mac Giolla Eain *et al.* 2015).

Among the existing pressure drop models for liquid-liquid Taylor flow regimes, the stagnant-film and moving-film models by Jovanović *et al.* (2011) and the skin-friction model proposed by Mac Giolla Eain *et al.* (2013b) are the most accepted and widely referenced in the literature. These models were developed by conducting experiments over a range of flow parameters and comparison of results with previous models. Despite the widespread acceptance of these models, there are still some limitations that need to be addressed. The current authors have identified four main issues with these models, which require attention and resolution: (i) The correlations are based on experiments involving flows with carrier to dispersed phase viscosity ratios greater than unity. This is similar to

liquid-gas flows where the viscosity of the carrier phase is always much greater than the dispersed phase ($\frac{\mu_C}{\mu_D} \gg 1$) and results in negligible frictional losses due to the dispersed phase. However, in liquid-liquid flows, a liquid with a comparably lower viscosity can segment the dispersed phase. This results in an increased contribution of the dispersed phase to pressure drop, making the prediction more complicated. In an effort to minimize pressure drop and overall energy cost, low-viscous carrier fluids have been employed to envelop highly viscous liquids in a variety of scientific and engineering applications, including lubricated pipelining (Joseph and Renardy 2013), multi-component polymeric flows (Everage Jr 1973; Khomami and Su 2000), and volcanic conduits (Carrigan and Eichelberger 1990). In such applications, the carrier phase functions as a lubricant to prevent the high-viscous fluid from being directly in contact with the channel wall. Also, depending on the viscosity ratio of the involved fluids, the interfacial tension can significantly influence the overall pressure drop (Mac Giolla Eain *et al.* 2015). (ii) The previous models have been developed from low Weber number experiments in which surface tension always dominates over inertial forces. In the studies by Jovanović *et al.* (2011) and Mac Giolla Eain *et al.* (2013b), the maximum Weber number is ~0.7. Several researches have indicated that the Weber number has a significant impact on the thickness and shape of the film that engulfs the dispersed phase (Aussillous and Quéré 2000; Han and Shikazono 2009) and hence the overall pressure drop (Warnier *et al.* 2010). (iii) In Jovanović's 'moving' and 'stagnant' film models, the theoretical solution of Bretherton (1961) is employed to estimate the pressure drop caused by interfacial tension between phases. Taking this approach resulted in neglecting inertial effects and assuming a negligible liquid film thickness to radius ratio ($h/R \lesssim 0.01$) (Jovanović *et al.* 2011). However, numerous studies show that these assumptions are only valid for low Reynolds numbers ($Re < 1$) and within a certain Capillary number range ($10^{-4} < Ca < 10^{-1}$); outside these ranges Bretherton's theoretical solution is not valid (Aussillous and Quéré 2000; Mac Giolla Eain *et al.* 2013a). (iv) In the proposed model by Mac Giolla Eain *et al.* (2013b), the contribution of the interfaces towards total pressure drop was determined by assuming a stagnant-film around the droplets. However, this assumption is not acceptable in all cases. Particularly, in liquid-liquid flows when, for a considerable interfacial tension, a thicker film encloses the droplet and depending on viscosity ratio, the flow in the liquid film can be significant (same order to the mean flow velocity) (Gupta *et al.* 2013; Howard and Walsh 2013).

In order to address these concerns and develop a more comprehensive pressure drop model, the current study presents a set of measurements over a wide range of dimensionless parameters. These include Reynolds numbers from 0.8 to 206, Capillary numbers from 2.1×10^{-4} to 6.79×10^{-2}, Weber numbers from 3.3×10^{-3} to 7.58, carrier to dispersed viscosity ratios ($^{\mu_C}/_{\mu_D}$) from 0.059 to 23.2, and slug length to diameter ratios from 1.94 to 20.6. To achieve this, five different liquid-liquid combinations were examined by employing four liquids with different thermophysical properties, in capillaries with nominal inner diameter of $800\ \mu m$. To improve the measurement accuracy, a novel apparatus capable of accurately defining the morphology and velocity of each carrier/dispersed phase unit in the system was developed. This provides high confidence in the boundary conditions used for model development. This fully automated setup ensures a high degree of precision with a low level of uncertainty (less than 5%) by eliminating potential errors induced by operators.

This study contributes to the advancement of microfluidic devices incorporating liquid-liquid Taylor flows and offers a greater insight to this flow regime by identifying the limitations with the existing models. This is achieved through a comprehensive comparison between experimental results and the most well-known existing pressure drop models in the literature (Jovanović *et al.* 2011; Mac Giolla Eain *et al.* 2013b).

5.2. Experimentation

5.2.1. Experimental setup

Figure 5.1 illustrates a schematic of the automated experimental set up used in the current study. This experimental facility enabled (1) the generation of consistent liquid-liquid slug flows; (2) measurement of pressure drop along the test section; and (3) accurate measurements of carrier and dispersed phase length and (4) velocity of droplets. The apparatus consists of a Harvard Pico Plus Elite syringe pump (with an accuracy of $\pm 0.35\%$) located at one end of the tube and a traverse/dipping stage at another end. In order to generate consistent slug trains, the tube was first primed and flushed with a carrier liquid. Following this both liquids were drawn into the tube by running the syringe pump in withdraw mode and simultaneously cycling the traverse stage vertically in a reservoir containing both immiscible fluids. The traverse system and syringe are controlled and synchronized using a custom G-Code command in order to generate droplet trains

containing different dispersed phase lengths (L_D), carrier phase lengths (L_C) and unit cell lengths (L_u). As the tip of the tubing enters a liquid, the pump draws in the desired volume of that liquid. Carrier and dispersed phase lengths were varied by controlling the dwell time of the dipping stage and the flow rate on the syringe pump. Droplet trains were generated in FEP (Fluorinated Ethylene Propylene) Teflon tubes (with a rigid wall) supplied by Cole Parmer^{TM}. The tubing is orientated horizontally with nominal inlet diameter of 800 μm and length of 5.6 m. Inner diameters of the capillaries were confirmed using two different approaches: (1) by measuring the weight of a liquid filled length of tube and (2) measuring the time taken to fill a certain length of tubing with a specific flow rate set by the syringe pump. It is important in both procedures to use a virgin tube due to the fact that any trace of liquid within the tube causes the measured diameter to be lower than the actual value. According to the measurements, the nominal and actual inlet diameters of the tubing differ by up to 6%. 10 ml Hamilton gas tight glass syringes were used during testing to minimize any uncertainty caused by deformation of the barrel and piston during experiments.

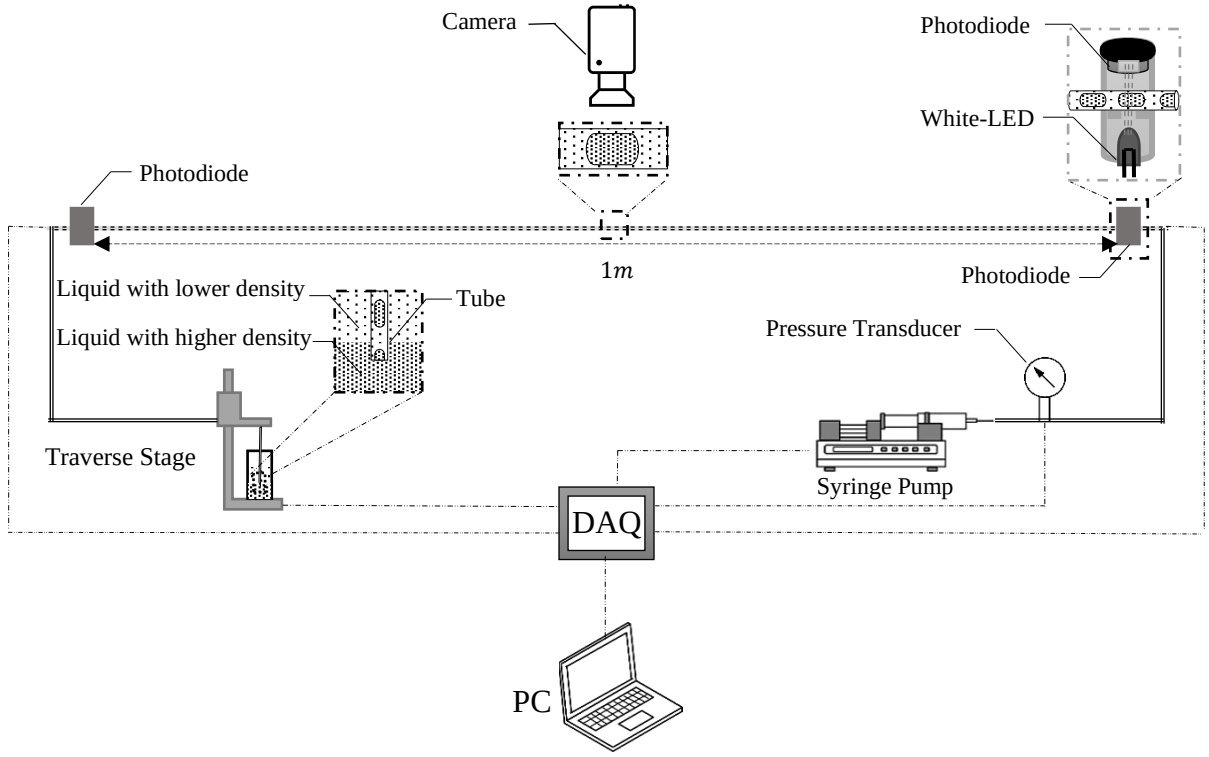

Figure 5.1. Experimental configuration used for pressure drop, slug length and velocity measurements.

The use of transparent tubing allowed droplet length, speed and spacing to be determined by means of two photodiodes and LEDs located along the tube, 1 m apart from each other, as shown in Figure 5.1. Photodiodes with integrated amplifiers (OPT301M),

provided by Burr-Brown and white LEDs (as light sources) with a maximum voltage of 3.4 v and current of 50 mA were used in this experiment. As shown in Figure 5.2(a), a plastic (PLA) holder was designed to hold the sensor and the light source and maintain them orthogonal to the tube axis. As a droplet passes each photodiode, the light intensity from white-LEDs to the photodiode changes due to reflection and different refractive indices of the carrier and dispersed liquids. This changing light intensity results in an output voltage trace from the photodiode. Similar to that shown in Figure 5.2(b). This trace was recorded at 4 kHz and analyzed using MATLAB to determine slug length (L_C), droplet length (L_D) and velocity of each droplet (U_D) in the system (see Appendix E).

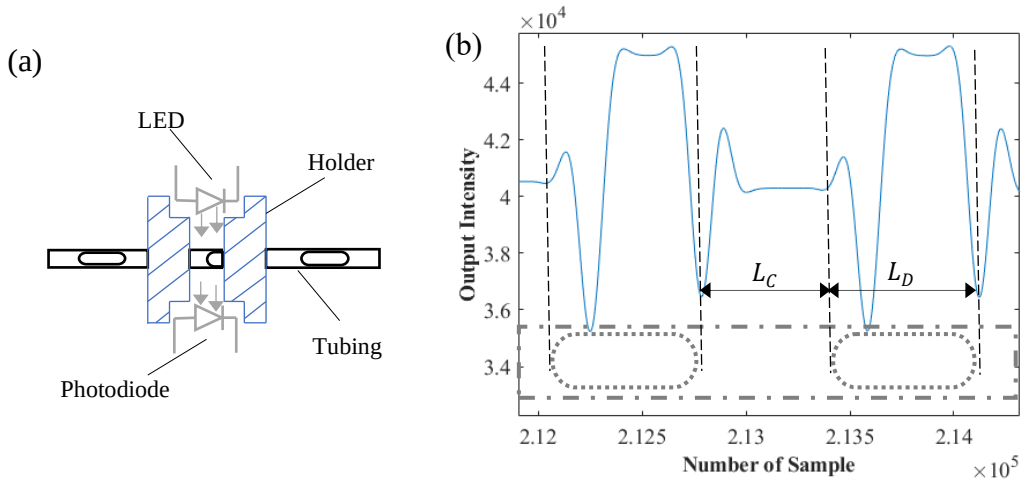

Figure 5.2. (a) Light sensor configuration and (b) example of recorded data used for droplet velocity and length measurements.

More details on the signal post-processing and the droplet length measurements are provided in (Zadeh *et al.* 2022). It is worth noting that different fluid combinations, as well as changes in the holder, tubing diameter, and light intensity, result in slightly different recorded signals.

The results from droplet length measurements show an excellent consistency in droplet length with a maximum variation of 6%. The maximum standard deviations of the carrier and dispersed phase lengths for each flow combination are provided in Table 5.1. The low standard deviations indicate that the majority of the data is firmly clustered around the mean value and in terms of length, both the carrier and dispersed phases are consistent. Figure 5.3 demonstrates an example of data for the measured droplet and continuous phases of a train. In this example, FC40 carries 85 droplets of water.

Table 5.1. The carrier and dispersed phase lengths' maximum standard deviations for all of the flow combinations investigated in this study.

Carrier_Dispersed	Maximum Standard Deviation in Length	
	Carrier	Dispersed
AR20_Water	3%	1.3%
FC40_Water	2.3%	2.1%
HFE7500_Water	1.6%	2.6%
FC40_AR20	5%	3.1%
HFE7500_AR20	4.3%	5.8%

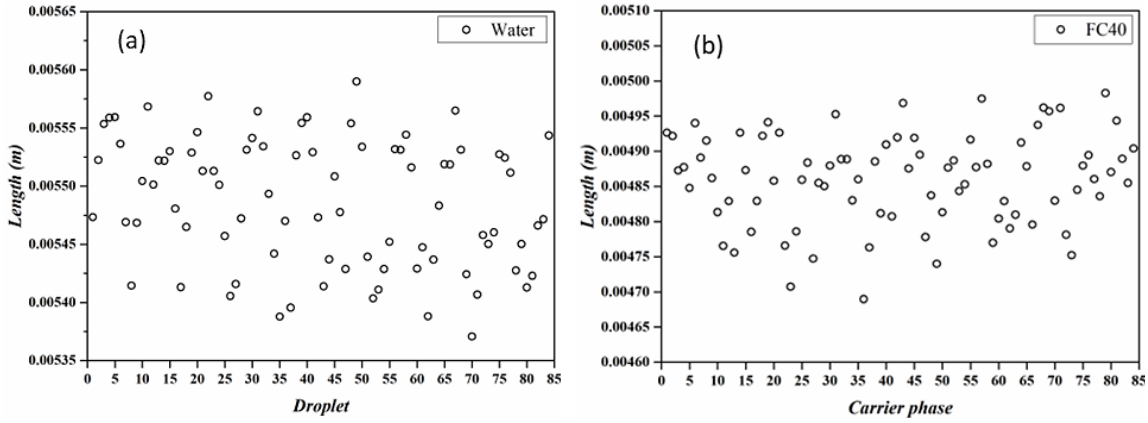

Figure 5.3. A sample results for (a) droplet and (b) carrier phase length measurements recorded from a train of FC40_Water.

Pressure drop was recorded using Honeywell gauge pressure transducers (26PCCFA6D) with ± 1, ± 5 and ± 15 PSI ranges, $1\ ms$ response time, $6.67\ mV/psi$ sensitivity and linearity of 0.5%. The appropriate pressure sensor is positioned $0.5\ m$ from the syringe pump and connected to the FEP tube with a T-Junction connector (see Figure 5.1). Prior to use, all three transducers were calibrated using Hagen-Poiseuille theory for single-phase flow in a circular tube with output voltage related to Hagen-Poiseuille pressure drop prediction (see Appendix D).

During experimentation, the dipping stage was used to fill a portion of the tube with a slug flow while the remaining length was filled with the carrier phase. Depending on number of the droplets and also droplet and slug length, the two-phase length of the capillary varied between $0.9m$ to $1.2\ m$. During the experiments, a range of 55 to 120 droplets was created and subsequently examined. This procedure allowed several tests to be performed using the same slug train by reversing flow direction and incrementing flow rates. This ensures more reliable results by keeping effective parameters such as slug and

droplet length constant throughout a set of experiments. The pressure drop due to the two-phase flow is obtained by subtracting the pressure drop in the single-phase sections of the tube, calculated by laminar flow theory, from the total pressure drop measured at the pressure transducer.

Silicon oil AR20 (Polyphenyl-methylsiloxane), fluorinert^{TM} FC40, hydrofluoroether HFE7500 and water were used in this study as the working liquids. FC40 and HFE7500 were supplied by ACOTA Ltd and AR20 was supplied by Sigma Aldrich Ltd. Prior to experimentation, all liquids were filtered twice to remove any trace of impurities. This was done using Millex® sterile syringe filters with a 0.45 μm pore size hydrophilic PVDF membrane. Afterwards, the interfacial tension of all liquids were measured using a commercial CAM 2000 Pendant Drop system. A CCD camera with maximum frame rate of 30 fps was used for visualization purposes. The viscosity of the liquids were determined by measuring the pressure drop along a certain length of the tubing and applying the Hagen-Poiseuille equation for laminar flow in a straight, circular capillary. These procedures were carried out over a wide temperature range in order to determine the temperature-viscosity characteristics of the fluids. Thermophysical properties of the fluids and range of dimensionless groups investigated in this are tabulated in Table 5.2 and Table 5.3 respectively. It is worth noting that in all experiments with water, deionized water (DI water) has been used to ensure high purity and eliminate any effects caused by a charge being present.

Table 5.2. Thermophysical properties of the fluids investigated at $\mathbf{20}$℃.

Liquid	Density $\left(\frac{\boldsymbol{kg}}{\boldsymbol{m^3}}\right)$	Viscosity $\left(\frac{\boldsymbol{kg}}{\boldsymbol{m.s}}\right)$
Water	998	0.0010
FC40	1854	0.0051
HFE7500	1620	0.0014
AR20	1142	0.0242

Table 5.3. Range of dimensionless groups investigated in current study.

Carrier/Dispersed	Interfacial Tension (γ) $\left(\frac{N}{m}\right)$	Re_C	Ca_C	L_C^*	L_D^*	We	Viscosity Ratio (μ_C/μ_D)
AR20/Water	0.03	0.1-1	4.2×10^{-3} 2.4×10^{-2}	10.4-20.6	2.15-6.5	7×10^{-4} 1.7×10^{-2}	24.2
FC40/Water	0.051	0.9-15	9.6×10^{-4} 4.8×10^{-3}	3.05-5.6	1.94-6.47	1.7×10^{-3} 7.2×10^{-1}	5.1
HFE7500/Water	0.049	8-49	3×10^{-4} 1.5×10^{-3}	6.25-8.75	1.94-4.56	2.5×10^{-3} 6.2×10^{-2}	1.4
FC40/AR20	0.006	2.6-16	1.4×10^{-3} 7.6×10^{-2}	6.47-7.72	2.1-5.18	3.1×10^{-2} 0.9	0.21
HFE7500/AR20	0.0019	8.6-19	7.7×10^{-3} 1.6×10^{-2}	10.4-14.8	1.34-3.82	6.2×10^{-2} 1.5	0.058

5.2.2. Uncertainty analysis

The uncertainty analysis is accomplished by using the 95% confidence formulation provided by Figliola and Beasley (2020). Considering length, flow rate, weight and time as the independent variables, an uncertainty value of 0.2% is determined for the tubing diameter. Maximum inaccuracy of 1 mm for tube length, 0.5% for flow rate, $10^{-2}g$ for weight and $10^{-3}s$ for time were considered to determine the uncertainty values. Maximum uncertainty for Capillary number, Reynolds number and pressure value, assuming 1% error in fluid properties, were found to be 2%, 3% and 5% respectively. To ensure repeatability of results, each test was repeated several times and the average values were used.

5.3. Results

This section presents the experimental results from pressure drop measurements over five different fluid combinations. In three cases, slug flows were created by aqueous slugs dispersed in a continuous oil phase of AR20, FC40, and HFE7500, whereas for the remaining two cases AR20 was segmented within FC40 and HFE7500.

Figure 5.4 presents the variations in total pressure drop with mean flow velocity over a range of 4 to 48 mm/s. The mean flow velocity is determined based on the mean flow rate set by the pump and the cross-sectional area of the tubing. This plot represents the overall experimentally measured pressure drop which ranges from 1.2 to 28 kPa. Also, three lines, represented by solid, dashed, and dotted styles, are superimposed on the graph to indicate the pressure drop of the respective carrier single-phase flows along the test section. The plot demonstrates a significant data scattering where different pressure drop values are recorded for a specific fluid combination at a given flow velocity. This is a result of measurements with various slug lengths and numbers, and among the tested fluid mixtures, FC40_Water exhibits the largest variance; whereas this variation is minimal in HFE7500_AR20.

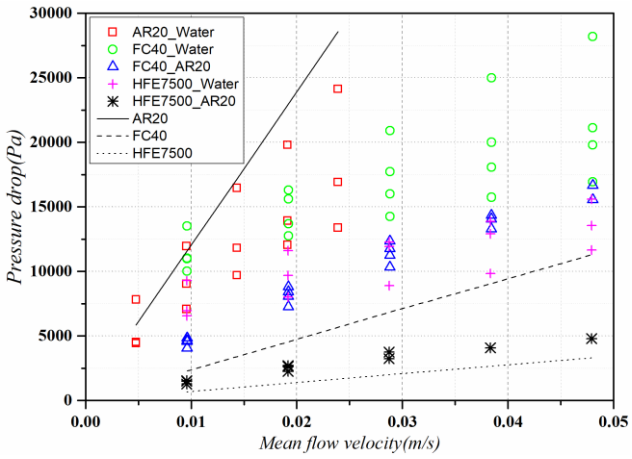

Figure 5.4. Plot of the total pressure drop against mean flow velocity for all the tested fluid combinations. Each line corresponds to pressure drop of a specific single-phase flow.

In liquid-liquid slug flow regimes, the overall pressure drop (ΔP_T) is considered to be the sum of the pressure drop in the carrier (ΔP_C) and dispersed (ΔP_D) phases in addition to the contribution of interfacial pressure drop (ΔP_{Int}) arising from the shared interfaces of the liquids, i.e. the differential Laplace pressures between leading and trailing droplet caps.

$$\Delta P_T = \Delta P_C + \Delta P_D + \Delta P_{Int} \tag{5.1}$$

The dispersed and continuous slug pair depicted in Figure 5.5 form each of the slug unit cells used in the Taylor flow modelling technique. In this figure l_d, l_c and l_u refer to dispersed, carrier and unit cell lengths respectively.

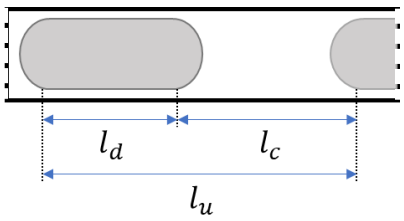

Figure 5.5. Schematic of the unit cell configuration using in a slug flow modelling.

By taking this approach, a number of studies have investigated the pressure drop in Taylor flow regimes with the majority focusing on liquid-gas flows. In liquid-gas flows, the contribution of the dispersed phase has been neglected due to the negligible viscosity of the dispersed gas. Assuming fully developed laminar flow with a parabolic velocity profile across the channel, the pressure drop across the carrier phase (ΔP_C) can be simply characterized by the Hagen-Poiseuille equation ($\Delta P = 32\mu UL/D^2$) by knowing the fluid viscosity (μ), velocity (U), capillary length (L) and diameter (D). As a result, the interfacial pressure drop is determined by subtracting the carrier phase pressure drop from the experimentally measured overall pressure drop. While in liquid-liquid flows taking the same approach to determine pressure drop across the droplet may not lead to correct results. In liquid-liquid flows, a thin liquid layer of the carrier phase acts as a separator between the droplet and the capillary wall. The viscosity gradients at the interface of two immiscible liquids leads to the development of a distinctive velocity profile within the liquid film, which differs from that of the carrier phase (Ładosz and von Rohr 2018). Therefore, precise and reliable calculation of the pressure drop across the dispersed phase is required in addition to the interfacial pressure drop's contribution.

In this regard, various models have been proposed to correlate the viscous pressure drop of the dispersed phase in liquid-liquid flows while primarily highlighting the need for determining the role of film thickness. In general, three different approaches might be taken to estimate the pressure drop along the dispersed slugs: by assuming (i) no-film, (ii) moving-film and (iii) stagnant-film between the dispersed phase and the capillary wall. Figure 5.6 illustrates the arrangement of a droplet in Taylor flow with the velocity profile highlighted for three states of (a) no-film, (b) moving-film and (c) stagnant-film.

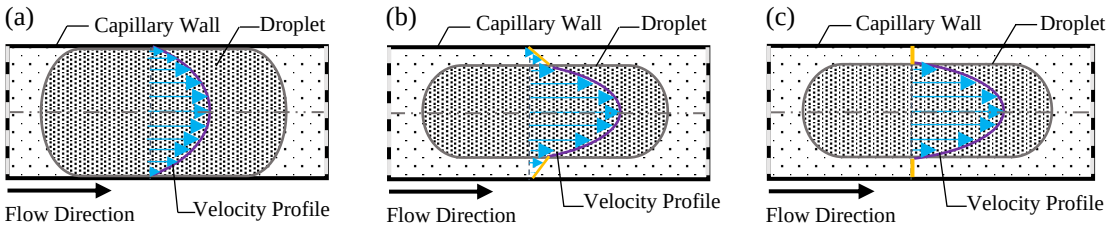

Figure 5.6. Schematic of the velocity profile across the capillary by assuming (a) no-film, (b) moving-film and (c) stagnant-film.

In a study by Kashid and Agar (2007), an expression was developed to estimate the interfacial contribution from the Young–Laplace equation by assuming no-film. This approach was found to overestimate the pressure drop in most cases (Lee and Lee 2010; Jovanović *et al.* 2011; Mac Giolla Eain *et al.* 2015). This is due to the existence of a thin liquid barrier between the droplets and the capillary wall (Howard and Walsh 2013; Mac Giolla Eain *et al.* 2013a) which significantly affects the pressure drop along the droplet. Also, the actual contact angle values of the droplets greatly diverge from the dry wall case (Figure 5.6(a)), and this results in an inaccurate estimation of the interfacial contribution determined from the Young–Laplace equation. Thus, in the following sections, the experimental data will be compared with the most well-known and recent models which assume either a stagnant or a moving film. This aids in identifying the limitations with the existing models in an effort to improve these models through a comprehensive data analysis.

5.3.1. Moving-Film Model

In the moving-film model (Jovanović *et al.* 2011) as shown in Eq. 5.2, total pressure drop can be significantly affected by film thickness. The shear stress and velocity are assumed continuous across the interfaces whereas the capillary wall is conditioned to a no-slip boundary.

$$\left(\frac{\Delta P_D}{L}\right)_{moving-film} = \frac{4U_D\varepsilon}{\frac{(R^2-(R-h)^2)}{\mu_C}+\frac{(0.5(R-h)^2)}{\mu_D}} \tag{5.2}$$

Where μ_C, ε, R, μ_D, U_D, h, and L refer to carrier viscosity, droplet length fraction ($\varepsilon = L_D/L_u$), capillary radius, droplet viscosity, droplet velocity, film thickness, capillary length.

In an initial effort, Jovanović *et al.* (2011) proposed a model in which the dispersed phase contribution was determined by employing the moving-film model (Eq. 5.2). In this model, the contribution of the interfacial pressure drop is calculated using Bretherton's equation, which was obtained by analysing the curvature of leading/trailing caps of a Taylor flow bubble. The determined contribution of each parameter in this model is presented in Table 5.4, where L_u, γ, and Ca_C are slug unit length ($L_u = L_D + L_C$), interfacial tension between respective phases and the Capillary number based on the carrier phase properties, respectively.

Table 5.4. Contribution of each parameter in a proposed model by Jovanović *et al*. (2011) by assuming moving-film around the dispersed phase.

Carrier phase (ΔP_C)	$L\frac{8\mu_C U(1-\varepsilon)}{R^2}$, (Hagen − Poiseuille)
Dispersed phase (ΔP_D)	$L\frac{4U_D\varepsilon}{\frac{(R^2-(R-h)^2)}{\mu_C}+\frac{(0.5(R-h)^2)}{\mu_D}}$, (moving − film)
Interfacial tension (ΔP_{Int})	$\frac{L}{L_u}7.16(3Ca_C)^{2/3}\frac{\gamma}{D}$, (Bretherton's equation)

In Figure 5.7, experimental pressure drop measurements are compared with the moving-film model. This plot shows the sum of the viscous pressure drop along the dispersed phase and the interfacial contribution, by subtracting the carrier phase contribution from the total pressure drop. This allows for a more accurate and informative evaluation of the model by only focusing on the additional pressure drop caused by introducing the secondary phase into the system.

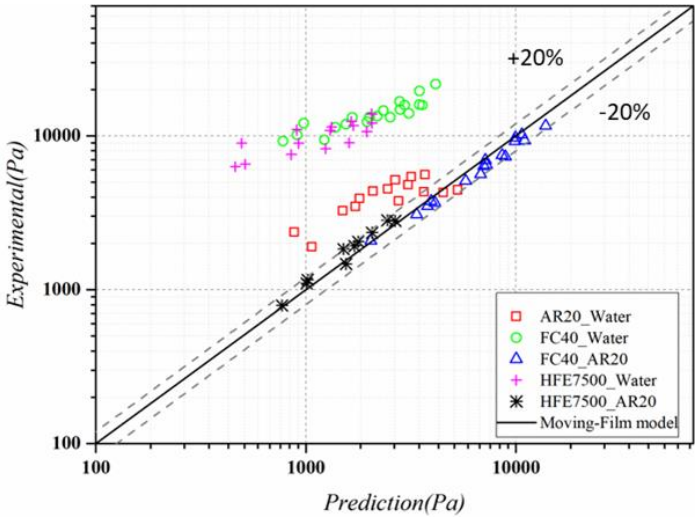

Figure 5.7. Experimental pressure drop caused by the secondary phase (viscous and interfacial contributions, $\Delta P_D + \Delta P_{Int}$) is plotted against theoretical prediction calculated using moving-film model described by Eq. 5.2.

From Figure 5.7, it is evident that results from HFE7500-water, FC40-water and AR20-water experiments are significantly underpredicted by the moving-film model while the majority of the data points from FC40_AR20 and HFE7500_AR20 are well predicted within a $\pm 20\%$ percent bandwidth error (shown by dashed lines). Underestimation of the pressure drop by this model has also been pointed out by Mac Giolla Eain *et al.* (2015) for similar fluid combinations of HFE7500_Water, FC40_Water, and AR20_Water. A poor agreement in these cases can be explained by the procedures taken to develop the pressure drop terms. As previously stated, the moving film model uses Bretherton's theoretical solution to calculate the interfacial pressure drop while assuming no inertial influence. However, numerous numerical and experimental investigations have shown the effect of inertial forces on the flow pattern around the dispersed phase and, consequentially, on the interfacial pressure drop (Heil 2001; Fujioka and Grotberg 2005; Kreutzer *et al.* 2005b; Walsh *et al.* 2009). The pressure drop across a droplet is mainly governed by the Laplace pressure term which is regulated by the droplet's shape, and according to various studies (Giavedoni and Saita 1999; Hodges *et al.* 2004; Kreutzer *et al.* 2005b) inertia has a substantial impact on shape. As a result, inertia is expected to play a significant role in the interfacial pressure drop of liquid–liquid Taylor flows.

Table 5.5 provides the contribution of each component (ΔP_C, ΔP_D and ΔP_{Int}) to the total pressure drop (ΔP_T) for the moving-film model. As shown, FC40-AR20 and HFE7500-AR20 flows have the minimum contributions of the interfacial tension due to the

lowest interfacial tensions of 0.0061 and 0.0019 respectively. Hence, the moving-film model is better positioned to predict pressure drop in these cases. This brings to light the weakness of the model in correctly assessing the interfacial pressure drop contribution. According to Table 5.5, the contribution of interfacial pressure drop for AR20-Water ranges between 8% and 17% while, in experiments with HFE7500-water and FC40-water, the contribution ranges from 21% to 36% and from 24% to 38% respectively. Thus, the results from AR20-water are more likely to agree with the model since the contribution of interfacial pressure drop is smaller.

Table 5.5. Contribution of each component (ΔP_C, ΔP_D and ΔP_{Int}) to overall pressure drop determined by moving-film (Jovanović et al. 2011)model for all tested flow combinations.

	ΔP_C%	ΔP_D%	ΔP_{Int}%
AR20_Water	79-89	1-10	8-17
FC40_Water	49-61	6-27	24-38
HFE7500_Water	35-47	19-45	21-36
FC40_AR20	21-49	37-74	5-14
HFE7500_AR20	27-48	41-64	8-13

In order to provide a better assessment, in Figure 5.8, the experimental interfacial pressure drop is compared with Bretherton's model. The experimental contribution of the interfaces is determined by using the Hagen-Poiseuille and moving-film equations to subtract the carrier's and the droplet's respective viscous pressure drops from the total experimental value. Clearly, the model is unable to collapse the data within the 20% error bands, and the majority of the data points are significantly scattered beyond the model's range. This poor agreement indicates that other critical factors need to be considered in liquid-liquid flows in order to correctly estimate the interfacial pressure drop. As previously stated, in liquid-gas flows, the additional pressure drop imposed by the secondary flow is assigned to the interfaces, and the viscous pressure drop along the dispersed phase is disregarded due to the negligible viscosity of the gas. This makes it simpler to develop a model to correlate the contribution of the interfacial pressure drop. However, in liquid-liquid flows, the extra pressure drop induced by the segmented phase is a comparable value to that of the viscous and interfacial pressure drops and differentiating the contribution of each component is a more difficult challenge. For instance, it is not clear whether the poor agreement in Figure 5.8 results from the inability of the Bretherton's model to determine the interfacial contribution or from the use of the moving-film model to estimate the viscous

pressure drop along the droplet. Therefore, a trustworthy model must first account for the viscous pressure drop along the droplet in order to achieve an authentic correlation to estimate the interfacial contribution. In the following subsection, results are compared to models by Jovanović *et al.* (2011) and Mac Giolla Eain *et al.* (2013b) which assume a stationary film between the droplet and the capillary wall. This aids in finding a more effective model to estimate the interfacial contribution by selecting the model that is more accurate at estimating the viscous pressure drop along the droplet.

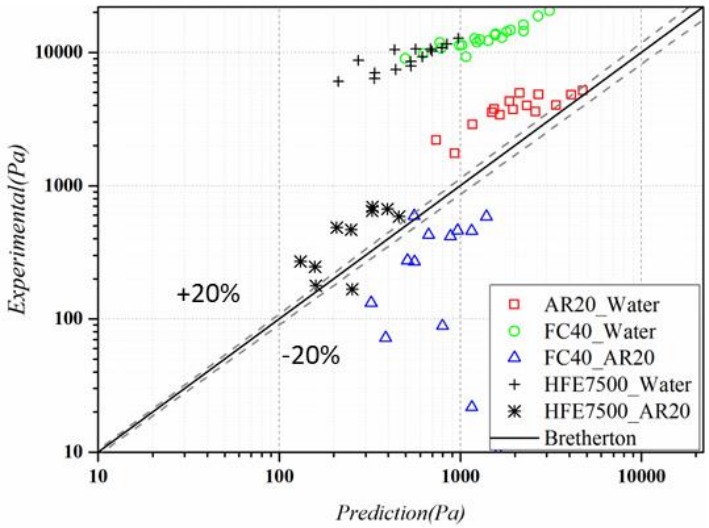

Figure 5.8. Determined experimental interfacial pressure drop plotted against theoretical solution by Bretherton by assuming moving-film around the segmented phase ($\Delta P_{Int_{exp}} = \Delta P_{exp} - \Delta P_C - (\Delta P_D)_{moving-film}$).

5.3.2. Stagnant-Film Model

In the stagnant-film model, a stationary film is assumed between the dispersed slug and the capillary wall. In this modelling procedure, the immobile film reduces the radius of the channel that the droplet is traveling through (see Figure 5.6(c)). Equation 5.3 presents the stagnant-film model where the dispersed phase viscous pressure drop is obtained by Hagen-Poiseuille flow theory. The capability of this modelling technique in predicting the pressure along the dispersed phase has also been examined in a study by Jovanović *et al.* (2011). In this study, similar to the moving-film model, Hagen-Poiseuille and Bretherton equations were used to predict the carrier phase contribution, and differential Laplace pressures between leading and trailing caps respectively.

$$\left(\frac{\Delta P_D}{L}\right)_{stagnant-film} = \frac{8\mu_D U_D \varepsilon}{(R-h)^2} \tag{5.3}$$

In Figure 5.9, the additional pressure drop induced by the secondary phase is compared with the stagnant-film model. For AR20-water, FC40-water and HFE7500-water the stagnant-film model underpredicts the pressure drop, similar to the moving-film model in Figure 5.7. This similarity has also been pointed out by Jovanović with a relative difference of less than 1.4% noted between both models. However, unlike the moving-film model which exhibits good agreement for FC40-AR20 and HFE7500-AR20 with very low viscosity ratios (less than unity), the stagnant-film model significantly overestimates the results in these cases.

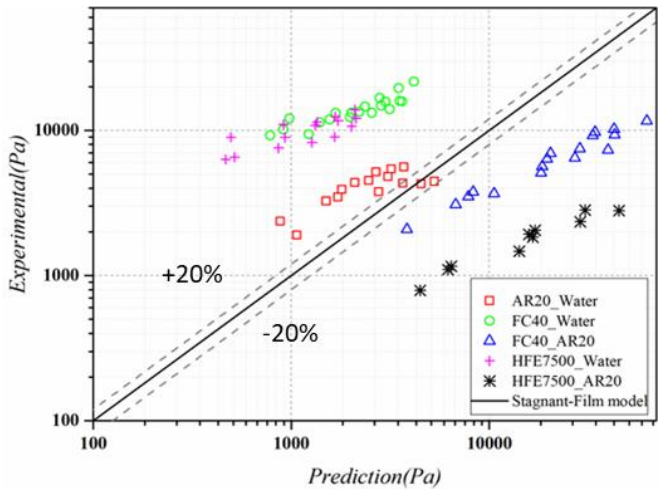

Figure 5.9. Experimental pressure drop caused by the secondary phase (viscous and interfacial contributions, $\Delta P_D + \Delta P_{Int}$) is plotted against theoretical prediction calculated using stagnant-film model described by Eq. 5.3.

The stagnant-film model was developed by assuming immobile flow within the film that encapsulates the droplet. However, this simplified assumption is not reliable in all cases. Figure 5.10(a) and 5.10(b) illustrate the velocity profile through the cross-section of a capillary for the tested fluid combinations. The velocity profiles across the film in Figure 5.10(c) are plotted using the expression given in equation 5.4 developed by Howard and Walsh (2013).

$$\frac{U_{film(r)}}{U_{TP}} = \frac{2\left(1-\frac{r^2}{R^2}\right)}{1+\frac{R_D^4}{R^4}\left(\frac{\mu_C}{\mu_D}-1\right)} \tag{5.4}$$

This graph exhibits the flow velocity across the film (U_{film}) on a log-linear scale while being normalized by the mean two-phase flow velocity (U_{TP}).

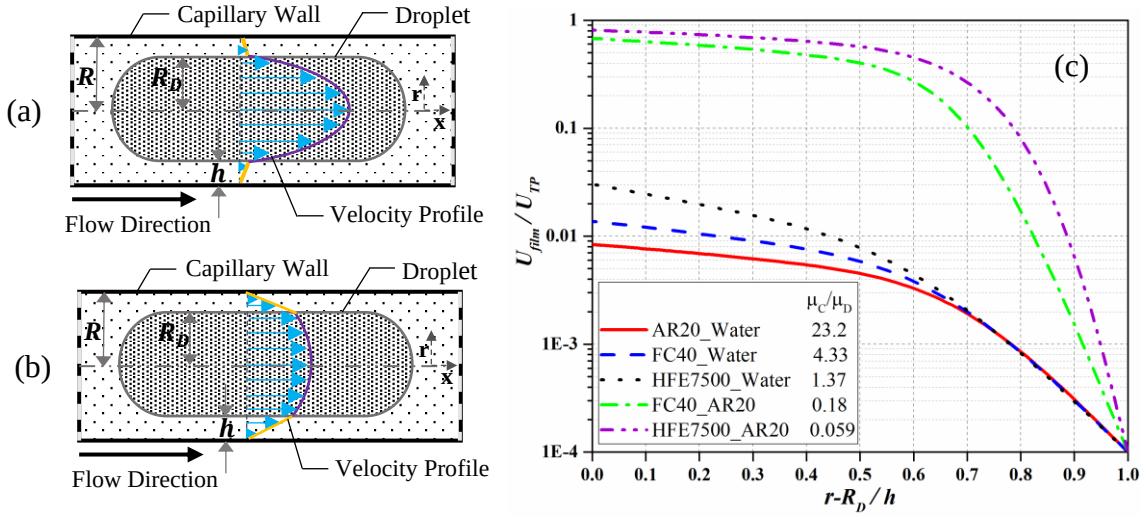

Figure 5.10. Schematic of the velocity profile over the capillary cross section in (a) AR20-water, HFE7500-water and FC40-water, (b) HFE7500-AR20 and FC40-AR20 and (c) comparison of the relative flow velocity across the film for tested flow combinations on log-linear scale.

Figure 5.10(c) indicates that the flow within the film moves faster as viscosity ratio decreases. In this graph, HFE7500-AR20 and FC40-AR20 flows with viscosity ratios of 0.18 and 0.059 respectively, show a considerable flow within the film. While, in the other cases, AR20-water, FC40-water and HFE7500-water the flow velocity within the film is almost negligible. In addition, HFE7500-AR20 and FC40-AR20 develop a relatively thicker film in comparison to the other fluid combinations. In Figure 5.11(a) film thickness ratio is plotted against flow velocity for each liquid-liquid combination. The film thickness magnitudes along the dispersed phase (between the front and rear slug caps) have been determined by employing a model developed by Mac Giolla Eain *et al.* (2013a) for liquid-liquid slug flow regimes. According to this model, the film thickness increases with velocity as the Capillary and Weber numbers increase.

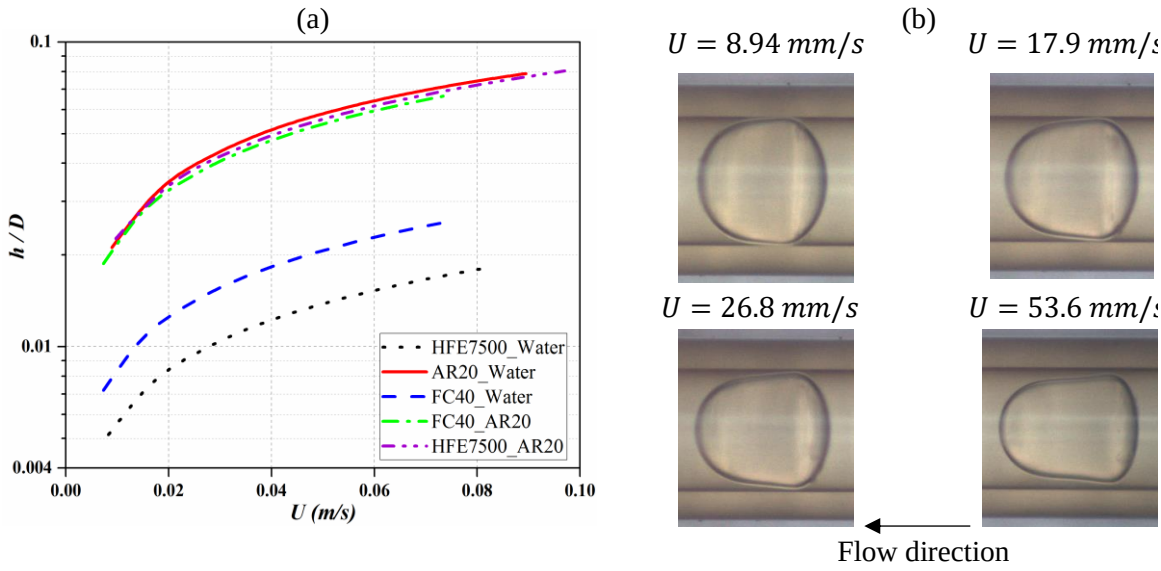

Figure 5.11. (a) Effect of flow velocity on film thickness values and (b) images of water dispersed in AR20 over varying velocity but constant droplet volume.

Figure 5.11(b) presents images of a single water droplet dispersed in the AR20 while moving at different velocities. Images were captured using a high-speed camera and the variation in droplet volume between images is less than 2%. At a higher flow velocity, the droplet becomes more elongated and a thicker film thickness is present. Hence, a thicker film (see Figure 5.11(a)) and a higher velocity of the fluid within the film (see Figure 5.10(c)) undermine validity of the stagnant-film model for FC40-AR20 and HFE7500-AR20 flows. In addition, for flows with low interfacial tension values, the impact of interfacial pressure on total pressure drop becomes weak and the remaining terms (the dispersed and carrier phase viscous pressure drop) dominate. Therefore, even a small miscalculation of the contribution of dispersed phase can have a significant effect on the overall predicted value of the pressure drop in these cases. Table 5.6 provides the contribution of each component to the total pressure drop for the stagnant-film model. According to this table, the contribution of dispersed phase to the total pressure drop is considerably high in FC40-AR20 and HFE7500-AR20, up to 96%.

Table 5.6. Contribution of each component (ΔP_C, ΔP_D and ΔP_{Int}) to overall pressure drop determined by stagnant-film model for all tested flow combinations.

	ΔP_C%	ΔP_D%	ΔP_{Int}%
AR20_Water	79-88	1-10	9-17
FC40_Water	49-61	5-28	23-39
HFE7500_Water	34-47	20-46	20-36
FC40_AR20	7-34	56-91	2-10
HFE7500_AR20	3-10	87-96	1-3

For AR20-water flows, the results in Figure 5.9 show that this case has a better agreement with the model than HFE7500-water and FC40-water. This can be due to a greater contribution of the viscous carrier phase to total pressure drop (79-88%), which reduces the contributions of the dispersed phase and interfacial tension (see Table 5.6).

In Figure 5.12 the interfacial pressure drop contribution is determined using the stagnant-film model (Jovanović *et al.* 2011). This graph illustrates incorrectly, negative interfacial pressure drop values for FC40-AR20 and HFE7500-AR20 when using the stagnant-film model to estimate the viscous pressure drop along the droplet. Therefore, assuming a stagnant-film to evaluate the dispersed phase contribution may not yield a valid result for flows with viscous dispersed phase, $\mu_C/\mu_D < 1$.

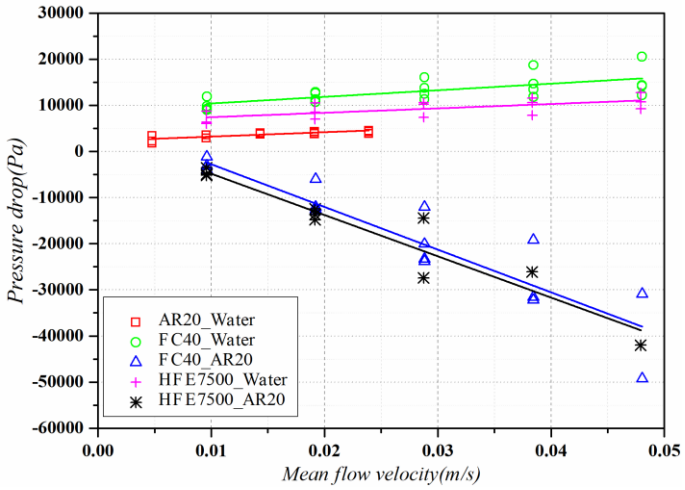

Figure 5.12. Experimental interfacial pressure drop by assuming a stagnant-film around the dispersed phase ($\Delta P_{Int_{exp}} = \Delta P_{exp} - \Delta P_C - (\Delta P_D)_{stagnant-film}$). The linear best fit line is depicted as a solid line for each flow combination.

5.3.3. Skin-Friction Model

By employing a semi-empirical approach to the subject and a different technique than the differential Laplace pressure, Mac Giolla Eain *et al.* (2013b) developed a new model focused on the contribution of interfacial pressure drop to overall pressure drop in liquid-liquid Taylor flows. The friction factor-Reynolds number (fRe) product was applied to the problem by employing single phase theory in predicting pressure drop in both phases and assuming a stagnant-film around the segmented phase. The pressure drop is stated as follows:

$$\Delta P = 4\left(f_{app}Re\right)x^{+}(0.5\rho U^{2}) \tag{5.5}$$

f_{app} is the apparent friction factor and gives the average friction factor over a desired area. Equation 5.5 presents the empirical correlation by Du Plessis and Collins (1992) that was used to estimate the apparent friction factor-Reynolds number product in both carrier and dispersed phase.

$$f_{app}Re = 16\left(1 + \left(\frac{0.046}{x^{+}}\right)^{1.1}\right)^{0.46} \tag{5.6}$$

In this equation x^{+} is the dimensionless development length for laminar flows in straight channels which is defined as:

$$x^{+} = \frac{l}{D\ Re} \tag{5.7}$$

where l and D are the slug length and channel diameter respectively.

Assuming the exact approximation of Equation 5.5 in obtaining the pressure drop in both phases, the interfacial pressure drop is calculated by subtracting the oil and water pressure drops from the total experimentally measured pressure drop. Mac Giolla Eain *et al.* (2013b) state the interfacial pressure drop in the form of a dimensionless skin-friction factor (C_f) presented in the following equation.

$$C_f = 14.486[(L_D^{*\,0.65}) \times (Ca_C^{-0.616}) \times (Re_C^{-1.05})] \tag{5.8}$$

In this equation, the skin-friction coefficient is determined to be a function of dimensionless droplet length $\left(L_D^* = {}^{L_D}/_{D}\right)$, Capillary and Reynolds numbers, where subscripts C and D refer to the carrier and dispersed phases respectively. This scaling group correlates the interfacial pressure drop and was achieved by a regression analysis of the data.

Figure 5.13 presents a comparison between current experimental data and the skin-friction model. In experiments with fluid combinations in which the carrier phase is more viscous than the dispersed phase ($\mu_C > \mu_D$), the model exhibits a good agreement with FC40-water and HFE7500-water but overestimates for flows with AR20_water. In flows with FC40-AR20 and HFE7500-AR20 at very small carrier to dispersed viscosity ratios ($\mu_C < \mu_D$), the correlation presents a greater overestimation.

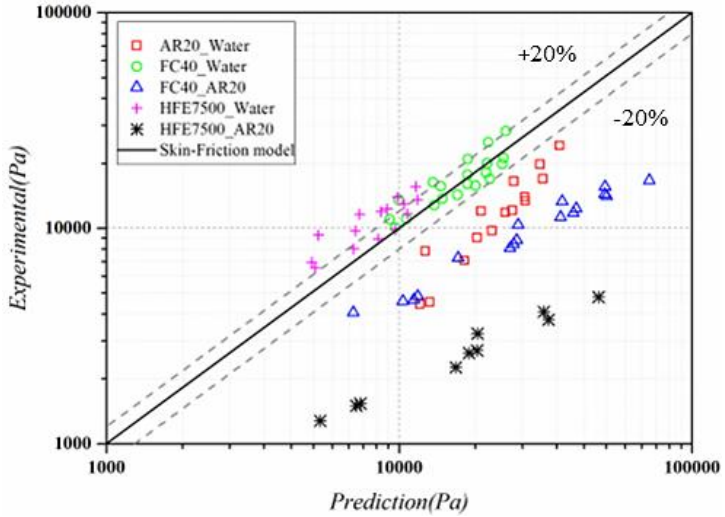

Figure 5.13. Experimental total pressure drop plotted against theoretical prediction calculated using skin-friction model.

In this model, the contribution of the interfaces towards total pressure drop was determined by assuming the presence of a stagnant-film between the capillary wall and the droplet. However, as shown in Section 5.3.2, this assumption can lead to incorrect values for cases involving significant film thickness and flow velocity within the film. FC40-water and HFE7500-water flows have a lower film thickness and negligible flow within the film (see Figure 5.10 and 5.11) and hence show good agreement with the model with the majority of data points are located within 20% bandwidths error. According to Table 5.7, in experiments with FC40-AR20 and HFE7500-AR20, the contribution of the dispersed phase to the overall pressure drop becomes more significant due to a higher droplet

viscosity and a reduced contribution of interfacial pressure drop (caused by lower interfacial tension). Therefore, the incorrect assumption of a stagnant-film can result in considerable divergence from the model in these cases. This can explain the significant overestimation by the model in case of HFE7500-AR20 where reports the maximum flow velocity within the film and a significant film thickness.

Table 5.7. Contribution of each component (ΔP_C, ΔP_D and ΔP_{Int}) to the overall pressure drop determined by the skin-friction model for all tested flow combinations.

	ΔP_C%	ΔP_D%	ΔP_{Int}%
AR20_Water	18-55	1-4	43-81
FC40_Water	8-28	2-8	67-89
HFE7500_Water	5-15	4-13	75-90
FC40_AR20	7-28	47-85	8-25
HFE7500_AR20	3-9	81-93	2-11

5.4. Discussion

According to the previous section, none of the discussed models can fully collapse the experimentally measured pressure drop data for the current study within a 20% bandwidth error. As a result, they cannot be effectively applied in the design of the majority of systems that adopt liquid-liquid Taylor flow regimes. It was shown in Section 5.3.2 that the experimental data deviate more from the stagnant-film model which assumes an immobile film around the droplet. This model is restricted to cases with negligible flow in the film thickness and, as film thickness and flow velocity within the film increase, the experimental data becomes considerably divergent from the prediction. Similar to the stagnant-film model, the disagreement of the experimental data with the skin-friction model was shown to be attributed to the incorrect assumption of a stationary film which led to an incorrect estimation of the dispersed phase contribution. Although, the moving-film model presented a better estimation than the stagnant-film model, it was still limited to certain test conditions. According to the data analysis, this was due to the incorrect estimation of the contribution of interfacial pressure drop and by decreasing the contribution of the interfacial pressure, the model better agrees with the experimental data. The expression utilized by the moving-film model to determine the interfacial pressure drop is restricted to conditions with very thin liquid films and negligible inertial effects and mainly suitable for liquid-gas flows.

Hence, based on the analysis of the strengths and weaknesses of the existing models, a new correlation is suggested by the current authors to better predict the interfacial pressure drop in liquid-liquid Taylor flow regimes. It is assumed that there is a moving-film surrounding the droplet and that the carrier phase has fully developed laminar flow. The new correlation is given in Eq. 5.9. The power trend law of the correlation is determined by means of data regression with the objective of finding the minimum RMS error achieved by means of iterative numeric procedures. An analogous method to that of Equation 4.4 is employed to determine the optimal values for target variables while adhering to specific constraints.

$$\Delta P_{Int} = \frac{2}{3}\left(\frac{\gamma}{D}\right) Ca^{2/3}\, {Re_C}^{4/5}\, {We_D}^{-1/2} \left(\frac{\mu_C}{\mu_D}\right)^{1/3} \left(\frac{L_D}{D}\right)^{2/5} \tag{5.9}$$

Ca, Re_C and We_D are the Capillary number (based on droplet velocity and the carrier phase viscosity), Reynolds number (based on the carrier phase properties and characteristics), and Weber number (based on the dispersed phase properties and characteristics) respectively.

Figure 5.14 (a) and 5.14 (b) illustrate an evaluation of the new model for the interfacial (ΔP_{Int}) and secondary phase ($\Delta P_D + \Delta P_{Int}$) contributions respectively; where the vertical axis represent results from experiments and the horizontal axis is the model's estimation of the pressure drop.

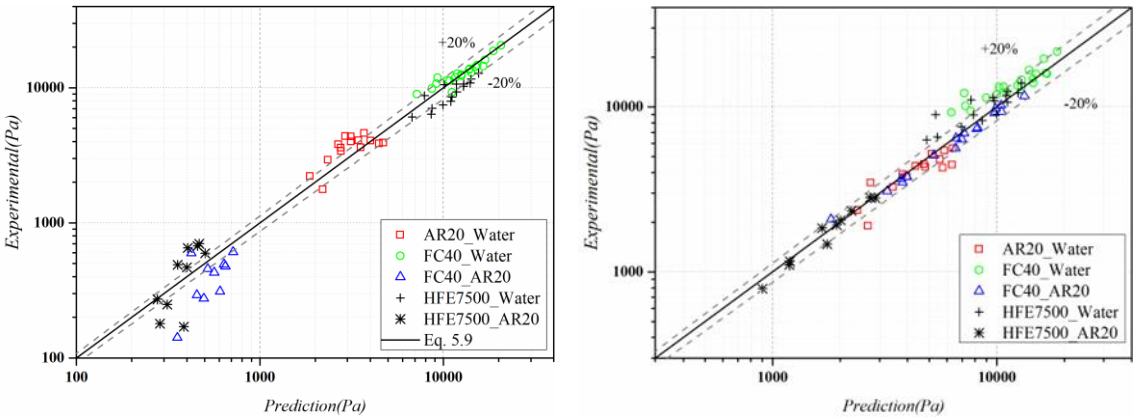

Figure 5.14. Experimental pressure drop caused by (a) the interfacial tension between the fluids (ΔP_{Int}) and (b) secondary phase ($\Delta P_D + \Delta P_{Int}$), plotted against theoretical prediction determined using Eq. 5.9 and assuming a moving-film around the droplet.

From Figure 5.14, it can be clearly seen that majority of the data points are located within the $\pm 20\%$ bandwidth of the predicted values and the model shows good capability in estimating pressure drop in liquid-liquid slug flow regimes over the tested flow conditions. The hydrodynamic pressure drop along the droplet is determined by the analytical laminar flow solution to co-flowing immiscible streams with shear stress conserved across the interface. It was observed during the current investigation that assuming a stagnant-film led to significant discrepancies, thus it was decided to investigate the pressure drop using the assumption of a moving-film. The annular flow model is shown to provide a good prediction for liquid-liquid flows (see Figure 5.14(b)) where the droplet viscosity is significant and the pressure gradient in the viscous film grows with the droplet viscosity (Lac and Sherwood 2009). While, in flows with a very low viscosity of droplet (similar to liquid-gas flows), fluid in the film is almost stagnant and the end caps are the only drivers of pressure drop (Bretherton 1961).

The $Ca^{2/3}$ scaling law, in Eq. 5.9, is similar to that proposed by the pioneer research by Bretherton (1961) who employed a lubricant analysis over the transition region (which is located between the spherical front of the bubble and the flat film region) to determine the interfacial pressure drop of a bubble. Numerous numerical investigations, in which ideal conditions of surfactant-free fluid were assumed, have proved the validity of Bretherton's theory (Reinelt 1987; Ratulowski and Chang 1989; Edvinsson and Irandoust 1996; Heil 2001). Most of these investigations have ignored inertial effects by assuming $We \ll 1$. The influence of inertia on Bretherton's approach has been more thoroughly examined in a number of studies (Edvinsson and Irandoust 1996; Giavedoni and Saita 1997; Aussillous and Quéré 2000). According to these studies, inertia significantly affects the bubble's shape. As the Laplace pressure term is mostly driven by the bubble's shape, the inertial forces are then expected to play an important role in determining the pressure drop across a single bubble. Therefore, the inertial effects are included in the correlation (Eq. 5.9) by involving the Weber and Reynolds numbers. In the current study, Reynolds and Weber numbers encompass a wide range of magnitude, ranging from 0.1 to 49 and 7×10^{-4} to 1.5, respectively.

The viscosity ratio is also included in determining the interfacial pressure drop since several numerical and experimental studies have shown the effect of viscosity ratio on the pressure drop (Lac and Sherwood 2009; Gupta *et al.* 2013; Mac Giolla Eain *et al.* 2015). A numerical study by Lac and Sherwood (2009) shows that in cases with high-viscous

droplets, the Capillary number and the viscosity ratio both affect the pressure drop. Also, according to this study, high-viscosity drops are subjected to increased shear stress, causing them to deform more than low-viscosity drops. Images of single droplets from the current experiments with HFE7500-AR20 and HFE7500-water are shown in Figure 5.15(a) and (b) respectively. These images are taken for droplets with a similar volume moving with a same flow velocity.

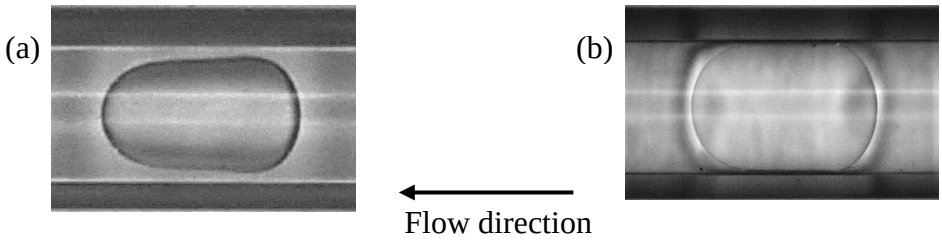

Figure 5.15. Images of single droplets of (a) AR20 and (b) water dispersed in HFE7500 for the same flow velocity and droplet volume.

As shown in these figures, the AR20 droplet, with its higher viscosity, exhibits more shape distortion than the water droplet. Considering the droplet shape as one of the main parameters in determining the Laplace pressure, the interfacial pressure drop is expected to be influenced by the viscosity ratio. Furthermore, viscosity ratio has been shown to have a significant impact on the internal topology of slugs and subsequently the stresses associated with the internal recirculation in droplets (Hodges *et al.* 2004). Overall, the viscosity ratio of the involved phases is expected to affect the pressure drop in liquid-liquid flows with a wide range of viscosity ratios; whereas in liquid-gas flows, the negligible viscosity of the gas phase always results in very high carrier to dispersed viscosity ratios.

Figure 5.16 represents a comparison between the total measured experimental pressure drop and the theoretical value calculated using single-phase flow theory and the moving-film model to predict the pressure drop across the carrier and dispersed phases respectively, while using Eq. 5.9 to predict the interfacial pressure drop. From this figure, it can be clearly seen that majority of the data points are located within the $\pm 20\%$ bandwidth of the predicted values and the model shows an excellent capability of estimating pressure drop in liquid-liquid slug flow regimes over the tested flow conditions. Moreover, the model presents a noticeable degree of accuracy in cases with the lowest carrier to dispersed viscosity ratios, FC40-AR20 and HFE7500-AR20, with the majority of the data points closely clustered around the predicted values indicated by a solid line. This

indicates the model's significant ability to estimate the pressure drop in liquid-liquid slug flows with extremely high dispersed phase viscosity.

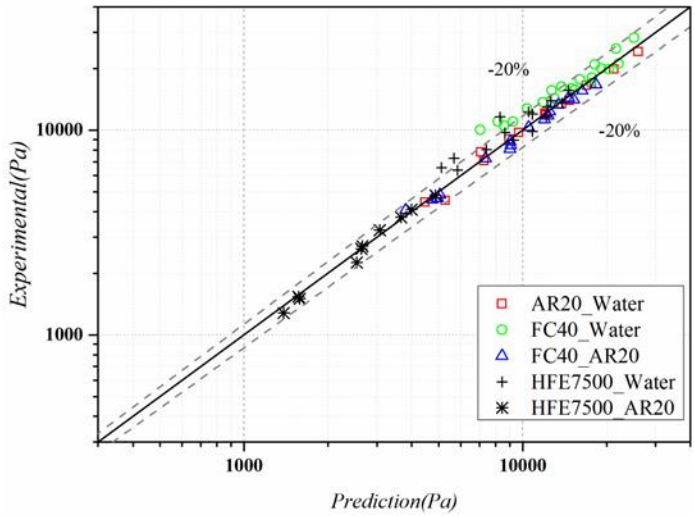

Figure 5.16. Total measured experimental pressure drop plotted against theoretically predicted pressure with Eq. 5.9 used to estimate the interfacial pressure drop contribution.

5.5. Conclusions

Pressure drop in liquid-liquid Taylor flow regimes was investigated experimentally by means of a novel experimental set up that ensured high measurement accuracy and repeatability. Results were compared with the most acceptable models in the literature and the accuracy of the existing models was shown to be limited to certain test conditions. Data analysis revealed that inaccurate estimation of pressure drop is attributed to the procedures and assumptions taken to develop the models. It was observed that the deviation of experimental data from the stagnant-film model is attributed to the restricted applicability of this model to cases with negligible flow within the film thickness. As film thickness and flow velocity within the film increase, experimental data diverges considerably from the prediction. Similarly, the skin-friction model assumes a stationary film, leading to an incorrect estimation of dispersed phase contribution. Although, the moving-film model offered a better prediction, it was still constrained by specific testing conditions. The expression employed by the moving-film model to determine the interfacial pressure drop is primarily applicable to scenarios involving liquid-gas flows with very thin liquid films and negligible inertial effects.

Conducting experiments over a wide-range of flow conditions allowed a thorough analysis of the existing models and resulted in a new expression to better estimate the interfacial pressure drop in liquid-liquid Taylor flow regimes. The new model is achieved by assuming an annular velocity profile across the capillary in the presence of the second phase and considering inertial viscosity ratio effects in determining the pressure drop. This model offers an appropriate prediction tool for most applications that utilize liquid–liquid slug flows, by fitting the experimental data to within $\pm 20\%$.

Chapter 6

Conclusions and Recommendations

This thesis investigated the fundamental hydrodynamics of liquid-liquid slug flows confined to mini and micro scale capillaries. The influential parameters on droplet velocity and pressure drop were identified, and phenomenological models were developed as a result. These models contribute to the advancement of microfluidic devices incorporating liquid-liquid Taylor flows and offer a greater insight to this flow regime by identifying the limitations with previous models. To accomplish the objectives, a novel non-invasive and cost-efficient measurement technique was developed and successfully applied. With high accuracy and reliability, this experimental setup allowed for flow investigation under a variety of operational and geometrical parameters. The current chapter includes the key findings from the entire body of the research, as well as providing recommendations for future studies.

6.1. Conclusions

The following three sub-sections summarize the main conclusions of this thesis. The first sub-section includes the developed measurement technique for performing high frequency real-time measurements of slug flow characteristics flowing in a transparent microfluidic channel. The findings of hydrodynamic research pertaining to the droplet velocity and the pressure drop of liquid-liquid slug flows are then presented in the subsequent sections.

6.1.1. Measurement Technique for Slug Flow Characteristics

The current study presented a novel measurement technique for investigating flow properties in both liquid-liquid and liquid-gas slug flow regimes. This automated, non-intrusive measurement technique allows for an in-line high-frequency droplet/bubble detection and related physical properties. The automation of droplet recognition and related physical features such as droplet length and velocity, are based on the difference in light transmission through a tube caused by phase shifting in liquid-liquid or liquid-gas flows.

In this regard, a reliable light source that delivers a steady amount of light orthogonal to the length-axis of the tubing, as well as a sensor sensitive to light intensity, are required to identify the fluctuation in transmitted light caused by phase shifting. The analogy of a sideward exposed hemispherical lens, which bundles or scatters light depending on the position of the light beam, was then employed to post-process the output signal from the light sensor. This measurement technique can be used for fast in-situ experimental modifications due to its real-time nature. The contrast in index of refraction that enables the phase detection, suggests that this detector might also serve as a preliminary step for probing the chemical composition of droplets. Additionally, this methodology enables a cheap and reliable framework to determine the inner diameter of microchannels with a high precision.

6.1.2. Mobility of Droplets in Liquid-Liquid Taylor Flows

This research developed a novel correlation to improve the description of the instantaneous droplet velocity. This model can be used to better estimate the velocity of elongated droplets and can serve as a foundation to better characterize the flow hydrodynamics. In addition, key insights were offered to help with the optimization of microfluidic devices by describing the influential parameters that impact droplet velocity. Transportation, analysis, detection, and monitoring are among the procedures applied in biological or chemical applications, each needing precise spatial and time control data for droplets. The main findings from the study on droplet velocity are listed below:

- Results indicate a complex dependency of droplet velocity on various parameters including droplet length, viscosity ratio, Reynolds and Bond number.
- For very short droplets, $L_D/D \lesssim 2$, the diameter of the droplet is noticeably smaller than that of the capillary and the ratio of capillary to buoyancy forces greatly impacts the droplet velocity. When capillary forces dominate, decreasing the droplet length boosts droplet mobility, whereas short droplets travel substantially slower than the mean flow velocity when buoyancy forces are dominant.
- For $L_D/D \gtrsim 2$, the analysis showed a changeover zone in which the droplet velocity first decreases and then increases. This crossover area deepens as the carrier to droplet viscosity ratio (μ_C/μ_D) increases. The lack of well-formed internal circulations is believed to be the reason for velocity reduction in this region with the effect becoming stronger as the carrier to droplet viscosity ratio increases. In

addition to the internal flow topology, the buoyancy force is shown to influence the droplet velocity in this zone.

- As the droplet length exceeds the crossover zone, the droplet velocity becomes almost constant and droplet length no longer affects the drop velocity. According to the data analysis, the commencement of this plateau zone greatly depends on the Capillary number and weakly on Reynolds and Bond numbers. An expression was developed to estimate the minimum droplet length ratio ($\frac{L_D}{D}$) required to enter the plateau zone for each flow combination. This model was able to collapse the data within $\pm 20\%$ bandwidth errors. It is recommended to use droplets longer than this minimal threshold to avoid coalescence of adjoining drops in applications where droplet coalescence is an undesired phenomenon (e.g. DNA analysis and protein crystallisation).
- As the droplet length surpasses a certain value, the droplet velocity ratio (U_D/U_{mean}) becomes independent from its length and increases as the Capillary number increases. This increase was found to be correlated as a function of Capillary number with a scale of $Ca^{0.5}$. A new correlation was suggested in this study to better predict the velocity of elongated droplet in liquid-liquid Taylor flow regimes. This model was achieved by means of a linear data regression and includes the effects of Bond and Reynolds numbers. The model showed an excellent capability of estimating droplet velocity with majority of the data points being located within the $\pm 10\%$ bandwidth of the predicted values.

6. 1. 3. Pressure Drop of Liquid-Liquid Taylor Flows

Pressure drop in liquid-liquid Taylor flow regimes was investigated experimentally by means of a novel experimental set up that ensured high measurement accuracy and repeatability. This investigation aimed to assess the precision of earlier analytical and experimental pressure drop models on liquid-liquid Taylor flows and, if necessary, to establish a more reliable correlation. In this regard, results were compared to the most acceptable models available in the literature and, the strengths and weaknesses of these models were noted. It was discovered that each model's accuracy was constrained to a subset of test conditions, narrow ranges of Reynolds, Capillary and Weber numbers, and were insufficiently accurate over a wide range of viscosity ratios. The current study developed a new expression for interfacial pressure drop based on experimental

investigations over a wide range of Capillary ($3 \times 10^{-4} \leq Ca_C \leq 7.6 \times 10^{-2}$), Reynolds ($0.1 \leq Re_C \leq 49$) and Weber ($7 \times 10^{-4} \leq We \leq 1.5$) numbers while carrier to dispersed viscosity ratio (μ_C/μ_D) spanned from 0.058 to 24.2. The conclusions from this analysis are as follows:

- According to the results, none of the investigated models can fully collapse the experimentally measured pressure drop data within a 20% bandwidth error. As a result, they cannot be effectively applied in the design of systems that adopt liquid-liquid Taylor flow regimes. Data analysis revealed that inaccurate estimation of pressure drop was mainly attributed to the procedures and assumptions taken to develop these models.
- It was shown that the experimental data deviates more from the stagnant-film model which assumes an immobile film around the droplet. This model was restricted to cases with negligible flow in the film and, as film thickness and flow velocity within the film increase, the experimental data becomes considerably divergent from the prediction.
- Similar to the stagnant-film model, the disagreement of the experimental data with the skin-friction model of Mac Giolla Eain *et al.* (2013b) was also shown to be attributed to the incorrect assumption of a stationary film which led to an incorrect estimation of the dispersed phase contribution.
- Although, the moving-film model presented a better estimation than the stagnant-film model, it was still limited to certain test conditions. According to the data analysis, this was due to the incorrect estimation of the contribution of interfacial pressure drop and by decreasing the contribution of the interfacial pressure, the model better agrees with the experimental data. The expression used for determining interfacial pressure drop was restricted to conditions with extremely thin liquid films and minimal inertial effects, primarily for liquid-gas flows.
- A new expression was developed to estimate interfacial pressure drop by assuming an annular velocity profile across the capillary in the presence of the second phase and taking into account inertia and viscosity ratio effects. This model offers an appropriate prediction tool for many applications that utilize liquid–liquid slug flows, by fitting the experimental data to within $\pm 20\%$.

6. 2. Recommendations

There are still unanswered questions and potential research topics concerning the hydrodynamic properties of liquid-liquid Taylor flows in small-scale channels. This section outlines some of the most important recommendations to enhance the current database of results and developed models. It is therefore advised that future research emphasize the following aspects:

- Flows in capillaries of mini and micro scale, ranging from $0.5\ mm$ to $1.6\ mm$, were investigated in this research. However, the size of microfluidic devices is now shrinking to less than $\sim 100\ \mu m$ due to recent advancements in microfabrication technologies. Thus, the ability of the models developed in this research may be evaluated and improved, if necessary, to be used in smaller scale channels with smaller Capillary, Reynolds, Weber and Bond numbers.
- All of the liquids used in this research were free from surfactants. As a result, the Marangoni effects on the established models was not investigated in this research. Surfactants present at the interface between phases tend to achieve an equilibrium state to maintain an equal distribution of molecules. However, when the droplet is in motion, the surfactants are forced towards the rear end of the droplet due to shear stresses. This uneven distribution of surfactants results in a difference in surface tension across the droplet, creating surface tension gradients. This phenomenon has many important applications in various fields, including materials science, biology, and chemistry. For example, it is used in the production of certain types of materials, such as semiconductor devices, and in the development of new drug delivery systems. Therefore, further investigation is required to improve the existing model database and quantitatively assess the significance of surfactants on these flows.
- While there have been significant advances in experimental techniques for studying Taylor flows, numerical modelling remains an important tool for understanding the flow dynamics. Unfortunately, the advantages of Computational Fluid Dynamics (CFD) simulations in understanding the hydrodynamics of Taylor flows have not been harnessed to its full potential. Future research could focus on developing more accurate and efficient numerical models that can capture the complex flow behaviour of Taylor flows. In this regard, a better understanding of internal flow circulations is required to achieve a thorough comprehension of flow

hydrodynamics, which would ultimately result in more accurate simulations. Nowadays, advancements in PIV technology have significantly improved our ability to study and understand fluid flow phenomena in various applications, paving the way for new discoveries and innovations in science and engineering. Thus, it is recommended to carry out visualisation measurements, such as Tomographic-PIV, to reveal the internal flow topology and validate the CFD simulations against the experimental results. Tomographic PIV systems can capture velocity data from multiple camera angles, allowing researchers to reconstruct 3D velocity fields with high resolution and accuracy.

- The geometry of a microchannel can have a significant effect on the hydrodynamics of two-phase flows and understanding these effects is essential for optimizing the design and performance of microfluidic devices and other microscale systems. Two-phase flows in microchannels are influenced by geometrical factors such as channel dimensions and shape. The size and aspect ratio of a microchannel can affect the behaviour of two-phase flow, with smaller channels exhibiting greater interfacial forces and more complex flow patterns. The shape of the microchannel can also affect two-phase flow hydrodynamics, with different flow regimes and interfacial behaviour observed in rectangular, circular, or triangular channels. Therefore, it is advised that the current study's scope be expanded to include capillaries with other cross-sections than circular.

In addition to above outlined recommendations, the scope of this study could be further expanded by investigating the effect of surface roughness and surface properties such as hydrophobicity. Moreover, this study recommends introducing a second liquid phase, in the form of slugs, into boiling flows to detach the vapor bubble at the very beginning of its formation and replace it with a fresh liquid film. The departure diameter in boiling flows, representing bubble size before detachment, significantly influences heat transfer and system performance. Due to the vapor's lower thermal conductivity, smaller departure diameters are preferred to minimize the hot spot zones on the capillary surface in microchannel boiling.

Finally, as the author benefited from the vast knowledge accumulated from the earlier studies, he would be delighted if additional benefits besides the developed models could be used by other researchers for their future studies. Thus, the author encourages other researchers to use the findings and methods from this study as a springboard for their

own investigations, and to support the ongoing pursuit of new discoveries and breakthroughs.

References

Abdollahi, A., Norris, S.E. and Sharma, R.N. (2020a) 'Fluid flow and heat transfer of liquid-liquid Taylor flow in square microchannels', *Applied Thermal Engineering*, 172, 115123.

Abdollahi, A., Norris, S.E. and Sharma, R.N. (2020b) 'Pressure drop and film thickness of liquid-liquid Taylor flow in square microchannels', *International Journal of Heat and Mass Transfer*, 156, 119802.

Abiev, R.S. (2017) 'Analysis of local pressure gradient inversion and form of bubbles in Taylor flow in microchannels', *Chemical Engineering Science*, 174, 403-412.

Adampourezare, M., Dehghan, G., Hasanzadeh, M. and Feizi, M.-A.H. (2021) 'Application of lateral flow and microfluidic bio-assay and biosensing towards identification of DNA-methylation and cancer detection: Recent progress and challenges in biomedicine', *Biomedicine & Pharmacotherapy*, 141, 111845.

Adrugi, W., Muzychka, Y. and Pope, K. (2016) 'Pressure Drop of Liquid-Liquid Taylor Flow in Mini-Scale Tubing', in *ASME International Mechanical Engineering Congress and Exposition*, American Society of Mechanical Engineers, V007T09A046.

Ahn, K., Agresti, J., Chong, H., Marquez, M. and Weitz, D.A. (2006) 'Electrocoalescence of drops synchronized by size-dependent flow in microfluidic channels', *Applied Physics Letters*, 88(26), 264105.

Anna, S.L., Bontoux, N. and Stone, H.A. (2003) 'Formation of dispersions using “flow focusing” in microchannels', *Applied physics letters*, 82(3), 364-366.

Aota, A., Mawatari, K., Takahashi, S., Matsumoto, T., Kanda, K., Anraku, R., Hibara, A., Tokeshi, M. and Kitamori, T. (2009) 'Phase separation of gas–liquid and liquid–liquid microflows in microchips', *Microchimica Acta*, 164(3), 249-255.

Asthana, A., Zinovik, I., Weinmueller, C. and Poulikakos, D. (2011) 'Significant Nusselt number increase in microchannels with a segmented flow of two immiscible liquids: An experimental study', *International Journal of Heat and Mass Transfer*, 54(7-8), 1456-1464.

Aussillous, P. and Quéré, D. (2000) 'Quick deposition of a fluid on the wall of a tube', *Physics of fluids*, 12(10), 2367-2371.

Awad, M. and Muzychka, Y. (2008) 'Effective property models for homogeneous two-phase flows', *Experimental Thermal and Fluid Science*, 33(1), 106-113.

Bandara, T., Cheung, S.C. and Rosengarten, G. (2015) 'Slug flow heat transfer in microchannels: A numerical study', *Computational Thermal Sciences: An International Journal*, 7(1).

Bandhauer, T.M. and Bevis, T.A. (2016) 'High heat flux boiling heat transfer for laser diode arrays', in *International Conference on Nanochannels, Microchannels, and Minichannels*, American Society of Mechanical Engineers, V001T04A002.

Bardin, D., Kendall, M.R., Dayton, P.A. and Lee, A.P. (2013) 'Parallel generation of uniform fine droplets at hundreds of kilohertz in a flow-focusing module', *Biomicrofluidics*, 7(3), 034112.

Baroud, C.N., Gallaire, F. and Dangla, R. (2010) 'Dynamics of microfluidic droplets', *Lab on a Chip*, 10(16), 2032-2045.

Bauer, T., Schubert, M., Lange, R. and Abiev, R.S. (2006) 'Intensification of heterogeneous catalytic gas-fluid interactions in reactors with a multichannel monolithic catalyst', *Russian journal of applied chemistry*, 79(7), 1047-1056.

Berggren, C., Bjarnason, B. and Johansson, G. (2001) 'Capacitive biosensors', *Electroanalysis: An International Journal Devoted to Fundamental and Practical Aspects of Electroanalysis*, 13(3), 173-180.

Beulen, B., Jong, J.d., Reinten, H., Berg, M.v.d., Wijshoff, H. and Van Dongen, R. (2007) 'Flows on the nozzle plate of an inkjet printhead', *Experiments in fluids*, 42(2), 217-224.

Biswas, K.G., Patra, R., Das, G., Ray, S. and Basu, J.K. (2015) 'Effect of flow orientation on liquid–liquid slug flow in a capillary tube', *Chemical Engineering Journal*, 262, 436-446.

Bretherton, F.P. (1961) 'The motion of long bubbles in tubes', *Journal of Fluid Mechanics*, 10(2), 166-188.

Burlage, K., Gerhardy, C., Praefke, H., Liauw, M. and Schomburg, W. (2013) 'Slug length monitoring in liquid–liquid Taylor-flow integrated in a novel PVDF micro-channel', *Chemical engineering journal*, 227, 111-115.

Burns, J. and Ramshaw, C. (2001) 'The intensification of rapid reactions in multiphase systems using slug flow in capillaries', *Lab on a Chip*, 1(1), 10-15.

Burns, M.A., Johnson, B.N., Brahmasandra, S.N., Handique, K., Webster, J.R., Krishnan, M., Sammarco, T.S., Man, P.M., Jones, D. and Heldsinger, D. (1998) 'An integrated nanoliter DNA analysis device', *Science*, 282(5388), 484-487.

Candoni, N., Grossier, R., Hammadi, Z., Morin, R. and Veesler, S. (2012) 'Practical physics behind growing crystals of biological macromolecules', *Protein and Peptide Letters*, 19(7), 714-724.

Candoni, N., Grossier, R., Lagaize, M. and Veesler, S. (2019) 'Advances in the use of microfluidics to study crystallization fundamentals', *Annual Review of Chemical and Biomolecular Engineering*, 10(1), 59-83.

Cao, Z., Wu, Z. and Sundén, B. (2018) 'Dimensionless analysis on liquid-liquid flow patterns and scaling law on slug hydrodynamics in cross-junction microchannels', *Chemical Engineering Journal*, 344, 604-615.

Carrigan, C.R. and Eichelberger, J.C. (1990) 'Zoning of magmas by viscosity in volcanic conduits', *Nature*, 343(6255), 248-251.

Chai, L., Xia, G., Zhou, M., Li, J. and Qi, J. (2013) 'Optimum thermal design of interrupted microchannel heat sink with rectangular ribs in the transverse microchambers', *Applied Thermal Engineering*, 51(1-2), 880-889.

Chao, X., Xu, F., Yao, C., Liu, T. and Chen, G. (2021) 'CFD simulation of internal flow and mixing within droplets in a T-junction microchannel', *Industrial & engineering chemistry research*, 60(16), 6038-6047.

Che, Z., Wong, T.N., Nguyen, N.-T. and Yang, C. (2015) 'Three dimensional features of convective heat transfer in droplet-based microchannel heat sinks', *International Journal of Heat and Mass Transfer*, 86, 455-464.

Chen, C.-T. and Lee, G.-B. (2006) 'Formation of microdroplets in liquids utilizing active pneumatic choppers on a microfluidic chip', *Journal of microelectromechanical systems*, 15(6), 1492-1498.

Chen, D.L., Li, L., Reyes, S., Adamson, D.N. and Ismagilov, R.F. (2007) 'Using three-phase flow of immiscible liquids to prevent coalescence of droplets in microfluidic channels: criteria to identify the third liquid and validation with protein crystallization', *Langmuir*, 23(4), 2255-2260.

Cherlo, S.K.R., Kariveti, S. and Pushpavanam, S. (2010) 'Experimental and numerical investigations of two-phase (liquid− liquid) flow behavior in rectangular microchannels', *Industrial & Engineering Chemistry Research*, 49(2), 893-899.

Chisholm, D. (1967) 'A theoretical basis for the Lockhart-Martinelli correlation for two-phase flow', *International Journal of Heat and Mass Transfer*, 10(12), 1767-1778.

Christopher, G.F. and Anna, S.L. (2007) 'Microfluidic methods for generating continuous droplet streams', *Journal of Physics D: Applied Physics*, 40(19), R319.

Cicchitti, A., Lombardi, C., Silvestri, M., Soldaini, G. and Zavattarelli, R. (1959) *Two-phase cooling experiments: pressure drop, heat transfer and burnout measurements*: Centro Informazioni Studi Esperienze, Milan.

Cybulski, A. and Moulijn, J.A. (2005) *Structured catalysts and reactors*, CRC press.

Dai, Z., Guo, Z., Fletcher, D.F. and Haynes, B.S. (2015) 'Taylor flow heat transfer in microchannels—Unification of liquid–liquid and gas–liquid results', *Chemical Engineering Science*, 138, 140-152.

Darekar, M., Singh, K.K., Mukhopadhyay, S. and Shenoy, K.T. (2017) 'Liquid–liquid two-phase flow patterns in Y-junction microchannels', *Industrial & Engineering Chemistry Research*, 56(42), 12215-12226.

de Ryck, A. (2002) 'The effect of weak inertia on the emptying of a tube', *Physics of Fluids*, 14(7), 2102-2108.

Dendukuri, D., Tsoi, K., Hatton, T.A. and Doyle, P.S. (2005) 'Controlled synthesis of nonspherical microparticles using microfluidics', *Langmuir*, 21(6), 2113-2116.

Deng, N., Wang, W., Ju, X., Xie, R., Liu, Z. and Chu, L. (2015) 'Recent advances in microfluidic manipulation and coalescence of microscale droplets', *Scientia Sinica Chimica*, 45(1), 7-15.

Dessimoz, A.-L., Cavin, L., Renken, A. and Kiwi-Minsker, L. (2008) 'Liquid–liquid two-phase flow patterns and mass transfer characteristics in rectangular glass microreactors', *Chemical Engineering Science*, 63(16), 4035-4044.

Devos, C., Van Gerven, T. and Kuhn, S. (2021) 'A review of experimental methods for nucleation rate determination in large-volume batch and microfluidic crystallization', *Crystal growth & design*, 21(4), 2541-2565.

Dombrowski, R.D., Litster, J.D., Wagner, N.J. and He, Y. (2007) 'Crystallization of alpha-lactose monohydrate in a drop-based microfluidic crystallizer', *Chemical Engineering Science*, 62(17), 4802-4810.

Dong, H., Carr, W.W. and Morris, J.F. (2006) 'An experimental study of drop-on-demand drop formation', *Physics of fluids*, 18(7), 072102.

Dore, V., Tsaoulidis, D. and Angeli, P. (2012) 'Mixing patterns in water plugs during water/ionic liquid segmented flow in microchannels', *Chemical engineering science*, 80, 334-341.

Du Plessis, J. and Collins, M. (1992) 'A new definition for laminar flow entrance lengths of straight ducts', *N&O Joernaal*, 25, 11-16.

Duan, X., Liu, L., Feng, F. and Wang, S. (2010) 'Cationic conjugated polymers for optical detection of DNA methylation, lesions, and single nucleotide polymorphisms', *Accounts of chemical research*, 43(2), 260-270.

Ducrée, J., Haeberle, S., Brenner, T., Glatzel, T. and Zengerle, R. (2006) 'Patterning of flow and mixing in rotating radial microchannels', *Microfluidics and Nanofluidics*, 2(2), 97-105.

Dukler, A., Wicks III, M. and Cleveland, R. (1964) 'Frictional pressure drop in two-phase flow: A. A comparison of existing correlations for pressure loss and holdup', *AIChE Journal*, 10(1), 38-43.

Eaton, W.P. and Smith, J.H. (1997) 'Micromachined pressure sensors: review and recent developments', *Smart Materials and Structures*, 6(5), 530.

Ebadian, M. and Lin, C. (2011) 'A review of high-heat-flux heat removal technologies', *Journal of heat transfer*, 133(11).

Edvinsson, R. and Irandoust, S. (1993) 'Hydrodesulfurization of dibenzothiophene in a monolithic catalyst reactor', *Industrial & engineering chemistry research*, 32(2), 391-395.

Edvinsson, R.K. and Irandoust, S. (1996) 'Finite-element analysis of Taylor flow', *AIChE Journal*, 42(7), 1815-1823.

Elamvaluthi, G. and Srinivas, N. (1984) 'Two-phase heat transfer in two component vertical flows', *Int. J. Multiphase Flow;(United Kingdom)*, 10(2).

Ern, P., Risso, F., Fabre, D. and Magnaudet, J. (2012) 'Wake-induced oscillatory paths of bodies freely rising or falling in fluids', *Annual Review of Fluid Mechanics*, 44(1), 97-121.

Etminan, A., Muzychka, Y.S. and Pope, K. (2021) 'A review on the hydrodynamics of Taylor flow in microchannels: Experimental and computational studies', *Processes*, 9(5), 870.

Everage Jr, A. (1973) 'Theory of stratified bicomponent flow of polymer melts. I. Equilibrium Newtonian tube flow', *Transactions of the Society of Rheology*, 17(4), 629-646.

Fabbri, M., Jiang, S. and Dhir, V.K. (2005) 'A comparative study of cooling of high power density electronics using sprays and microjets', *J. Heat Transfer*, 127(1), 38-48.

Fairbrother, F. and Stubbs, A.E. (1935) '119. Studies in electro-endosmosis. Part VI. The "bubble-tube" method of measurement', *Journal of the Chemical Society (Resumed)*, 527-529.

Ferraro, D., Serra, M., Filippi, D., Zago, L., Guglielmin, E., Pierno, M., Descroix, S., Viovy, J.-L. and Mistura, G. (2019) 'Controlling the distance of highly confined droplets in a capillary by interfacial tension for merging on-demand', *Lab on a Chip*, 19(1), 136-146.

Fidalgo, L.M., Whyte, G., Bratton, D., Kaminski, C.F., Abell, C. and Huck, W.T. (2008) 'From microdroplets to microfluidics: selective emulsion separation in microfluidic devices', *Angewandte Chemie*, 120(11), 2072-2075.

Figliola, R.S. and Beasley, D.E. (2020) *Theory and design for mechanical measurements*, John Wiley & Sons.

Fischer, M., Juric, D. and Poulikakos, D. (2010) 'Large convective heat transfer enhancement in microchannels with a train of coflowing immiscible or colloidal droplets', *Journal of heat transfer*, 132(11).

Fujioka, H. and Grotberg, J.B. (2005) 'The steady propagation of a surfactant-laden liquid plug in a two-dimensional channel', *Physics of fluids*, 17(8), 082102.

Galkin, O. and Vekilov, P.G. (2000) 'Are nucleation kinetics of protein crystals similar to those of liquid droplets?', *Journal of the American chemical society*, 122(1), 156-163.

Gao, J., Hu, Z., Yang, Q., Liang, X. and Wu, H. (2022) 'Fluid flow and heat transfer in microchannel heat sinks: Modelling review and recent progress', *Thermal Science and Engineering Progress*, 101203.

Gerard, C.J., Ferry, G., Vuillard, L.M., Boutin, J.A., Ferte, N., Grossier, R., Candoni, N. and Veesler, S. (2018) 'A chemical library to screen protein and protein–ligand

crystallization using a versatile microfluidic platform', *Crystal Growth & Design*, 18(9), 5130-5137.

Gettyimages (2022), available: https://www.gettyimages.ie/ [accessed

Ghani, I.A., Sidik, N.A.C. and Kamaruzaman, N. (2017) 'Hydrothermal performance of microchannel heat sink: The effect of channel design', *International Journal of Heat and Mass Transfer*, 107, 21-44.

Giavedoni, M.a.D. and Saita, F.A. (1997) 'The axisymmetric and plane cases of a gas phase steadily displacing a Newtonian liquid—A simultaneous solution of the governing equations', *Physics of fluids*, 9(8), 2420-2428.

Giavedoni, M.D. and Saita, F.A. (1999) 'The rear meniscus of a long bubble steadily displacing a Newtonian liquid in a capillary tube', *Physics of fluids*, 11(4), 786-794.

Gu, Y. and Fisher, A.C. (2013) 'An ac voltammetry approach for the detection of droplets in microfluidic devices', *Analyst*, 138(16), 4448-4452.

Gupta, R., Leung, S.S., Manica, R., Fletcher, D.F. and Haynes, B.S. (2013) 'Hydrodynamics of liquid–liquid Taylor flow in microchannels', *Chemical Engineering Science*, 92, 180-189.

Hamann, H.F., Weger, A., Lacey, J.A., Hu, Z., Bose, P., Cohen, E. and Wakil, J. (2006) 'Hotspot-limited microprocessors: Direct temperature and power distribution measurements', *IEEE Journal of Solid-State Circuits*, 42(1), 56-65.

Han, Y. and Shikazono, N. (2009) 'Measurement of the liquid film thickness in micro tube slug flow', *International Journal of Heat and Fluid Flow*, 30(5), 842-853.

Hanafi, B. (2014) *Design of silicon power ampliers and arrays for millimeter wave applications*, unpublished thesis, UC San Diego.

Harries, N., Burns, J., Barrow, D.A. and Ramshaw, C. (2003) 'A numerical model for segmented flow in a microreactor', *International journal of heat and mass transfer*, 46(17), 3313-3322.

Hatakeyama, T., Chen, D.L. and Ismagilov, R.F. (2006) 'Microgram-scale testing of reaction conditions in solution using nanoliter plugs in microfluidics with detection by MALDI-MS', *Journal of the American chemical society*, 128(8), 2518-2519.

Heil, M. (2001) 'Finite Reynolds number effects in the Bretherton problem', *Physics of Fluids*, 13(9), 2517-2521.

Helmers, T., Kemper, P., Thöming, J. and Mießner, U. (2022) 'The flow topology transition of liquid–liquid Taylor flows in square microchannels', *Experiments in Fluids*, 63(1), 1-24.

Hodges, S., Jensen, O. and Rallison, J. (2004) 'The motion of a viscous drop through a cylindrical tube', *Journal of Fluid Mechanics*, 501, 279-301.

Hosokawa, M., Nishikawa, Y., Kogawa, M. and Takeyama, H. (2017) 'Massively parallel whole genome amplification for single-cell sequencing using droplet microfluidics', *Scientific reports*, 7(1), 1-11.

Hotta, T. and Patil, N. (2018) 'A review on cooling of discrete heated modules using liquid jet impingement', *Frontiers in Heat and Mass Transfer (FHMT)*, 11.

Howard, J.A. and Walsh, P.A. (2013) 'Review and extensions to film thickness and relative bubble drift velocity prediction methods in laminar Taylor or slug flows', *International Journal of Multiphase Flow*, 55, 32-42.

Howard, J.A., Walsh, P.A. and Walsh, E.J. (2011) 'Prandtl and capillary effects on heat transfer performance within laminar liquid–gas slug flows', *International Journal of Heat and Mass Transfer*, 54(21-22), 4752-4761.

Huebner, A., Olguin, L.F., Bratton, D., Whyte, G., Huck, W.T., De Mello, A.J., Edel, J.B., Abell, C. and Hollfelder, F. (2008) 'Development of quantitative cell-based enzyme assays in microdroplets', *Analytical chemistry*, 80(10), 3890-3896.

Irandoust, S. and Andersson, B. (1989) 'Liquid film in Taylor flow through a capillary', *Industrial & engineering chemistry research*, 28(11), 1684-1688.

Isgor, P.K., Marcali, M., Keser, M. and Elbuken, C. (2015) 'Microfluidic droplet content detection using integrated capacitive sensors', *Sensors and Actuators B: Chemical*, 210, 669-675.

Jähnisch, K., Baerns, M., Hessel, V., Ehrfeld, W., Haverkamp, V., Löwe, H., Wille, C. and Guber, A. (2000) 'Direct fluorination of toluene using elemental fluorine in gas/liquid microreactors', *Journal of fluorine chemistry*, 105(1), 117-128.

Jakiela, S., Korczyk, P.M., Makulska, S., Cybulski, O. and Garstecki, P. (2012) 'Discontinuous transition in a laminar fluid flow: A change of flow topology inside a droplet moving in a micron-size channel', *Physical review letters*, 108(13), 134501.

Jakiela, S., Makulska, S., Korczyk, P.M. and Garstecki, P. (2011) 'Speed of flow of individual droplets in microfluidic channels as a function of the capillary number, volume of droplets and contrast of viscosities', *Lab on a Chip*, 11(21), 3603-3608.

Jeffers, N.M., Punch, J., Walsh, E.J. and McLean, M. (2009) 'Heat transfer from novel target surface structures to a normally impinging, submerged and confined water jet', *Journal of Thermal Science and Engineering Applications*, 1(3).

Jiang, S. and Horst, J.H. (2011) 'Crystal nucleation rates from probability distributions of induction times', *Crystal Growth & Design*, 11(1), 256-261.

Jin, B., Kim, Y., Lee, Y. and Yoo, J. (2010) 'Droplet merging in a straight microchannel using droplet size or viscosity difference', *Journal of Micromechanics and Microengineering*, 20(3), 035003.

Jiu-Sheng, C. and Jiang, J.-H. (2012) 'Droplet microfluidic technology: Mirodroplets formation and manipulation', *Chinese Journal of Analytical Chemistry*, 40(8), 1293-1300.

Joseph, D.D. and Renardy, Y.Y. (2013) *Fundamentals of two-fluid dynamics: part II: lubricated transport, drops and miscible liquids*, Springer Science & Business Media.

Jovanović, J., Zhou, W., Rebrov, E.V., Nijhuis, T., Hessel, V. and Schouten, J.C. (2011) 'Liquid–liquid slug flow: hydrodynamics and pressure drop', *Chemical Engineering Science*, 66(1), 42-54.

Kandlikar, S.G. (2002) 'Two-phase flow patterns, pressure drop, and heat transfer during boiling in minichannel flow passages of compact evaporators', *Heat Transfer Engineering*, 23(1), 5-23.

Kandlikar, S., Garimella, S., Li, D., Colin, S. and King, M.R. (2005) *Heat transfer and fluid flow in minichannels and microchannels*, elsevier.

Kashchiev, D. (2000) 'Nucleation: basic theory with applications. 1ª edição'.

Kashid, M. and Kiwi-Minsker, L. (2011) 'Quantitative prediction of flow patterns in liquid–liquid flow in micro-capillaries', *Chemical Engineering and Processing: Process Intensification*, 50(10), 972-978.

Kashid, M.N. and Agar, D.W. (2007) 'Hydrodynamics of liquid–liquid slug flow capillary microreactor: flow regimes, slug size and pressure drop', *Chemical Engineering Journal*, 131(1-3), 1-13.

Kashid, M.N., Agar, D.W. and Turek, S. (2007) 'CFD modelling of mass transfer with and without chemical reaction in the liquid–liquid slug flow microreactor', *Chemical Engineering Science*, 62(18-20), 5102-5109.

Kashid, M.N., Gupta, A., Renken, A. and Kiwi-Minsker, L. (2010) 'Numbering-up and mass transfer studies of liquid–liquid two-phase microstructured reactors', *Chemical Engineering Journal*, 158(2), 233-240.

Khan, W., Chandra, A.K., Kishor, K., Sachan, S. and Alam, M.S. (2017) 'Hydrodynamics and simulation studies of liquid-liquid slug flow in micro-capillaries', in *2017 International Conference on Advances in Mechanical, Industrial, Automation and Management Systems (AMIAMS)*, IEEE, 281-284.

Khomami, B. and Su, K.C. (2000) 'An experimental/theoretical investigation of interfacial instabilities in superposed pressure-driven channel flow of Newtonian and well characterized viscoelastic fluids: part I: linear stability and encapsulation effects', *Journal of non-newtonian fluid mechanics*, 91(1), 59-84.

King, C., Walsh, E. and Grimes, R. (2007) 'PIV measurements of flow within plugs in a microchannel', *Microfluidics and Nanofluidics*, 3(4), 463-472.

Kreutzer, M.T., Du, P., Heiszwolf, J.J., Kapteijn, F. and Moulijn, J.A. (2001) 'Mass transfer characteristics of three-phase monolith reactors', *Chemical Engineering Science*, 56(21-22), 6015-6023.

Kreutzer, M.T., Kapteijn, F., Moulijn, J.A. and Heiszwolf, J.J. (2005a) 'Multiphase monolith reactors: chemical reaction engineering of segmented flow in microchannels', *Chemical Engineering Science*, 60(22), 5895-5916.

Kreutzer, M.T., Kapteijn, F., Moulijn, J.A., Kleijn, C.R. and Heiszwolf, J.J. (2005b) 'Inertial and interfacial effects on pressure drop of Taylor flow in capillaries', *AIChE Journal*, 51(9), 2428-2440.

Kumari, S., Kumar, N. and Gupta, R., 2019. Flow and heat transfer in slug flow in microchannels: Effect of bubble volume. *International Journal of Heat and Mass Transfer*, *129*, pp.812-826.

Labrot, V., Schindler, M., Guillot, P., Colin, A. and Joanicot, M. (2009) 'Extracting the hydrodynamic resistance of droplets from their behavior in microchannel networks', *Biomicrofluidics*, 3(1), 012804.

Lac, E. and Sherwood, J. (2009) 'Motion of a drop along the centreline of a capillary in a pressure-driven flow', *Journal of Fluid Mechanics*, 640, 27-54.

Ładosz, A. and von Rohr, P.R. (2018) 'Pressure drop of two-phase liquid-liquid slug flow in square microchannels', *Chemical Engineering Science*, 191, 398-409.

Lee, C.Y. and Lee, S.Y. (2010) 'Pressure drop of two-phase dry-plug flow in round mini-channels: Effect of moving contact line', *Experimental Thermal and Fluid Science*, 34(1), 1-9.

Li, L., Mustafi, D., Fu, Q., Tereshko, V., Chen, D.L., Tice, J.D. and Ismagilov, R.F. (2006) 'Nanoliter microfluidic hybrid method for simultaneous screening and optimization validated with crystallization of membrane proteins', *Proceedings of the National Academy of Sciences*, 103(51), 19243-19248.

Li, M., Liu, Z., Pang, Y., Yan, C., Wang, J., Zhao, S. and Zhou, Q. (2020) 'Flow topology and its transformation inside droplets traveling in rectangular microchannels', *Physics of Fluids*, 32(5), 052009.

Li, Q. and Angeli, P. (2017) 'Experimental and numerical hydrodynamic studies of ionic liquid-aqueous plug flow in small channels', *Chemical Engineering Journal*, 328, 717-736.

Li, Z., Wu, J., Hu, G. and Hu, G. (2012) 'Fluid flow in microfluidic chips'.

Lin, S., Kwok, C., Li, R.-Y., Chen, Z.-H. and Chen, Z.-Y. (1991) 'Local frictional pressure drop during vaporization of R-12 through capillary tubes', *International Journal of Multiphase Flow*, 17(1), 95-102.

Lindken, R., Rossi, M., Große, S. and Westerweel, J. (2009) 'Micro-particle image velocimetry (μPIV): recent developments, applications, and guidelines', *Lab on a Chip*, 9(17), 2551-2567.

Link, D.R., Grasland-Mongrain, E., Duri, A., Sarrazin, F., Cheng, Z., Cristobal, G., Marquez, M. and Weitz, D.A. (2006) 'Electric control of droplets in microfluidic devices', *Angewandte Chemie International Edition*, 45(16), 2556-2560.

Liu, H., Vandu, C.O. and Krishna, R. (2005) 'Hydrodynamics of Taylor flow in vertical capillaries: flow regimes, bubble rise velocity, liquid slug length, and pressure drop', *Industrial & engineering chemistry research*, 44(14), 4884-4897.

Lockhart, R.W. (1949) 'Proposed correlation of data for isothermal two-phase, two-component flow in pipes', *Chem. Eng. Prog.*, 45, 39-48.

Ma, S., Sherwood, J.M., Huck, W.T. and Balabani, S. (2014) 'On the flow topology inside droplets moving in rectangular microchannels', *Lab on a Chip*, 14(18), 3611-3620.

Mac Giolla Eain, M., Egan, V., Howard, J., Walsh, P., Walsh, E. and Punch, J. (2015) 'Review and extension of pressure drop models applied to Taylor flow regimes', *International Journal of Multiphase Flow*, 68, 1-9.

Mac Giolla Eain, M., Egan, V. and Punch, J. (2013a) 'Film thickness measurements in liquid–liquid slug flow regimes', *International Journal of heat and fluid flow*, 44, 515-523.

Mac Giolla Eain, M., Egan, V. and Punch, J. (2015) 'Local Nusselt number enhancements in liquid–liquid Taylor flows', *International Journal of Heat and Mass Transfer*, 80, 85-97.

Mac Giolla Eain, M., Egan, V., Punch, J., Walsh, P. and Walsh, E. (2013b) 'An investigation of the pressure drop associated with liquid-liquid slug flows', in *International Conference on Nanochannels, Microchannels, and Minichannels*, American Society of Mechanical Engineers, V001T03A009.

Malsch, D., Kielpinski, M., Merthan, R., Albert, J., Mayer, G., Köhler, J., Süße, H., Stahl, M. and Henkel, T. (2008) 'µPIV-analysis of Taylor flow in micro channels', *Chemical Engineering Journal*, 135, S166-S172.

Méhault, C., Vanoye, L., Philippe, R. and de Bellefon, C. (2021) 'Multiphase alternated slug flows: conditions to avoid coalescence and characterization of mass transfer between droplets', *Chemical Engineering Journal*, 407, 127215.

Mudawar, I. and Bowers, M.B. (1999) 'Ultra-high critical heat flux (CHF) for subcooled water flow boiling—I: CHF data and parametric effects for small diameter tubes', *International Journal of Heat and Mass Transfer*, 42(8), 1405-1428.

Mukhaimer, A., Al-Sarkhi, A., El Nakla, M., Ahmed, W. and Al-Hadhrami, L. (2015) 'Pressure drop and flow pattern of oil–water flow for low viscosity oils: Role of mixture viscosity', *International Journal of Multiphase Flow*, 100(73), 90-96.

Niu, X., Zhang, M., Peng, S., Wen, W. and Sheng, P. (2007) 'Real-time detection, control, and sorting of microfluidic droplets', *Biomicrofluidics*, 1(4), 044101.

Prajapati, Y.K. and Bhandari, P. (2017) 'Flow boiling instabilities in microchannels and their promising solutions–A review', *Experimental Thermal and Fluid Science*, 88, 576-593.

Qian, G., Zhou, J., Zhang, J., Chen, C., Jin, R. and Liu, W. (2012) 'Microfiltration performance with two-phase flow', *Separation and purification technology*, 98, 165-173.

Rappaport, T.S., Sun, S., Mayzus, R., Zhao, H., Azar, Y., Wang, K., Wong, G.N., Schulz, J.K., Samimi, M. and Gutierrez, F. (2013) 'Millimeter wave mobile communications for 5G cellular: It will work!', *IEEE access*, 1, 335-349.

Ratulowski, J. and Chang, H.-C. (1990) 'Marangoni effects of trace impurities on the motion of long gas bubbles in capillaries', *Journal of Fluid Mechanics*, 210, 303-328.

Ratulowski, J. and Chang, H.C. (1989) 'Transport of gas bubbles in capillaries', *Physics of Fluids A: Fluid Dynamics*, 1(10), 1642-1655.

Reinelt, D. (1987) 'The rate at which a long bubble rises in a vertical tube', *Journal of Fluid Mechanics*, 175, 557-565.

Robert de Saint Vincent, M., Cassagnère, S., Plantard, J. and Delville, J.-P. (2012) 'Real-time droplet caliper for digital microfluidics', *Microfluidics and Nanofluidics*, 13(2), 261-271.

Roberts, C.C., Roberts, S.A., Nemer, M.B. and Rao, R.R. (2014) 'Circulation within confined droplets in Hele-Shaw channels', *Physics of Fluids*, 26(3), 032105.

Roy, S.K. and Avanic, B.L. (1996) 'A very high heat flux microchannel heat exchanger for cooling of semiconductor laser diode arrays', *IEEE Transactions on Components, Packaging, and Manufacturing Technology: Part B*, 19(2), 444-451.

Salim, A., Fourar, M., Pironon, J. and Sausse, J. (2008) 'Oil–water two-phase flow in microchannels: Flow patterns and pressure drop measurements', *The Canadian Journal of Chemical Engineering*, 86(6), 978-988.

Schwartz, L., Princen, H. and Kiss, A. (1986) 'On the motion of bubbles in capillary tubes', *Journal of Fluid Mechanics*, 172, 259-275.

Seo, M., Nie, Z., Xu, S., Mok, M., Lewis, P.C., Graham, R. and Kumacheva, E. (2005) 'Continuous microfluidic reactors for polymer particles', *Langmuir*, 21(25), 11614-11622.

Shintaku, H., Kuwabara, T., Kawano, S., Suzuki, T., Kanno, I. and Kotera, H. (2007) 'Micro cell encapsulation and its hydrogel-beads production using microfluidic device', *Microsystem technologies*, 13(8), 951-958.

Smakulski, P. and Pietrowicz, S. (2016) 'A review of the capabilities of high heat flux removal by porous materials, microchannels and spray cooling techniques', *Applied thermal engineering*, 104, 636-646.

Song, H. and Ismagilov, R.F. (2003) 'Millisecond kinetics on a microfluidic chip using nanoliters of reagents', *Journal of the American Chemical Society*, 125(47), 14613-14619.

Sun, T. and Morgan, H. (2010) 'Single-cell microfluidic impedance cytometry: a review', *Microfluidics and Nanofluidics*, 8(4), 423-443.

Suo, M. and Griffith, P. (1964) 'Two-phase flow in capillary tubes'.

Sur, A. and Liu, D. (2012) 'Adiabatic air–water two-phase flow in circular microchannels', *International Journal of Thermal Sciences*, 53, 18-34.

Suresh, V. and Grotberg, J. (2005) 'The effect of gravity on liquid plug propagation in a two-dimensional channel', *Physics of fluids*, 17(3), 031507.

Svärd, M., Nordström, F.L., Jasnobulka, T. and Rasmuson, Å.C. (2010) 'Thermodynamics and nucleation kinetics of m-aminobenzoic acid polymorphs', *Crystal growth & design*, 10(1), 195-204.

Talimi, V., Muzychka, Y. and Kocabiyik, S. (2012) 'A review on numerical studies of slug flow hydrodynamics and heat transfer in microtubes and microchannels', *International Journal of Multiphase Flow*, 39, 88-104.

Taly, V., Kelly, B.T. and Griffiths, A.D. (2007) 'Droplets as microreactors for high-throughput biology', *ChemBioChem*, 8(3), 263-272.

Taylor, G. (1961) 'Deposition of a viscous fluid on the wall of a tube', *Journal of Fluid Mechanics*, 10(2), 161-165.

Thome, J.R. and Cioncolini, A. (2017) 'Flow boiling in microchannels' in *Advances in Heat Transfer* Elsevier, 157-224.

Thorsen, T., Roberts, R.W., Arnold, F.H. and Quake, S.R. (2001) 'Dynamic pattern formation in a vesicle-generating microfluidic device', *Physical review letters*, 86(18), 4163.

Thulasidas, T., Abraham, M. and Cerro, R. (1997) 'Flow patterns in liquid slugs during bubble-train flow inside capillaries', *Chemical engineering science*, 52(17), 2947-2962.

Tilton, D.E., Pais, M.R. and Chow, L.C. (1989) *High power density spray cooling*: KENTUCKY UNIV LEXINGTON DEPT OF MECHANICAL ENGINEERING.

Tsaoulidis, D. and Angeli, P. (2016) 'Effect of channel size on liquid-liquid plug flow in small channels', *AIChE Journal*, 62(1), 315-324.

Tsaoulidis, D., Dore, V., Angeli, P., Plechkova, N.V. and Seddon, K.R. (2013) 'Flow patterns and pressure drop of ionic liquid–water two-phase flows in microchannels', *International Journal of Multiphase Flow*, 54, 1-10.

Tuckerman, D.B. and Pease, R.F.W. (1981) 'High-performance heat sinking for VLSI', *IEEE Electron device letters*, 2(5), 126-129.

Urbant, P., Leshansky, A. and Halupovich, Y. (2008) 'On the forced convective heat transport in a droplet-laden flow in microchannels', *Microfluidics and Nanofluidics*, 4(6), 533-542.

Vanapalli, S.A., Banpurkar, A.G., Van Den Ende, D., Duits, M.H. and Mugele, F. (2009) 'Hydrodynamic resistance of single confined moving drops in rectangular microchannels', *Lab on a Chip*, 9(7), 982-990.

Veesler, S. and Puel, F. (2015) 'Crystallization of pharmaceutical crystals' in *Handbook of Crystal Growth* Elsevier, 915-949.

Waelchli, S. and von Rohr, P.R. (2006) 'Two-phase flow characteristics in gas–liquid microreactors', *International Journal of Multiphase Flow*, 32(7), 791-806.

Walsh, E., Muzychka, Y., Walsh, P., Egan, V. and Punch, J. (2009) 'Pressure drop in two phase slug/bubble flows in mini scale capillaries', *International Journal of Multiphase Flow*, 35(10), 879-884.

Ward, T., Faivre, M., Abkarian, M. and Stone, H.A. (2005) 'Microfluidic flow focusing: Drop size and scaling in pressure versus flow-rate-driven pumping', *Electrophoresis*, 26(19), 3716-3724.

Warnier, M., De Croon, M., Rebrov, E. and Schouten, J. (2010) 'Pressure drop of gas–liquid Taylor flow in round micro-capillaries for low to intermediate Reynolds numbers', *Microfluidics and Nanofluidics*, 8(1), 33-45.

Weber, E., Puchberger-Enengl, D., Keplinger, F. and Vellekoop, M.J. (2013) 'In-line characterization and identification of micro-droplets on-chip', *Optofluidics*, 1(2013), 11-18.

Wegmann, A. and Rudolf von Rohr, P. (2006) 'Two phase liquid–liquid flows in pipes of small diameters', *International Journal of Multiphase Flow*, 32(8), 1017-1028.

Willaime, H., Barbier, V., Kloul, L., Maine, S. and Tabeling, P. (2006) 'Arnold tongues in a microfluidic drop emitter', *Physical review letters*, 96(5), 054501.

Wu, Z., Cao, Z. and Sundén, B. (2017) 'Liquid-liquid flow patterns and slug hydrodynamics in square microchannels of cross-shaped junctions', *Chemical Engineering Science*, 174, 56-66.

Xiao, Z. and Zhang, B. (2011) 'Droplet microfluidics: technologies and applications', *Se pu= Chinese Journal of Chromatography*, 29(10), 949-956.

Xu, K.-W., Zhang, Y., Liu, D., Azman, A.N. and Kim, H.-B. (2020) 'Slug flow development study in a horizontal pipe using particle image velocimetry', *International Journal of Heat and Mass Transfer*, 162, 120267.

Xu, S., Nie, Z., Seo, M., Lewis, P., Kumacheva, E., Stone, H.A., Garstecki, P., Weibel, D.B., Gitlin, I. and Whitesides, G.M. (2005) 'Generation of monodisperse particles by using microfluidics: control over size, shape, and composition', *Angewandte Chemie*, 117(5), 734-738.

Zadeh, S.S.S., Egan, V. and Walsh, P. (2022) 'An Experimental Study on the Mobility of Droplets in Liquid-Liquid Taylor Flows within Circular Capillaries', *International Journal of Multiphase Flow*, 104259.

Zec, H.C., Zheng, T., Liu, L., Hsieh, K., Rane, T.D., Pederson, T. and Wang, T.-H. (2018) 'Programmable microfluidic genotyping of plant DNA samples for marker-assisted selection', *Microsystems & Nanoengineering*, 4(1), 1-10.

Zhang, K., Hu, P., Liang, Q. and Luo, G. (2008) 'Control and application of microdroplet in microfluidic chip', *Chinese Journal of Analytical Chemistry*.

Zhang, M., Pan, L.-m., Ju, P., Yang, X. and Ishii, M. (2017) 'The mechanism of bubbly to slug flow regime transition in air-water two phase flow: A new transition criterion', *International Journal of Heat and Mass Transfer*, 108, 1579-1590.

Zhao, S., Riaud, A., Luo, G., Jin, Y. and Cheng, Y. (2015) 'Simulation of liquid mixing inside micro-droplets by a lattice Boltzmann method', *Chemical Engineering Science*, 131, 118-128.

Zheng, B., Roach, L.S. and Ismagilov, R.F. (2003) 'Screening of protein crystallization conditions on a microfluidic chip using nanoliter-size droplets', *Journal of the American chemical society*, 125(37), 11170-11171.

Zheng, Y., Fujioka, H. and Grotberg, J. (2007) 'Effects of gravity, inertia, and surfactant on steady plug propagation in a two-dimensional channel', *Physics of Fluids*, 19(8), 082107.

Appendix A

Published Work

A.1. Journal Papers

- Zadeh, S.S.S., Egan, V. and Walsh, P., 2022. An experimental study on the mobility of droplets in liquid-liquid Taylor flows within circular capillaries. *International Journal of Multiphase Flow*, *157*, p.104259.
  https://doi.org/10.1016/j.ijmultiphaseflow.2022.104259

- Zadeh, S.S.S., Egan, V. and Walsh, P., 2022. Real-Time Measurement Technique for Slug Flow Characterisation. *Journal of Fluid Flow, Heat and Mass Transfer (JFFHMT)*, *9*(1), p.191.
  DOI: 10.11159/jffhmt.2022.023

- Zadeh, S.S.S., Egan, V. and Walsh, P. Experimentally Investigating the Pressure Drop of Liquid-Liquid Taylor Flows Over Varying Viscosity Ratios.
  Under review in: *International Journal of Multiphase Flow*.

A.2. Conference Papers

- Zadeh, S.S.S., Walsh, P. and Egan, V., 2021, November. Velocity measurements of individual droplets in liquid-liquid Taylor flows in circular capillaries. In *Journal of Physics: Conference Series* (Vol. 2116, No. 1, p. 012074). *8th European Thermal Sciences Conference (EUROTHERM 2021).* 20-22 September 2021, VIRTUAL
  DOI:10.1088/1742-6596/2116/1/012074

- Zadeh, S.S.S., Egan, V. and Walsh, P., Experimental Investigation on Pressure Drop In Liquid-Liquid Taylor Flow Regimes. *The 9th International Conference on Heat Transfer and Fluid Flow (HTFF 2022) July 31-August 02, 2022, Prague, Czech Republic* .
  DOI: 10.11159/htff22.156

- Zadeh, S.S.S., Egan, V. and Walsh, P., High Frequency Flow Measurement Technique for Slug Flow Regimes. *The 9th International Conference on Heat Transfer and Fluid Flow (HTFF 2022) July 31-August 02, 2022, Prague, Czech Republic*. (**Best Paper Award**)
  DOI: 10.11159/htff22.144.

Appendix B

Manufacturers' Specifications

The following section includes a detailed manufacturer's specifications of the equipment and consumables used in this thesis.

Table B.1. Manufacturer's specifications of the equipment and consumables used in chapter 3, 4 and 5.

Product	Description
32 Bit Teensy 3.6 board 180 MHz Cortex-M4F 3.3V signals Manufacture Number: 78106 SL005	Microcontroller Chip MK66FX1M0VMD18, USB High Speed (480 Mbit/sec) Port, 2 CAN Bus Ports, 32 General Purpose DMA Channels, 22 PWM Outputs, 4 I2C Ports, 11 Touch Sensing Inputs. https://www.adafruit.com
Multicore Cable 6 Core, 28 AWG, 0.0925 mm², 100 ft, 30.5 m. Manufacture Number: 3266	Conductor: AWG Tinned Copper Insulation: 0.007" Wall, Nom. Modified Polyphenylene Ether-PE Colour Code: Alpha Wire Colour Code E https://ie.farnell.com
Hamilton™ 1000 Series Gastight™ Syringes: Luer Lock Syringes, TLL Termination Manufacture Number: 10500052	PTFE Luer Lock (TLL)- This termination has a PTFE, male Luer taper with nickel-plated brass locking hub for use with Kel-F needles, metal hub needles, and universal connectors. Mid-volume GASTIGHT syringe ideal for dispensing volumes from 100 µL up to 100 mL. https://www.fishersci.ie
Masterflex™ FEP Tubing Manufacture Number: 15367065	Inner diameter: 0.5 to 1.6 mm Maximum pressure: 444 psi Material: FEP Overall length: 7.6 m Min. operating temperature: -270°C Max. operating temperature: 204°C Colour: translucent https://www.fishersci.ie

Honeywell Differential Pressure Sensor, 1, 5, 15psi Manufacture Number: 26PCA(B)(C)FA6D	Pressure Reading Type Differential Minimum Pressure Reading: 0psi Maximum Pressure Reading: 15psi Accuracy: ±0.25 % Output Type: Unamplified Electrical Connection: 4-Pin Connector Analogue Output: 97 → 103 mV Response Time: 1ms Supply Voltage:10V dc Minimum Operating Temperature: -40°C Maximum Operating Temperature: +85°C https://ie.rs-online.com
FC40 Molecular formula: C21F48N2	Acota FC40, Perfluorotri-n-butylamine mixture with Perfluoro-n-dibutylmethylamine. Boiling point range 158.0 - 173.0°C, density 1.845-1.895 g/ml at. Colour: translucent https://www.acota.co.uk
HFE7500 Molecular formula: C9H5F15O	Acota HFE7500, hydrofluoroether fluid Contains no chlorine or bromine. Non-flammable, boiling point 129 °C, density 1.63 g/ml. Colour: translucent https://www.acota.co.uk
Silicone oil AR 20 Polyphenyl-Methylsiloxane	Aldrich AR 20 Viscosity:~20 mPa.s, at 25 °C Density:1.000-1.020 g/mL at 20 °C Colour: translucent https://www.sigmaaldrich.com

Appendix C

Viscosity Temperature Charts of Liquids

The temperature-dependent variations in viscosity of the liquids, investigated in this study, are shown in the following plots. Each graph also includes the fitting curve equation linking the viscosity and temperature. The viscosity of the liquids were determined by measuring the pressure drop along a certain length of the tubing and applying the Hagen-Poiseuille equation for laminar flow in a straight, circular capillary. These procedures were carried out over the temperature ranges in which the measurements were conducted.

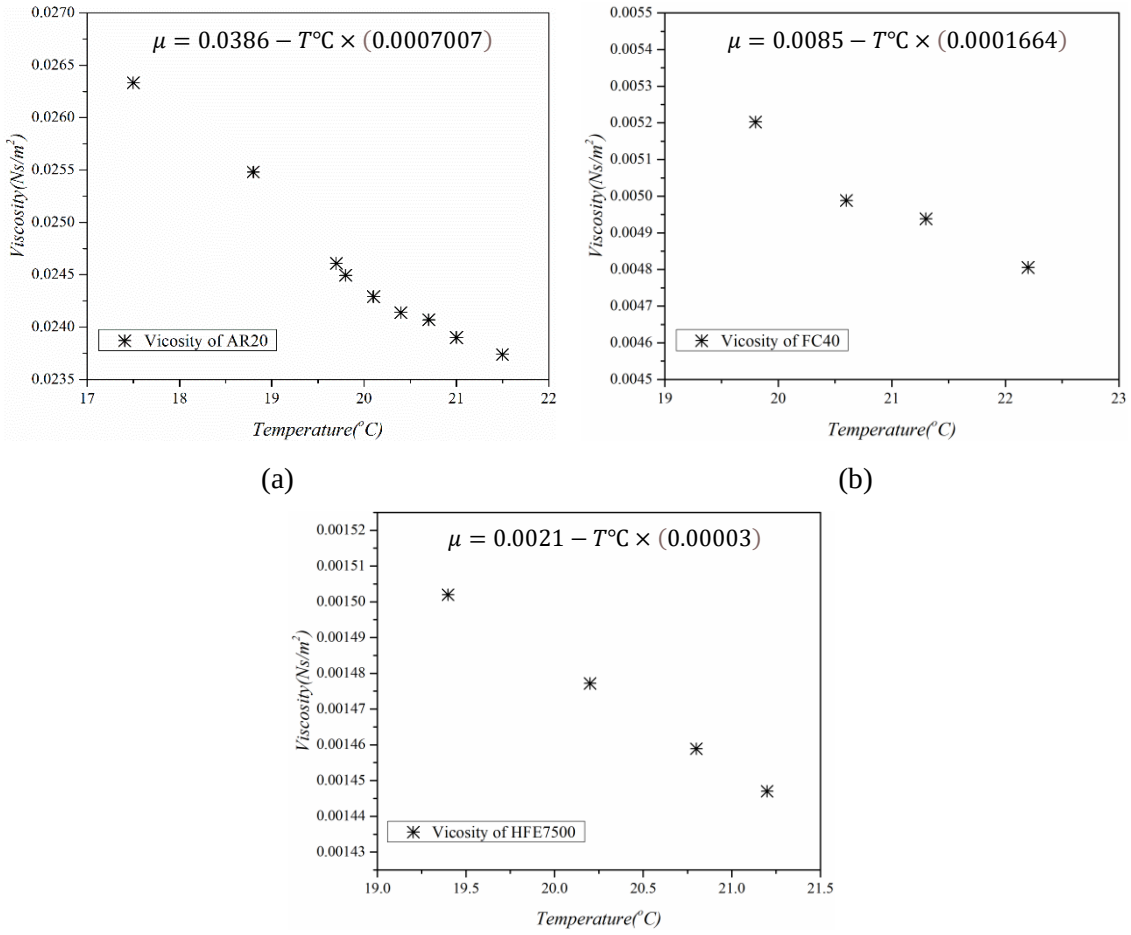

Figure C.1. Viscosity-temperature plot for (a) AR20, (b) FC40, and (c) HFE7500.

Appendix D

Calibration Procedure for Pressure Transducer

Prior to use, all four transducers were calibrated using Hagen-Poiseuille theory for single-phase flow in a circular tube with output voltage related to Hagen-Poiseuille pressure drop prediction. A laminar flow of water through a tube with $2m$ long and $0.8mm$ diameter was employed to make the correlation between the pressure drop and the output voltage (see Figure D.1). Although the sensors of the 26PC series manufactured by Honeywell guarantee a linearity of 0.5%, all the pressure transducers were calibrated in both infuse and refill directions and results prove the linearity assumption. The graphical description of the calibration curves and the curve fitting equations are shown in Figure D.2.

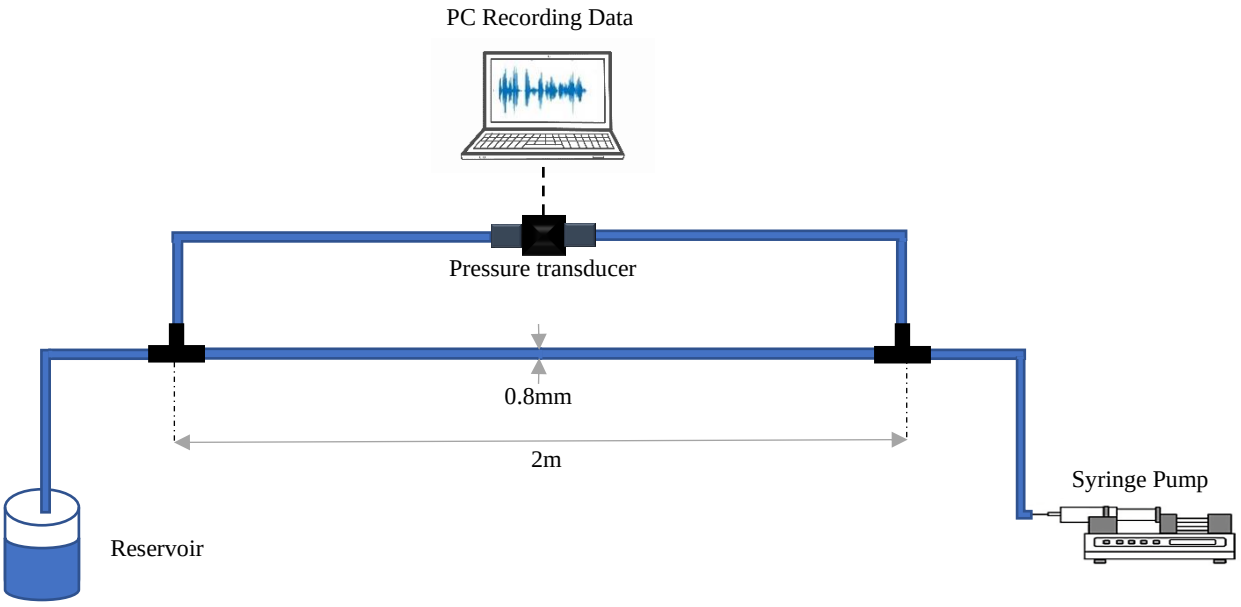

Figure D.1. The measurement configuration for pressure transducer calibration.

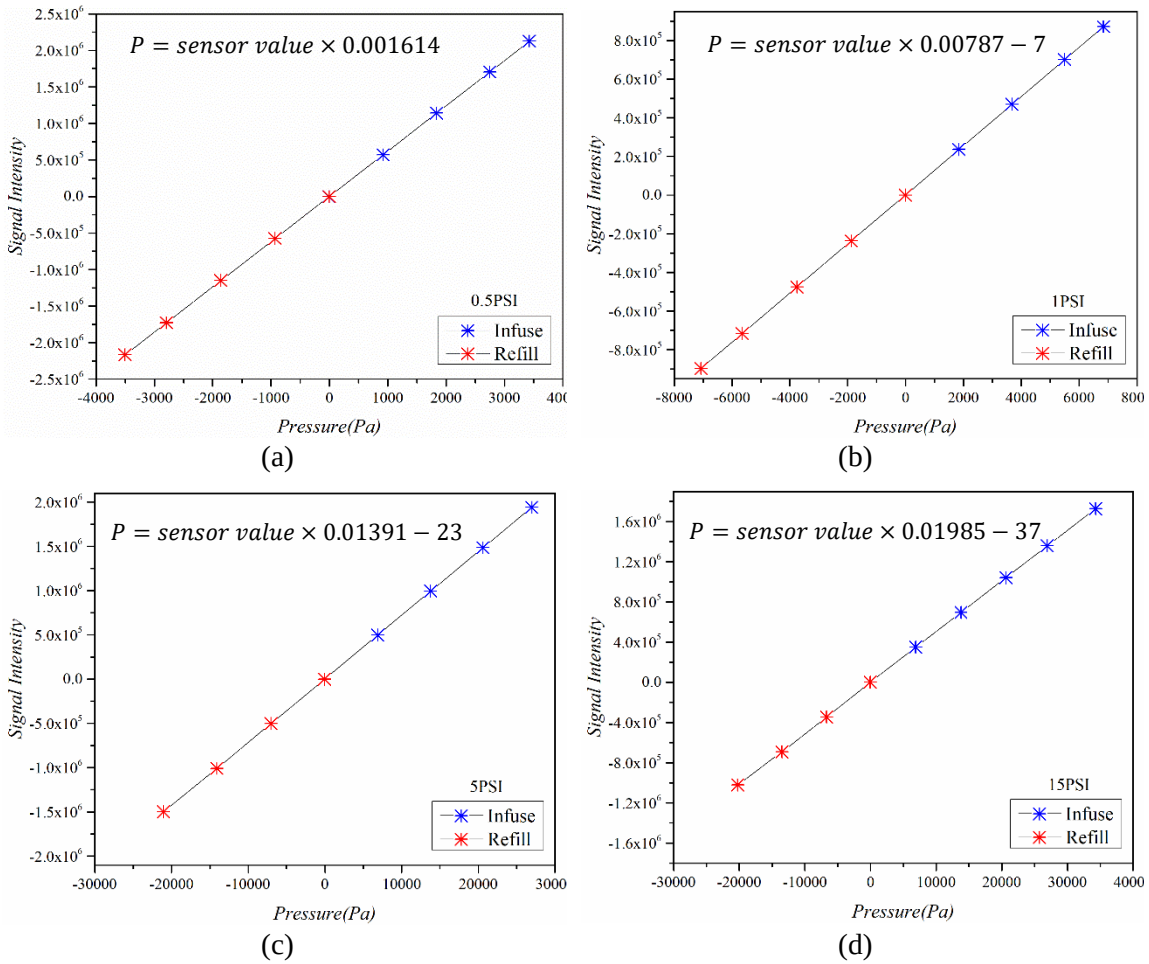

Figure D.2. Calibration curve and the curve fitting equation for pressure transducers with ranges of (a) ±0.5PSI, (b) ±1PSI, (c) ±5PSI, and (d) ±15PSI.

Appendix E

MATLAB Code for Post-Processing the Signals from Photodiodes

```
clear all
clc
filename='Book1.xlsx';
time=xlsread(filename,'A:A');
sens_1=xlsread(filename,'b:b');
sens_2=xlsread(filename,'c:c');
L=1; %distance between two sensors(m)
fprintf("Sensor 2: ");
[dots_2,times_2] = nextFunc(time,sens_2)
fprintf("Sensor 1: ");
[dots_1,times_1] = nextFunc(time,sens_1)

droplets_num=size(times_1,2);
for i=1:1:droplets_num;
   speed(i,1)=L/(times_2(1,i)-times_1(1,i));
   droplen_1(i,1)=speed(i,1)*(times_1(4,i)-times_1(1,i));
   droplen_2(i,1)=speed(i,1)*(times_2(4,i)-times_2(1,i));
   Slug_length_1(i,1)=speed(i,1)*(times_1(1,i+1)-
times_1(4,i));
   Slug_length_2(i,1)=speed(i,1)*(times_2(1,i+1)-
times_2(4,i));
   Average_Slug_1=mean(Slug_length_1);
   Average_Slug_2=mean(Slug_length_2);
   Average_Droplets=mean(droplen_1);
end
%nextFunc
function [result_matrix,result_time] = nextFunc(time,sensor)
    step=0;
    matrix_counter=1;
    min=999999;
    max=sensor(1);
    normal_value = sensor(1);
    noise=200;
    last_time = time(1);
    for i=1:size(time)
        if(step==0)
            if(sensor(i)-noise>max)
                max = sensor(i);%take off
                step=1;
```

```
                result_matrix(1,matrix_counter)=sensor(i);
                result_time(1,matrix_counter)=time(i);
            end
        elseif(step==1)
            if(max<sensor(i))
                max=sensor(i);
                last_time =time(i);
            elseif(max>sensor(i)+noise)
                result_matrix(2,matrix_counter)=max;%first
hill
                result_time(2,matrix_counter)=last_time;
                step=2;
            end
        elseif(step==2)
            if(min>sensor(i))
                min = sensor(i);
                last_time =time(i);
            elseif(min+1000<sensor(i))
                result_matrix(3,matrix_counter)=min;%first
valley
                result_time(3,matrix_counter)=last_time;
                step = 3;
                max=min;
            end
        elseif(step==3)
            if(max<sensor(i))
                max = sensor(i);
                last_time =time(i);
            elseif(max>sensor(i)+7500)

result_matrix(4,matrix_counter)=sensor(i);%second hill
                result_time(4,matrix_counter)=time(i);
                step = 4;
                min = max;
            end
        elseif(step==4)
            if(min>sensor(i))
                min = sensor(i);
                last_time =time(i);
            elseif(min+5000<sensor(i))
                result_matrix(5,matrix_counter)=min;%second
valley
                result_time(5,matrix_counter)=last_time;
                max=min;
                step = 5;
            end
        elseif(step==5)
            if(max<sensor(i))
                max = sensor(i);
                last_time =time(i);
            elseif(max>sensor(i)+200)
```

```
                result_matrix(6,matrix_counter)=max;%third
hill
                result_time(6,matrix_counter)=last_time;
                step =6;
                min = max;
            end
        elseif(step==6)
            if(min>sensor(i))
                min = sensor(i);
                last_time = time(i);
            %reset algorithm if sensor value returned to
normal zone
            elseif(abs(normal_value-sensor(i))<100)
                result_matrix(7,matrix_counter)=max;%back to
normal
                result_time(7,matrix_counter)=last_time;
                matrix_counter = matrix_counter +1;
                step =0;
                max = sensor(i);
                min = 9999999;
            end
        end
    end
    soundsc(2);
end
```

Appendix F

Design and Fabrication of a Small Vertical 1-D Traverse System for Precision Motion Control

This appendix presents a comprehensive step-by-step procedure for the construction and programming of the single-axis traverse system utilized in the study. The details provided here offer clear guidance on how the system was designed and implemented for precise motion control in the experimental setup.

Materials and Tools:

Stepper motor: NEMA17 stepper motor 1.8 degrees per step, 47 mm long. With its robust design, this high-performance stepper motor is well-suited for a wide range of RepRap 3D printers and CNC machines. Its D-shaped shaft facilitates effortless attachment of pulleys and couplings, making it a convenient choice for various applications.

Figure F.1. Stepper motor used in the traverse system construction.

Pulleys: Select pulleys that match the size and specifications of the stepper motor shaft.

Belt: Use a suitable timing belt that fits the pulleys and provides the desired motion.

Figure F.2. Pulley and belt used in the traverse system construction.

Mounting structure: A mounting structure is designed and 3D printed to precisely position the components.

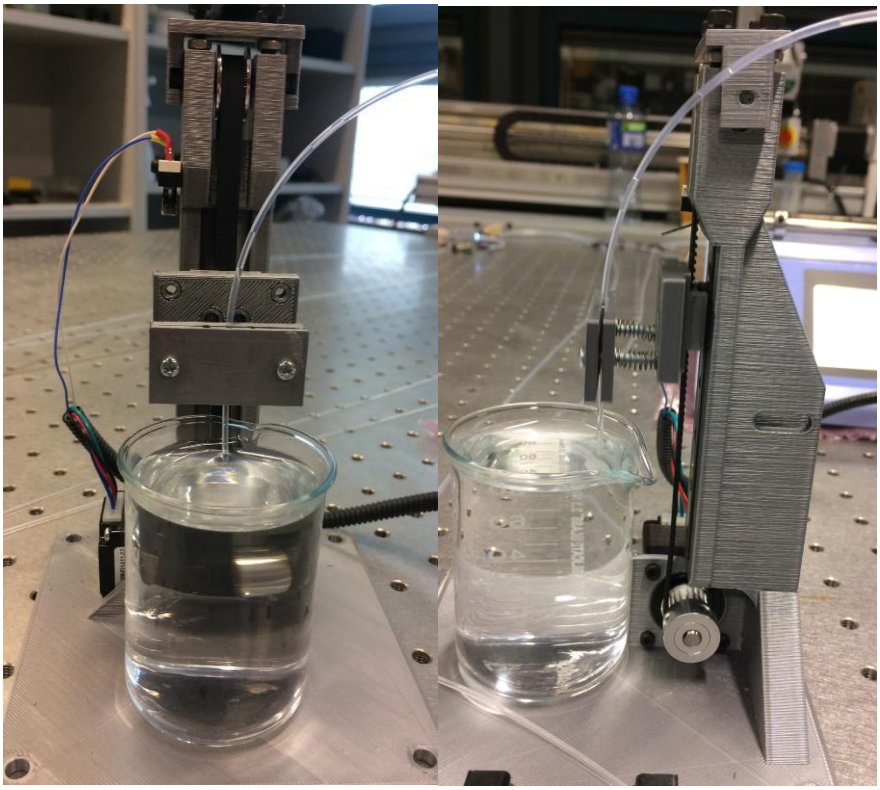

Figure F.3. 3-D printed mounting structure to precisely position the components used in the traverse system.

Power supply: Based on specifications of the actuator, a 24V-DC power supply unit is employed to provide an appropriate power source.

Control system: An Arduino Uno is used to program and control the stepper motor's movements.

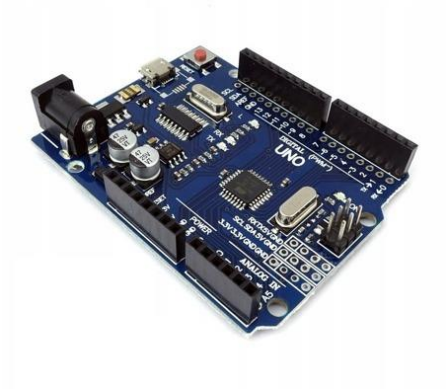

Figure F.4. Arduino controller board used to program and control the stepper motor.

Connecting wires: These are used to connect the linear actuator to the power supply and control system.

Basic hand tools: Screwdriver, drill, screws, nuts, and bolts for assembly.

Procedure:

Design and 3D printing the mounting brackets and structure: These holders provide a secure assembly of the stepper motor, pulleys, and belt.

Pulley Installation: Attach the pulleys to the stepper motor shaft and the desired endpoint of the traverse system. Ensure proper alignment between the pulleys for smooth motion and accurate positioning.

Stepper Motor Mounting: Securely mount the stepper motor on the mounting brackets, aligning it properly with the pulleys.

Belt Installation and Tensioning: Place the timing belt around the pulleys, ensuring proper alignment and engagement. Adjust the tension of the belt to achieve optimal engagement and minimize slippage.

Wiring and Connections: Connect the motor to the controller board/Arduino board following the manufacturer's specifications. Connect the stepper motor to the power supply, ensuring the voltage and current requirements are met.

Programming: Develop a program using the chosen controller's programming language (e.g., Arduino IDE, Python, etc.). Utilize stepper motor libraries or commands specific to

the controller to control the motor's position, speed, and direction. Below is an Arduino sketch written in C++ to control the linear actuator using two push buttons. The code uses the **Stepper** library, which allows the linear actuator's position to be adjusted incrementally based on the state of the push buttons.

```
#include <AccelStepper.h>
// Pin assignments
const int stepPin = 9;    // Connect the stepper motor step pin to pin 9
const int dirPin = 10;    // Connect the stepper motor direction pin to pin 10
const int buttonUpPin = 2;      // Connect the button for upward motion to pin 2
const int buttonDownPin = 3;    // Connect the button for downward motion to pin 3
// Variables
AccelStepper stepper(AccelStepper::DRIVER, stepPin, dirPin);
int currentPosition = 0;
const int stepSize = 5;   // Adjust this value to set the step size of linear actuator motion
void setup() {
  stepper.setMaxSpeed(1000);   // Adjust the maximum speed of the stepper motor if needed
  stepper.setAcceleration(500); // Adjust the acceleration of the stepper motor if needed
  pinMode(buttonUpPin, INPUT_PULLUP);
  pinMode(buttonDownPin, INPUT_PULLUP);
}
void loop() {
  // Check if the button for upward motion is pressed
  if (digitalRead(buttonUpPin) == LOW) {
    currentPosition += stepSize;
    moveStepper(currentPosition);
    delay(100); // Adjust this delay to control the speed of motion
  }
  // Check if the button for downward motion is pressed
  if (digitalRead(buttonDownPin) == LOW) {
    currentPosition -= stepSize;
    moveStepper(currentPosition);
```

```
    delay(100); // Adjust this delay to control the speed of motion
  }
}
// Function to move the stepper motor to the desired position
void moveStepper(int position) {
  // Ensure the position is within the desired range
  position = constrain(position, 0, 180);
  // Move the stepper motor to the desired position
  stepper.moveTo(position);
  stepper.runToPosition();
}
```

In this code, the linear actuator is controlled using the Stepper library, and two buttons connected to the Arduino are used to control the upward and downward motion. Each button press increments or decrements the currentPosition variable by the stepSize, and the moveLinearActuator() function moves the linear actuator to the desired position. Adjust the stepSize and delay values as needed to suit your specific requirements.

Please note that this code is a basic example to get you started. Depending on your specific setup and requirements, you may need to modify and adapt the code accordingly.

To control a traverse system using G-code, you'll need a microcontroller or controller board that supports G-code interpretation. One popular option is to use a CNC controller board, such as an Arduino-based board running GRBL firmware. Here's a general outline of the steps involved:

1. Set up the Hardware:
    - Connect the linear actuator to the traverse system as per the manufacturer's instructions.
    - Connect the CNC controller board to your computer via USB or another suitable interface.
2. Install the Required Software:

- Install a G-code sender program on your computer. Some popular options are Universal Gcode Sender (UGS), bCNC, or CNCjs. These programs allow you to send G-code commands to the controller board.
- Install the necessary firmware on the CNC controller board. For an Arduino-based board, the GRBL firmware can be used to flash it.

3. Configure the Controller Board:
    - Follow the instructions specific to your controller board to configure it correctly. This typically involves setting the steps per millimeter or inch for your linear actuator and other motor-related settings.
4. Generate or Obtain G-code:
    - Create or obtain the G-code file that contains the commands to control your traverse system. G-code is a standard programming language used in CNC machines to control their movements. Each command specifies a specific action, such as moving to a position or changing the speed.
5. Connect and Send G-code:
    - Open the G-code sender program on your computer and connect it to the controller board.
    - Load the G-code file into the sender program.
    - Use the program's interface to send the G-code commands to the controller board.
    - The controller board interprets the G-code commands and controls the linear actuator to perform the desired movements.

Appendix G

Validation of Photodiode Sensor Signal Analysis for Droplet Length Measurement

This appendix outlines the validation procedure employed to ensure the accuracy of length measurements obtained by signal analysis from photodiodes. The approach involves a comparison of droplet length measurements derived from the optical technique to establish the reliability and precision of the signal analysis. In this procedure, a high-speed camera and a meshed paper with a known mesh size of 5 mm are used to precisely measure the droplet length. The mesh size was meticulously measured with a calliper under a microscope.

The experimental setup involved placing the meshed paper at an optimal distance from the tubing and capturing clear and focused images of the droplets passing across the meshed area. In parallel with the meshed paper technique, two photodiode sensors were set up to measure the droplet length. Throughout the experiment, data was collected by capturing a substantial number of droplet images using the high-speed camera, while the corresponding droplet length measurements were recorded from the photodiode sensors.

Signal analysis was then conducted to compare the measurements obtained from both the high-speed camera images and the photodiodes readings, assessing the degree of agreement between the two techniques. The validated measurements obtained from the meshed paper technique served as the reference for determining the "actual" droplet length, enabling accurate signal analysis. To ensure the reliability of the findings, the experiment was replicated multiple times with various droplet lengths. An example image from the procedure is provided in Figure G.1.

Figure G.1. illustration of the meshed paper with a precisely known mesh size used as a reference for determining droplet length through signal analysis from photodiodes. In this image, the mesh size and the inlet diameter of the tubing are measured to be 5 mm and 800 µm.

Appendix H

Supplementary Figures Related to Chapter 4

This appendix presents additional figures related to the main content of Chapter 4. These additional figures offer a more detailed observation of the critical zones where significant changes occur in the dataset. The enhanced insight gained from these additional figures will further support the findings and conclusions presented in the chapter, facilitating a more comprehensive understanding of the data analysis.

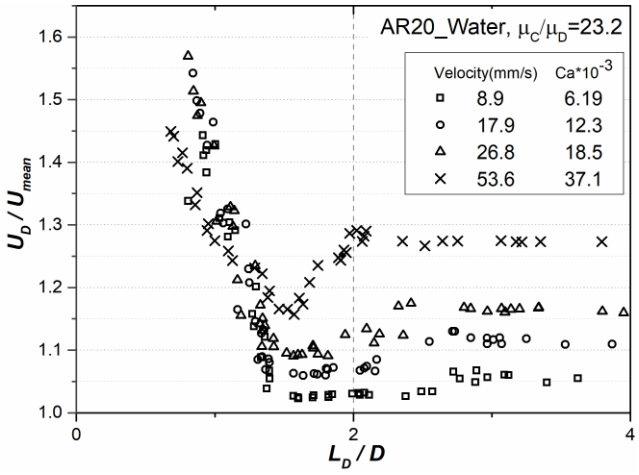

Figure H.1. Variation in droplet velocity ratio with dimensionless droplet length for experiments with AR20_Water while Bo = 0.11.

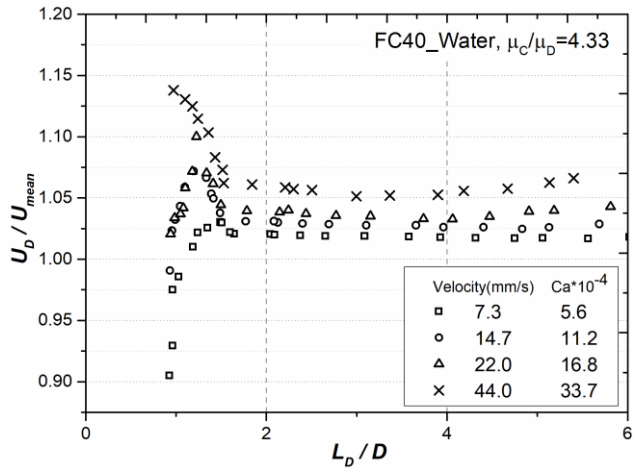

Figure H.2. Variation in droplet velocity ratio with dimensionless droplet length for experiments with FC40_Water, Bo = 0.3.

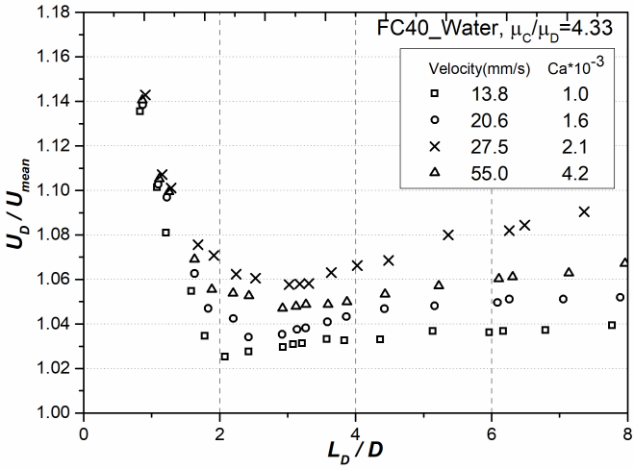

Figure H.3. Variation in droplet velocity ratio with dimensionless droplet length for experiments with FC40_Water, Bo = 0.05.

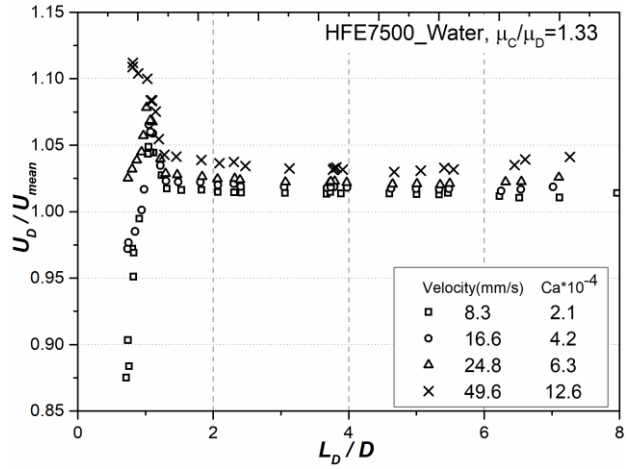

Figure H.4. Variation in droplet velocity ratio with dimensionless droplet length for experiments with (a) HFE7500_Water, Bo = 0.47.

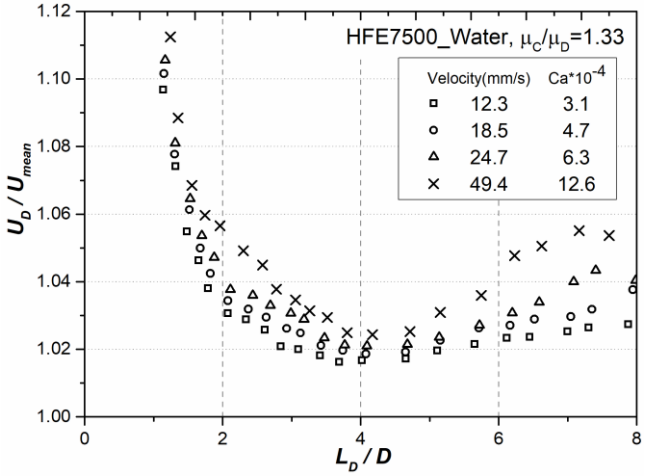

Figure H.5. Variation in droplet velocity ratio with dimensionless droplet length for experiments with HFE700_Water, Bo = 0.04.

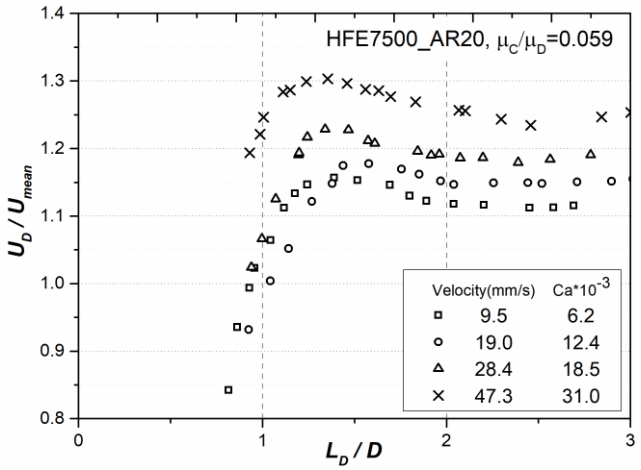

Figure H.6. Variation in droplet velocity ratio with dimensionless droplet length for experiments with HFE7500_AR20, Bo = 1.66.

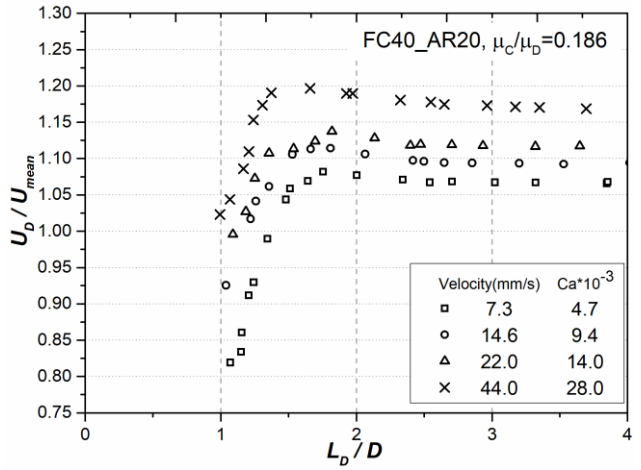

Figure H.7. Variation in droplet velocity ratio with dimensionless droplet length for experiments with FC40_AR20, Bo = 3.26.